

A NUMERICAL INVESTIGATION USING A NOVEL FINITE VOLUME METHOD OF SOME FLOW INSTABILITIES

THÈSE N° 2971 (2004)

PRÉSENTÉE À LA FACULTÉ SCIENCES ET TECHNIQUES DE L'INGÉNIEUR

Institut des sciences de l'énergie

SECTION DE GÉNIE MÉCANIQUE

ÉCOLE POLYTECHNIQUE FÉDÉRALE DE LAUSANNE

POUR L'OBTENTION DU GRADE DE DOCTEUR ÈS SCIENCES

PAR

Mehmet SAHIN

M.Sc. in Aerospace Engineering, Georgia Institute of Technology, Etats-Unis
et de nationalité turque

acceptée sur proposition du jury:

Prof. R. G. Owens, directeur de thèse
Prof. P. Oliveira, rapporteur
Prof. T. Phillips, rapporteur
Prof. J. Rappaz, rapporteur

Lausanne, EPFL
2004

Acknowledgements

I would like to thank my thesis supervisor Prof. Robert G. Owens for his continuous support and encouragement during the last three years. I am very grateful to have had such a unique opportunity to work with him on a very challenging research topic.

I would also like to acknowledge gratefully my colleagues from the Laboratory of Fluid Mechanics and the Laboratory of Computational Engineering of the EPFL, mentioning especially Alexei Lozinski, Christopher Pipe, Emmanuel Leriche, Farid Moussaoui and Nicolas Fiétier, for help and assistance during the course of my PhD.

Several interesting discussions with Prof. Peter Monkewitz on iterative computation of critical Reynolds numbers and secondary instabilities have been extremely useful. I also would like to thank Christophe Migeon at the Université de Poitiers in France for kindly providing his original particle-streak images for an impulsively accelerated lid-driven square cavity problem.

All the calculations presented here have been performed on the SGI Origin 3800 parallel machine *Eridan* with 124 processors and on the Linux cluster *Ielnx* with 22 processors. I should also mention many helpful suggestions from Trach-Minh Tran at SIC for parallelization and assistance for installing the *MUMPS* library.

I am also very grateful to Professors Alain Curnier, Paulo J. Oliveira, Timothy N. Phillips and Jacques C. Rappaz for being members of my thesis committee. Additionally, I would like to thank Prof. Oliveira for performing the drag computations for the MCR fluid that are shown in Fig. 6.2.

The École Polytechnique Fédérale de Lausanne and the Swiss National Science Foundation (grant number 2100-61865.00) are gratefully acknowledged for financial support over the last three years.

And, finally, I would like to thank my parents for their continuous support and understanding throughout my life.

Abstract

A novel implicit cell-vertex finite volume method is presented for the solution of both the Navier-Stokes equations and the governing equations for certain viscoelastic fluids. The key idea is the elimination of the pressure term from the momentum equation by multiplying the momentum equation with the unit normal vector to a control volume boundary and integrating thereafter around this boundary. The resulting equations are expressed solely in terms of the velocity components and, where appropriate, the components of elastic stress. Thus any difficulties with pressure or vorticity boundary conditions are circumvented and the number of primary variables that need to be determined equals the number of space dimension. As test cases, lid-driven cavity flow in a square enclosure and flow around a confined circular cylinder in a channel are solved in order to verify the accuracy of the present method and extensive comparisons are made with the results available in the literature. In addition, we investigate some interesting flow instabilities such as asymmetric flow around a confined circular cylinder at high blockage ratios and the stabilization effect of viscoelasticity for this flow. The numerical results are computed on meshes having up to 1.8 million degrees of freedom.

Version Abrégée

Une méthode originale de volumes finis basé sur approche implicite avec les variables assignées aux sommets (*cell – vertex*) est présentée pour la résolution à la fois des équations de Navier-Stokes et des équations régissant le comportement de certains fluides viscoélastiques. L'idée clé de cette approche est l'élimination du terme de pression des équations de moment en prenant le produit vectoriel de ces équations avec le vecteur unité normal à la frontière du volume de contrôle considéré, et en intégrant ensuite le long de cette frontière. Les équations résultantes sont alors uniquement exprimées dans les termes des composantes de vitesse et, si besoin, celles du tenseur d'élasticité. Ainsi toutes les difficultés rencontrée avec la pression ou les conditions de frontière à appliquer au champ de vorticit  sont contourn es et le nombre de variables primaires   d terminer explicitement est  gal au nombre de dimensions spatiales. Comme cas test, les probl mes de l' coulement dans la cavit  carr e entra n e ainsi que celui autour du cylindre circulaire confin  dans un canal plan ont  t  consid r s afin de v rifier la pr cision de la pr sente m thode et de la valider avec les r sultats disponibles dans la litt rature. En plus, nous avons  tudi  les instabilit s de ces  coulements. Dans le cas de l' coulement autour du cylindre confin  dans un canal plan pr sents d'importants rapports de blocage, une des solutions instables conduit   un  coulement non sym trique. L'effet stabilisateur d  au comportement visco lastique du fluide a  t  mis en  vidence pour ce type d' coulement. Les r sultats num riques se basent sur des maillages utilisant jusqu'  1.8 millions de degr s de libert .

Contents

Introduction	1
1 Governing Equations and Numerical Discretization	5
1.1 The Navier-Stokes Equations	5
1.1.1 Discretization of the time-dependent Navier-Stokes equations	7
1.1.2 Discretization of the steady Navier-Stokes equations	8
1.2 Viscoelastic Constitutive Equations	8
1.2.1 Discretization of time-dependent constitutive equations	11
1.2.2 Discretization of steady constitutive equations	12
2 Linear Stability Analysis	15
2.1 Linear Perturbation Equations for the Navier-Stokes Equations	15
2.2 Linear Perturbation Equations for the Modified FENE Chilcott-Rallison Fluid	16
2.3 The Arnoldi Method	17
3 Lid-Driven Cavity Flow at High Reynolds Numbers	21
3.1 Introduction	21
3.2 Numerical Results	24
3.2.1 The lid-driven cavity problem: steady flow	24
3.2.2 The lid-driven cavity problem: start-up flow	36
3.3 Conclusions	37
4 Linear Stability Analysis of a Lid-Driven Cavity Flow	41
4.1 Introduction	41
4.2 Numerical Results	43
4.3 Conclusions	47
5 Flow Around a Confined Circular Cylinder in a Channel	49
5.1 Introduction	49
5.2 Mathematical Problem	53
5.3 Flow Past an Unbounded Circular Cylinder	57
5.4 Flow Past a Confined Circular Cylinder ($0.1 < \Lambda < 0.9$)	61
5.4.1 Linear stability analysis	62
5.4.2 Direct numerical simulations	69
5.5 Conclusions	83

6	Viscoelastic Flow Past a Confined Circular Cylinder	85
6.1	Introduction	85
6.1.1	Purely elastic instabilities	85
6.1.2	Modification to the wake by polymer additives	87
6.2	Validation and Comparison with Other Results in the Literature	90
6.3	Linear Stability Analysis	94
6.3.1	Numerical considerations	94
6.3.2	Effect on linear stability of polymer additives	94
6.4	Direct Numerical Simulations	98
6.5	Conclusions	104
7	Conclusions and Future Perspectives	105
	Bibliography	109
	Curriculum Vitae	121

Introduction

Flow instabilities have a crucial importance for the polymer processing and materials manufacturing industries where output quality constraints require that operating conditions should be maintained in the stable flow regime. Therefore the prediction and understanding of flow instabilities under different flow conditions are highly desirable. Instabilities can be quite different in nature such as inertial instabilities, elastic instabilities, etc. Inertial instabilities manifest themselves at high Reynolds numbers while elastic instabilities may appear at vanishingly small Reynolds numbers where they are entirely absent in Newtonian fluids under the same flow conditions. Instabilities can also be classified as *temporal* or *spatial* depending on their nature.

During the last decade, significant progress has been made in the understanding of flow instabilities, particularly in the nature of inertial instabilities of a two-dimensional base flow. Three-dimensional temporal and spatial inertial instabilities in a finite domain are still challenging in terms of required computer power. Very limited success has been achieved in the understanding of elastic instabilities, however. This is particularly due to the complex nature of the constitutive equations. Although highly simplified constitutive models such as the Oldroyd-B, FENE models, etc. can be used the solution of these constitutive equations remains a challenging task in terms of accuracy, stability, convergence and required computer power. The stability analysis of viscoelastic flow is even more challenging due to the often prohibitively large generalized eigenvalue problem (GEVP) resulting from the linear stability analysis.

In the first part of this thesis, we propose a novel implicit cell-vertex finite volume method for the solution of the Navier-Stokes equations and the linear stability analysis. The key idea of the cell-vertex finite volume method is the elimination of the pressure term from the momentum equation by multiplying the momentum equation with the unit normal vector to a control volume boundary and integrating thereafter around this boundary. The resulting equations are expressed solely in terms of the velocity components. Thus any difficulties with pressure or vorticity boundary conditions are circumvented and the number of primary variables that need to be determined equals the number of space dimensions. The governing equations are discretized on four-node quadrilateral finite volume elements by using second-order-accurate central finite differences with the mid-point integration rule in space and first and second-order-accurate finite differences in time. The first reason to use the four-node quadrilateral finite volume formulation is to avoid a system of algebraic equations which is not diagonally dominant. In the past, Gatski et al. [54] tried to solve for the velocity components by using the definition of the vorticity and the dilatation in the velocity-vorticity formulation. In fact the main idea in this work was to solve Newtonian rotational flows with irrotational initial conditions. However in the formulation of Gatski et al. [54] the system of equations was not diagonally dominant and they reported that the iterative methods used to solve the block

matrix equations were not very efficient [53]. The second reason to use a four-node quadrilateral finite volume formulation is that the summation of the continuity equations within each finite volume element can be exactly reduced to the domain boundary which is important for the global conservation laws.

In the second part of this thesis, the proposed cell-vertex finite volume method based on the velocity-only formulation is then extended to a velocity-stress formulation for a viscoelastic fluid. To represent viscoelastic effects a constant viscosity modified FENE Chilcott-Rallison (MCR) model [31] is used. Unlike the velocity components, the elastic stress variables are defined at cell-centres and the governing equations are discretized on the same four-node quadrilateral finite volume elements in a similar manner to the cell-vertex finite volume method. However, the elastic stress fluxes at faces of the four-node quadrilateral finite volumes are evaluated using the QUICK [87] scheme in order to maintain stability. The whole system of algebraic equations is coupled and solved using a direct solver.

The outline of the thesis as follows:

- In Chapter 1, we outline the governing equations and their discretization using our finite volume method. Both steady and time-dependent formulations of our method are described. In the steady form a Newton method is employed.
- In Chapter 2, we begin by recalling the Navier-Stokes equations and proceed to consider the behavior with time of infinitesimal perturbations. The algebraic system for the nodal values of the eigenfunctions is derived. We also explain how we will use the method of Arnoldi [6, 121] for the accurate determination of the most dangerous eigenvalues that appear when the steady base flow is subjected to two-dimensional infinitesimal perturbations.
- In Chapter 3, the present method is applied to both the steady and unsteady two-dimensional lid-driven cavity flow in a square enclosure at Reynolds numbers up to 10000 in order to verify its accuracy. Results are compared with those in the literature. The results of this chapter have been published in [123, 124].
- In Chapter 4, the present method is applied in the linear stability analysis of a lid-driven cavity flow in a square enclosure. A combination of Arnoldi method and extrapolation to zero mesh size allows us to determine the first critical Reynolds number at which a Hopf bifurcation takes place. The results of this chapter have been published in [125].
- In Chapter 5, the present method is used to solve the flow field around a confined circular cylinder in a channel in order to investigate lateral wall proximity effects on stability, Strouhal number, hydrodynamic forces and wake structure behind the cylinder for a wide range of blockage ratios ($0.1 < \Lambda \leq 0.9$) and Reynolds numbers ($0 < Re \leq 280$).

Altogether, four distinct regions in the parameter space have been identified, each corresponding to a different class of flow: (i) steady symmetric flow, (ii) symmetric vortex shedding, (iii) steady asymmetric flow and (iv) asymmetric vortex shedding, where a periodic-in-time flow is classed as symmetric or asymmetric depending on whether the time-average over one cycle of the lift coefficient is zero or not.

Numerical solutions are computed on meshes having up to 1.8 million degrees of freedom. Extensive comparisons are made with the results available in the literature. The results of this chapter have been accepted for publication in [126].

-
- In Chapter 6, the present method is used to solve the viscoelastic flow field around a confined circular cylinder in a channel with blockage ratio $\Lambda = 0.5$. Our particular interest is the effect of polymer additives on the linear stability of two-dimensional viscous flow past a confined cylinder and our investigation involves both direct numerical simulation (DNS) and the solution of a generalized eigenvalue problem arising from the linearized perturbation equations. The present work represents, as far as we are aware, the first linear stability analysis for inertial flows of a viscoelastic fluid around a bluff body. The results of this chapter have been submitted for publication in [127].

Finally, we conclude with a summary of our results and address some outstanding issues.

Chapter 1

Governing Equations and Numerical Discretization

In this chapter first we present the Navier-Stokes equations and their discretization using a novel finite volume method for both steady and time-dependent flows. Then we present the extension of the present method to viscoelastic fluids using the modified FENE Chilcott-Rallison model. The method described in Section 1.1 will be used in Chapters 3, 4 and 5 while the method for viscoelastic fluids described in Section 1.2 will be used in Chapter 6.

1.1 The Navier-Stokes Equations

The incompressible unsteady Navier-Stokes equations may be written in dimensionless form over some domain $\Omega \subset \mathbb{R}^2$ as

$$\nabla \cdot \mathbf{u} = 0, \quad (1.1)$$

$$\frac{\partial \mathbf{u}}{\partial t} + (\mathbf{u} \cdot \nabla) \mathbf{u} = -\nabla p + \frac{1}{Re} \nabla^2 \mathbf{u}, \quad (1.2)$$

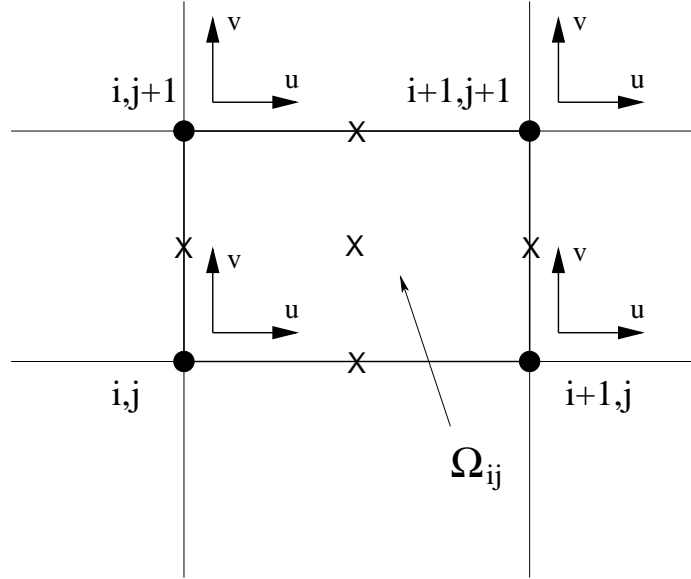
where, in the usual notation, $\mathbf{u} = (u, v)$ denotes the velocity field, p the pressure and Re is a Reynolds number.

Suppose now that Ω may be partitioned into quadrilateral finite volumes $\Omega_{i,j}$ with (i, j) in some finite subset of \mathbb{Z}^2 . Let \mathbf{n} denote an outward pointing normal vector to the boundary $\partial\Omega_{i,j}$ of $\Omega_{i,j}$. Then integrating (1.1) over one such finite volume $\Omega_{i,j}$ we get, on application of the divergence theorem, that

$$\oint_{\partial\Omega_{i,j}} \mathbf{n} \cdot \mathbf{u} \, ds = 0. \quad (1.3)$$

Let us take the vector product of (1.2) with \mathbf{n} and integrate around the boundary $\partial\Omega_{i,j}$ of $\Omega_{i,j}$ to get

$$\oint_{\partial\Omega_{i,j}} \mathbf{n} \times \left[\frac{\partial \mathbf{u}}{\partial t} + (\mathbf{u} \cdot \nabla) \mathbf{u} + \nabla p - \frac{1}{Re} \nabla^2 \mathbf{u} \right] ds = \mathbf{0}. \quad (1.4)$$

Figure 1.1: A four-node quadrilateral finite volume element Ω_{ij}

Using the following mathematical relations

$$(\mathbf{u} \cdot \nabla)\mathbf{u} = \nabla\left(\frac{|\mathbf{u}|^2}{2}\right) + (\nabla \times \mathbf{u}) \times \mathbf{u}, \quad (1.5)$$

$$\nabla^2 \mathbf{u} = \nabla(\nabla \cdot \mathbf{u}) + \nabla \times (\nabla \times \mathbf{u}) = \nabla \times (\nabla \times \mathbf{u}), \quad (1.6)$$

and since the closed line integral of the gradient terms is zero:

$$\oint_{\partial\Omega_{i,j}} \mathbf{n} \times \nabla \left[p + \frac{|\mathbf{u}|^2}{2} \right] ds = \mathbf{0}, \quad (1.7)$$

Eqn. (1.4) may be rewritten as

$$\oint_{\partial\Omega_{i,j}} \mathbf{n} \times \left[\frac{\partial \mathbf{u}}{\partial t} + (\nabla \times \mathbf{u}) \times \mathbf{u} + \frac{1}{Re} \nabla \times (\nabla \times \mathbf{u}) \right] ds = \mathbf{0}. \quad (1.8)$$

Note that no pressure term appears in (1.3) and (1.8). In fact, (1.8) is equal to the finite volume integral of the vorticity transport equation. However, here it is expressed solely in terms of the velocity components and therefore any difficulties associated with vorticity boundary conditions are obviated.

In this work we will solve (1.3) and (1.8) for the velocity components in coupled form by using a direct solver. For the sake of simplicity (and only for this reason) our exposé shall be limited to rectangular control volumes with sides parallel to the Cartesian axes Ox and Oy , and $\Omega_{i,j}$ shall denote the cell having lower left-hand vertex labelled (i, j) , as shown in Fig. 1.1. The velocity unknowns $\mathbf{u}_{i,j}^n = (u_{i,j}^n, v_{i,j}^n)$ at the n th time step or Newton iterate are located at cell vertices and physical points are denoted $(x_{i,j}, y_{i,j})$ in an obvious way.

1.1.1 Discretization of the time-dependent Navier-Stokes equations

The continuity equation (1.3) is enforced at time level $t = (n + 1)\Delta t$. To evaluate the integral over the boundary of $\Omega_{i,j}$, we use the mid-point rule on each of the four faces of $\Omega_{i,j}$, viz.

$$\begin{aligned} \oint_{\partial\Omega_{i,j}} \mathbf{n} \cdot \mathbf{u}^{n+1} ds &= \frac{v_{i+1,j+1}^{n+1} + v_{i,j+1}^{n+1}}{2}(x_{i+1,j+1} - x_{i,j+1}) - \frac{v_{i+1,j}^{n+1} + v_{i,j}^{n+1}}{2}(x_{i+1,j} - x_{i,j}) \\ &+ \frac{u_{i+1,j+1}^{n+1} + u_{i+1,j}^{n+1}}{2}(y_{i+1,j+1} - y_{i+1,j}) - \frac{u_{i,j+1}^{n+1} + u_{i,j}^{n+1}}{2}(y_{i,j+1} - y_{i,j}). \end{aligned} \quad (1.9)$$

For the time-dependent problem we discretize the integrand in (1.8) with both the Crank-Nicolson ($\kappa = 0.5$) and Euler implicit ($\kappa = 1$) methods which are second-order and first-order accurate in time accordingly:

$$\oint_{\partial\Omega_{i,j}} \mathbf{n} \times \left[\frac{\mathbf{u}^{n+1} - \mathbf{u}^n}{\Delta t} + \kappa \mathbf{E}^{n+1} + (1 - \kappa) \mathbf{E}^n \right] ds = 0, \quad (1.10)$$

where \mathbf{E}^n in (1.10) is defined by

$$\mathbf{E}^n = (E_1^n, E_2^n) = \boldsymbol{\omega}^n \times \mathbf{u}^n + \frac{1}{Re} \nabla \times \boldsymbol{\omega}^n. \quad (1.11)$$

The line integral in (1.10) is evaluated using the mid-point rule on each of the cell faces, this yielding

$$\begin{aligned} &(y_{i+1,j+1} - y_{i+1,j}) \left[\frac{(v_{i+1,j+1}^{n+1} - v_{i+1,j+1}^n)}{2\Delta t} + \frac{(v_{i+1,j}^{n+1} - v_{i+1,j}^n)}{2\Delta t} + \kappa E_{2,i+1,j+1/2}^{n+1} + (1 - \kappa) E_{2,i+1,j+1/2}^n \right] \\ &- (x_{i+1,j+1} - x_{i,j+1}) \left[\frac{(u_{i+1,j+1}^{n+1} - u_{i+1,j+1}^n)}{2\Delta t} + \frac{(u_{i+1,j}^{n+1} - u_{i+1,j}^n)}{2\Delta t} + \kappa E_{1,i+1/2,j+1}^{n+1} + (1 - \kappa) E_{1,i+1/2,j+1}^n \right] \\ &- (y_{i,j+1} - y_{i,j}) \left[\frac{(v_{i,j+1}^{n+1} - v_{i,j+1}^n)}{2\Delta t} + \frac{(v_{i,j}^{n+1} - v_{i,j}^n)}{2\Delta t} + \kappa E_{2,i,j+1/2}^{n+1} + (1 - \kappa) E_{2,i,j+1/2}^n \right] \\ &+ (x_{i+1,j} - x_{i,j}) \left[\frac{(u_{i+1,j}^{n+1} - u_{i+1,j}^n)}{2\Delta t} + \frac{(u_{i,j}^{n+1} - u_{i,j}^n)}{2\Delta t} + \kappa E_{1,i+1/2,j}^{n+1} + (1 - \kappa) E_{1,i+1/2,j}^n \right] = 0. \end{aligned} \quad (1.12)$$

The flux vector components $E_{1,i+1/2,j}$ and $E_{2,i,j+1/2}$ appearing in (1.12) are computed as follows:

$$\begin{aligned} E_{1,i+1/2,j} &= -\frac{1}{4}(v_{i,j} + v_{i+1,j})(\omega_{i+1/2,j+1/2} + \omega_{i+1/2,j-1/2}) \\ &\quad + \frac{1}{Re} \frac{\omega_{i+1/2,j+1/2} - \omega_{i+1/2,j-1/2}}{y_{i+1/2,j+1/2} - y_{i+1/2,j-1/2}}, \end{aligned} \quad (1.13)$$

$$\begin{aligned} E_{2,i,j+1/2} &= \frac{1}{4}(u_{i,j} + u_{i,j+1})(\omega_{i+1/2,j+1/2} + \omega_{i-1/2,j+1/2}) \\ &\quad - \frac{1}{Re} \frac{\omega_{i+1/2,j+1/2} - \omega_{i-1/2,j+1/2}}{x_{i+1/2,j+1/2} - x_{i-1/2,j+1/2}}. \end{aligned} \quad (1.14)$$

The non-linearities in $E_{1,i+1/2,j}^{n+1}$ and $E_{2,i,j+1/2}^{n+1}$ are treated by taking the velocity components (u, v) from the previous time step. To handle the vorticity terms in (1.13) and (1.14) a vorticity value at the centre of the (i, j) th cell $\Omega_{i,j}$ is calculated as

$$\omega_{i+1/2,j+1/2} = \frac{1}{\text{Area } \Omega_{i,j}} \oint_{\partial\Omega_{i,j}} \mathbf{n} \times \mathbf{u} \, ds, \quad (1.15)$$

where the line integral on the right-hand side of (1.15) is evaluated using the mid-point rule on each of the cell faces, as before.

1.1.2 Discretization of the steady Navier-Stokes equations

The same finite volumes described in Section 1.1.1 are used in the discretization of the steady problem. Let a superscript n now denote an iteration count. The steady form of (1.3) and (1.8) is solved using Newton's method: substituting $\mathbf{u} = \mathbf{u}^{n+1}$ into (1.3) and (1.8) where

$$\mathbf{u}^{n+1} = \mathbf{u}^n + \delta\mathbf{u}^{n+1}, \quad (1.16)$$

and neglecting second-order terms we get

$$\oint_{\partial\Omega_{i,j}} \mathbf{n} \cdot \delta\mathbf{u}^{n+1} \, ds = - \oint_{\partial\Omega_{i,j}} \mathbf{n} \cdot \mathbf{u}^n \, ds, \quad (1.17)$$

and

$$\oint_{\partial\Omega_{i,j}} \mathbf{n} \times \left[\delta\boldsymbol{\omega}^{n+1} \times \mathbf{u}^n + \boldsymbol{\omega}^n \times \delta\mathbf{u}^{n+1} + \frac{1}{Re} \nabla \times \delta\boldsymbol{\omega}^{n+1} \right] ds = - \oint_{\partial\Omega_{i,j}} \mathbf{n} \times \mathbf{E}^n \, ds. \quad (1.18)$$

(1.17) and (1.18) are discretized in a similar manner to Eqns. (1.9) and (1.10) and may be solved in coupled form using a direct solver. The new values of the velocity components at the $(n + 1)$ th iteration are calculated as follows:

$$\mathbf{u}_{i,j}^{n+1} = \mathbf{u}_{i,j}^n + \delta\mathbf{u}_{i,j}^{n+1}/\alpha, \quad (1.19)$$

where α is an under-relaxation parameter chosen in order to ensure convergence.

For both the steady and unsteady algorithms described in the previous two sections, mass conservation (Eqns. (1.9) and (1.17)) is applied in each finite volume. The vorticity transport equation (Eqns. (1.10) and (1.18)) is applied in each finite volume except those next to the walls; vorticity creation thus being permitted within these latter elements in order to satisfy the no-slip boundary conditions. The resulting algebraic systems of equations for the cell vertex values of \mathbf{u}^{n+1} or $\delta\mathbf{u}^{n+1}$ are block quad-diagonal and may be solved at each step (time step or Newton iterate) by using a direct solver.

1.2 Viscoelastic Constitutive Equations

The constitutive model to be used in our analysis and simulations is the so-called modified FENE Chilcott-Rallison (MCR) model, originally used by Coates et al. [31] in 1992 and is a simplified version of the original constant viscosity FENE model introduced by Chilcott and

Rallison [30] some four years previously. The Kramers expression for the elastic extra-stress $\boldsymbol{\tau}$ is given by

$$\boldsymbol{\tau} = -nkT\mathbf{I} + nHf(Q)\langle\mathbf{Q}\mathbf{Q}\rangle, \quad (1.20)$$

where, in the usual notation, n denotes a polymer number density, k is Boltzmann's constant, T is the absolute temperature, H is a spring constant and \mathbf{Q} is the dumbbell connector vector. $f(Q)$ is the spring law coefficient given by

$$f(Q) = \frac{1}{1 - \langle Q^2/Q_{max}^2 \rangle},$$

and we introduce the dimensionless orientation tensor

$$\mathbf{A} = \frac{1}{l_0^2}\langle\mathbf{Q}\mathbf{Q}\rangle,$$

where for d -dimensional configuration space

$$l_0 = \frac{\langle Q_{eq}^2 \rangle^{1/2}}{d^{1/2}},$$

denotes the average length of one component of the connector vector under equilibrium conditions. Now, for the full FENE CR model [30] \mathbf{A} satisfies the evolution equation

$$\overset{\nabla}{\mathbf{A}} = \frac{f(Q)}{\lambda}(\mathbf{I} - \mathbf{A}), \quad (1.21)$$

where λ is a relaxation time. Therefore, taking the upper convected derivative of the Kramers expression (1.20) and using Eqn. (1.21) we get

$$\begin{aligned} \overset{\nabla}{\boldsymbol{\tau}} &= -nkT \overset{\nabla}{\mathbf{I}} + nH \frac{Df(Q)}{Dt} \langle\mathbf{Q}\mathbf{Q}\rangle + nHf(Q) \langle\overset{\nabla}{\mathbf{Q}\mathbf{Q}}\rangle, \\ &= nkT\dot{\boldsymbol{\gamma}} + \frac{Df(Q)}{Dt} \left[\frac{\boldsymbol{\tau} + nkT\mathbf{I}}{f(Q)} \right] + \frac{nHl_0^2}{\lambda} f(Q)^2 \left[\mathbf{I} - \frac{1}{l_0^2} \langle\mathbf{Q}\mathbf{Q}\rangle \right], \\ &= nkT\dot{\boldsymbol{\gamma}} + \frac{Df(Q)}{Dt} \left[\frac{\boldsymbol{\tau} + nkT\mathbf{I}}{f(Q)} \right] + \frac{nHl_0^2}{\lambda} f(Q)^2 \mathbf{I} - \frac{f(Q)}{\lambda} [\boldsymbol{\tau} + nkT\mathbf{I}]. \end{aligned} \quad (1.22)$$

We now choose

$$\begin{aligned} \boldsymbol{\tau}' &= \boldsymbol{\tau} + nkT \left(1 - \frac{l_0^2 H}{kT} f(Q) \right) \mathbf{I} \\ &= nHl_0^2 f(Q) \left(\frac{1}{l_0^2} \langle\mathbf{Q}\mathbf{Q}\rangle - \mathbf{I} \right) = \frac{\eta_p}{\lambda} f(Q) (\mathbf{A} - \mathbf{I}), \end{aligned} \quad (1.23)$$

where $\eta_p = nH\lambda l_0^2$ is the polymeric viscosity. Then it may be seen that $\boldsymbol{\tau}'$ satisfies

$$\boldsymbol{\tau}' + \frac{\lambda}{f(Q)} \overset{\nabla}{\boldsymbol{\tau}'} = \eta_p \dot{\boldsymbol{\gamma}}, \quad (1.24)$$

where we have assumed (the simplification brought to bear in the MCR model) that Df/Dt is negligible. By performing a standard non-dimensionalization (starred variables) Eqn. (1.24) may be written in non-dimensional form as

$$\boldsymbol{\tau}'_* + \frac{We}{f_*(Q)} \nabla \boldsymbol{\tau}'_* = (1 - \beta) \dot{\boldsymbol{\gamma}}_*, \quad (1.25)$$

where We is a Weissenberg number and β is the solvent to total viscosity ratio. Supposing that the problem is defined in d configuration space dimensions, we may easily show by taking the trace of the Kramers expression (1.20) that

$$f(Q) = \frac{nH\langle Q_{max}^2 \rangle + tr\boldsymbol{\tau}'}{nH\langle Q_{max}^2 \rangle - dnHl_0^2} = \frac{b + \frac{\lambda}{\eta_p} tr\boldsymbol{\tau}'}{b - d} \left(= \frac{b}{b - tr\mathbf{A}} \right), \quad (1.26)$$

where $b = \langle Q_{max}^2 \rangle / l_0^2$, so that f_* in (1.25) is given by

$$f_* = \frac{b + \frac{We}{(1-\beta)} tr\boldsymbol{\tau}'_*}{b - d}. \quad (1.27)$$

We now drop the asterisks on dimensionless variables and write the non-dimensionalized momentum and continuity equations for the incompressible MCR fluid as

$$\nabla \cdot \mathbf{u} = 0, \quad (1.28)$$

$$\frac{\partial \mathbf{u}}{\partial t} + (\mathbf{u} \cdot \nabla) \mathbf{u} = -\nabla p + \frac{\beta}{Re} \nabla^2 \mathbf{u} + \frac{1}{Re} \nabla \cdot \boldsymbol{\tau}'. \quad (1.29)$$

As before, let \mathbf{n} denote a unit outward pointing normal vector to the boundary $\partial\Omega_{i,j}$ of a finite volume $\Omega_{i,j}$. Then integration of (1.28) and (1.25) over $\Omega_{i,j}$ and taking the vector product of (1.29) with \mathbf{n} , followed by integration around $\partial\Omega_{i,j}$ leads to

$$\oint_{\partial\Omega_{i,j}} \mathbf{n} \cdot \mathbf{u} \, ds = 0, \quad (1.30)$$

$$\oint_{\partial\Omega_{i,j}} \mathbf{n} \times \left[\frac{\partial \mathbf{u}}{\partial t} + (\nabla \times \mathbf{u}) \times \mathbf{u} + \frac{\beta}{Re} \nabla \times (\nabla \times \mathbf{u}) - \frac{1}{Re} \nabla \cdot \boldsymbol{\tau}' \right] ds = \mathbf{0}, \quad (1.31)$$

$$\begin{aligned} \int_{\Omega_{i,j}} \boldsymbol{\tau}' d\Omega + \int_{\Omega_{i,j}} \frac{We}{f(Q)} \left[\frac{\partial \boldsymbol{\tau}'}{\partial t} + \mathbf{u} \nabla \boldsymbol{\tau}' - \nabla \mathbf{u}^T \boldsymbol{\tau}' - \boldsymbol{\tau}' \nabla \mathbf{u} \right] d\Omega \\ = (1 - \beta) \oint_{\partial\Omega_{i,j}} [\mathbf{u} \mathbf{n} + (\mathbf{u} \mathbf{n})^T] ds. \end{aligned} \quad (1.32)$$

A fully-implicit finite volume method based on a velocity-stress formulation is used for the discretization of (1.30), (1.31) and (1.32). Velocity nodes appear at cell vertices and the elastic stress nodes at cell centres, as shown schematically in Fig. 1.2. Discretization of the integrals appearing in (1.30) and (1.31) is effected by using the mid-point rule on cell faces in a similar manner to the discretization of Newtonian flow in Section 1.1. In the interests of brevity they will not be reproduced here. However, we present the discretization of the constitutive equation (1.32).

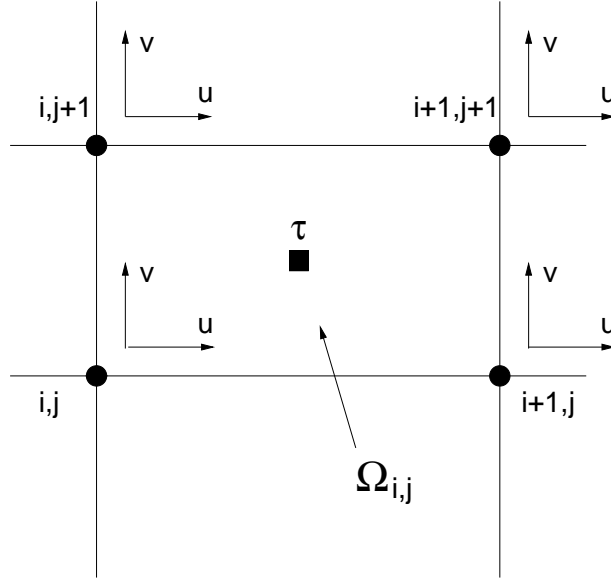


Figure 1.2: A four-node quadrilateral finite volume $\Omega_{i,j}$ showing positioning of velocity and elastic stress nodes.

1.2.1 Discretization of time-dependent constitutive equations

For time-dependent calculations let us denote the evaluation of a velocity or stress variable at time step $n\Delta t$ with a subscript n . The non-linearities in Eqn. (1.32) are treated taking $f(Q)$ from the previous time step at the cell centre and the velocity gradients in multiplication with τ' are evaluated at the cell centre from the previous time step. In Chapter 6 we will use both the Euler-implicit ($\kappa = 1$) and Crank-Nicolson ($\kappa = 0.5$) for discretization of the partial time derivative:

$$\begin{aligned}
 & \int_{\Omega_{i,j}} \kappa \tau'_{n+1} + (1 - \kappa) \tau'_n d\Omega + \frac{We}{f(Q)_n} \oint_{\partial\Omega_{i,j}} (\mathbf{n} \cdot \mathbf{u}_n) [\kappa \tau'_{n+1} + (1 - \kappa) \tau'_n] ds \\
 & + \frac{We}{f(Q)_n} \int_{\Omega_{i,j}} \left[\frac{\tau'_{n+1} - \tau'_n}{\Delta t} - (\nabla \mathbf{u}_n)^T [\kappa \tau'_{n+1} + (1 - \kappa) \tau'_n] - [\kappa \tau'_{n+1} + (1 - \kappa) \tau'_n] (\nabla \mathbf{u}_n) \right] d\Omega \\
 & = \kappa(1 - \beta) \oint_{\partial\Omega_{i,j}} (\mathbf{n} \mathbf{u}_{n+1} + \mathbf{n} \mathbf{u}_{n+1}^T) ds + (1 - \kappa)(1 - \beta) \oint_{\partial\Omega_{i,j}} [\mathbf{u}_n \mathbf{n} + (\mathbf{u}_n \mathbf{n})^T] ds.
 \end{aligned} \tag{1.33}$$

For the calculation of the velocity gradients in a cell centre in (1.33), first we compute the velocity gradients at vertices using second-order accurate finite differences. Then we compute the average cell-centre values from the surrounding cell-vertex values. One may compute these velocity gradients in a similar manner to the calculation of vorticity in (1.15). However, this leads to odd-even oscillations even though it uses a shorter stencil. Integration of (1.33) leads

to

$$\begin{aligned}
& \text{Area}\Omega_{i,j}[\kappa\boldsymbol{\tau}'_{n+1} + (1-\kappa)\boldsymbol{\tau}'_n]_{i+1/2,j+1/2} + \frac{We\text{Area}\Omega_{i,j}}{f(Q)_{n,i+1/2,j+1/2}} \frac{\boldsymbol{\tau}'_{n+1,i+1/2,j+1/2} - \boldsymbol{\tau}'_{n,i+1/2,j+1/2}}{\Delta t} \\
& - \frac{We\text{Area}\Omega_{i,j}}{f(Q)_{n,i+1/2,j+1/2}} [(\nabla\mathbf{u}_n)^T[\kappa\boldsymbol{\tau}'_{n+1} + (1-\kappa)\boldsymbol{\tau}'_n] + [\kappa\boldsymbol{\tau}'_{n+1} + (1-\kappa)\boldsymbol{\tau}'_n](\nabla\mathbf{u}_n)]_{i+1/2,j+1/2} \\
& + \frac{We}{f(Q)_{n,i+1/2,j+1/2}} \sum_{e=1}^4 (\mathbf{n} \cdot \mathbf{u}_n)_e [\kappa\boldsymbol{\tau}'_{n+1} + (1-\kappa)\boldsymbol{\tau}'_n]_e \Delta S_e \\
& = \kappa(1-\beta) \sum_{e=1}^4 [\mathbf{u}_{n+1}\mathbf{n} + (\mathbf{u}_{n+1}\mathbf{n})^T]_e \Delta S_e + (1-\kappa)(1-\beta) \sum_{e=1}^4 [\mathbf{u}_n\mathbf{n} + (\mathbf{u}_n\mathbf{n})^T]_e \Delta S_e,
\end{aligned} \tag{1.34}$$

where summation over e in (1.34) represents the evaluation of the surface integral over the four-node quadrilateral element boundary $\partial\Omega_{ij}$ and ΔS_e is an edge length. The face values of $\delta\mathbf{v}_n$ appearing in the line integrals around the boundary $\partial\Omega_{ij}$ are evaluated using the mid-point rule. Face values of $\delta\boldsymbol{\tau}'_n$ are evaluated using QUICK [87] in order to maintain stability. The whole system of algebraic equations may be solved in coupled form using a direct solver.

1.2.2 Discretization of steady constitutive equations

For the discretization of the MCR constitutive equation (1.32) we begin by writing $\boldsymbol{\tau}'_{n+1} = \boldsymbol{\tau}'_n + \delta\boldsymbol{\tau}'_n$ and $\mathbf{u}_{n+1} = \mathbf{u}_n + \delta\mathbf{u}_n$ for updates $\delta\boldsymbol{\tau}'_n$ and $\delta\mathbf{u}_n$ to $\boldsymbol{\tau}'_n$ and \mathbf{u}_n , respectively. Denoting for convenience the ratio $We/(1-\beta)$ by θ we then get

$$\begin{aligned}
& \int_{\Omega_{i,j}} \boldsymbol{\tau}'_n + \delta\boldsymbol{\tau}'_n d\Omega - \int_{\Omega_{i,j}} \frac{We(b-d)}{b + \theta(\text{tr}\boldsymbol{\tau}'_n + \text{tr}\delta\boldsymbol{\tau}'_n)} [\nabla(\mathbf{u}_n + \delta\mathbf{u}_n)^T \boldsymbol{\tau}'_n + \nabla(\mathbf{u}_n + \delta\mathbf{u}_n)^T \delta\boldsymbol{\tau}'_n] d\Omega \\
& - \int_{\Omega_{i,j}} \frac{We(b-d)}{b + \theta(\text{tr}\boldsymbol{\tau}'_n + \text{tr}\delta\boldsymbol{\tau}'_n)} [\boldsymbol{\tau}'_n \nabla(\mathbf{u}_n + \delta\mathbf{u}_n) + \delta\boldsymbol{\tau}'_n \nabla(\mathbf{u}_n + \delta\mathbf{u}_n)] d\Omega \\
& + \int_{\Omega_{i,j}} \frac{We(b-d)}{b + \theta(\text{tr}\boldsymbol{\tau}'_n + \text{tr}\delta\boldsymbol{\tau}'_n)} (\mathbf{u}_n + \delta\mathbf{u}_n) \cdot (\nabla\boldsymbol{\tau}'_n + \nabla\delta\boldsymbol{\tau}'_n) d\Omega \\
& = (1-\beta) \oint_{\partial\Omega_{i,j}} [(\mathbf{u}_n + \delta\mathbf{u}_n)\mathbf{n} + ((\mathbf{u}_n + \delta\mathbf{u}_n)\mathbf{n})^T] ds.
\end{aligned} \tag{1.35}$$

Assuming $\delta\boldsymbol{\tau}'_n$ and $\delta\mathbf{u}_n$ to be sufficiently small that quadratic and higher powers of these terms may be neglected we may write

$$\begin{aligned}
\frac{We(b-d)}{b + \theta(\text{tr}\boldsymbol{\tau}'_n + \text{tr}\delta\boldsymbol{\tau}'_n)} &= \frac{We(b-d)}{\theta \left(\frac{b}{\theta} + \text{tr}\boldsymbol{\tau}'_n \right) \left(1 + \frac{\text{tr}\delta\boldsymbol{\tau}'_n}{\frac{b}{\theta} + \text{tr}\boldsymbol{\tau}'_n} \right)} \\
&\approx \frac{We(b-d)}{(b + \theta\text{tr}\boldsymbol{\tau}'_n)} \left[1 - \frac{\text{tr}\delta\boldsymbol{\tau}'_n}{\left(\frac{b}{\theta} + \text{tr}\boldsymbol{\tau}'_n \right)} \right],
\end{aligned} \tag{1.36}$$

Inserting Eqn. (1.36) into (1.35), neglecting higher order terms and using equation (1.25) leads to

$$\begin{aligned}
\int_{\Omega_{i,j}} \delta \boldsymbol{\tau}'_n d\Omega - \int_{\Omega_{i,j}} \frac{We(b-d)}{b + \theta tr \boldsymbol{\tau}'_n} [\nabla \mathbf{u}_n \delta \boldsymbol{\tau}'_n + \nabla \delta \mathbf{u}_n \boldsymbol{\tau}'_n + \delta \boldsymbol{\tau}'_n \nabla \mathbf{u}_n^T + \boldsymbol{\tau}'_n \nabla \delta \mathbf{u}_n^T] d\Omega \\
+ \int_{\Omega_{i,j}} \frac{We(b-d)}{b + \theta tr \boldsymbol{\tau}'_n} [\mathbf{u}_n \cdot \nabla \delta \boldsymbol{\tau}'_n + \delta \mathbf{u}_n \cdot \nabla \boldsymbol{\tau}'_n] d\Omega \\
- \int_{\Omega_{i,j}} \frac{\theta}{b + \theta tr \boldsymbol{\tau}'_n} tr \delta \boldsymbol{\tau}'_n [\nabla \mathbf{u}_n + \nabla \mathbf{u}_n^T - \boldsymbol{\tau}'_n] d\Omega \\
- (1 - \beta) \oint_{\partial \Omega_{i,j}} [\delta \mathbf{u}_n \mathbf{n} + (\delta \mathbf{u}_n \mathbf{n})^T] ds = \mathbf{r}_n. \quad (1.37)
\end{aligned}$$

where \mathbf{r}_n denotes the residual at n th iteration

$$\begin{aligned}
\mathbf{r}_n = - \int_{\Omega_{i,j}} \boldsymbol{\tau}'_n d\Omega + \int_{\Omega_{i,j}} \frac{We(b-d)}{b + \theta tr \boldsymbol{\tau}'_n} [\nabla \mathbf{u}_n^T \boldsymbol{\tau}'_n + \boldsymbol{\tau}'_n \nabla \mathbf{u}_n - \mathbf{u}_n \cdot \nabla \boldsymbol{\tau}'_n] d\Omega \\
+ (1 - \beta) \oint_{\partial \Omega_{i,j}} [\mathbf{u}_n \mathbf{n} + (\mathbf{u}_n \mathbf{n})^T] ds. \quad (1.38)
\end{aligned}$$

Eqn. (1.38) may be similarly integrated over a finite volume Ω_{ij} and the nonlinearities are treated as in Section 1.2.1:

$$\begin{aligned}
Area \Omega_{i,j} \delta \boldsymbol{\tau}'_n - \frac{We(b-d) Area \Omega_{i,j}}{b + \theta tr \boldsymbol{\tau}'_{n,i+1/2,j+1/2}} [\nabla \mathbf{u}_n \delta \boldsymbol{\tau}'_n + \nabla \delta \mathbf{u}_n \boldsymbol{\tau}'_n + \delta \boldsymbol{\tau}'_n \nabla \mathbf{u}_n^T + \boldsymbol{\tau}'_n \nabla \delta \mathbf{u}_n^T]_{i+1/2,j+1/2} \\
+ \frac{We(b-d)}{b + \theta tr \boldsymbol{\tau}'_{n,i+1/2,j+1/2}} \sum_{e=1}^4 [(\mathbf{n} \cdot \mathbf{u}_n) \delta \boldsymbol{\tau}'_n + (\mathbf{n} \cdot \delta \mathbf{u}_n) \boldsymbol{\tau}'_n]_e \Delta S_e \\
- \frac{\theta Area \Omega_{i,j}}{b + \theta tr \boldsymbol{\tau}'_{n,i+1/2,j+1/2}} tr \delta \boldsymbol{\tau}'_{n,i+1/2,j+1/2} [\nabla \mathbf{u}_n + \nabla \mathbf{u}_n^T - \boldsymbol{\tau}'_n]_{i+1/2,j+1/2} \\
- (1 - \beta) \sum_{e=1}^4 [\delta \mathbf{u}_n \mathbf{n} + (\delta \mathbf{u}_n \mathbf{n})^T]_e \Delta S_e = \mathbf{r}_{n,i+1/2,j+1/2}. \quad (1.39)
\end{aligned}$$

The updated value of $\boldsymbol{\tau}'$ is computed from

$$\boldsymbol{\tau}'_{n+1} = \boldsymbol{\tau}'_n + \delta \boldsymbol{\tau}' / \alpha. \quad (1.40)$$

where α is an under-relaxation parameter. In all our calculations we use the same α parameter for both \mathbf{u} and $\boldsymbol{\tau}'$.

Chapter 2

Linear Stability Analysis

In this chapter we recall the governing equations given in Chapter 1 and introduce infinitesimal disturbances to the steady base flow. Then we describe the discretization of the linear perturbation equations and how to compute the leading eigenvalues of the GEVP using the Arnoldi method. The linear stability analysis presented in this chapter will be used in Chapters 4, 5 and 6.

2.1 Linear Perturbation Equations for the Navier-Stokes Equations

In Chapter 1 we showed that integration of (1.1) over a finite volume $\Omega_{i,j}$ and multiplication of Eqn. (1.2) with a vector normal to the boundary $\partial\Omega_{i,j}$ of $\Omega_{i,j}$, followed by integration around $\partial\Omega_{i,j}$ led to

$$\oint_{\partial\Omega_{i,j}} \mathbf{n} \cdot \mathbf{u} \, ds = 0, \quad (2.1)$$

and

$$\oint_{\partial\Omega_{i,j}} \mathbf{n} \times \left[\frac{\partial \mathbf{u}}{\partial t} + (\nabla \times \mathbf{u}) \times \mathbf{u} + \frac{1}{Re} \nabla \times (\nabla \times \mathbf{u}) \right] ds = \mathbf{0}. \quad (2.2)$$

respectively. To study the linear stability of the steady base flow velocity $\mathbf{u} = \mathbf{U}$, computed using Newton's method as described in Chapter 1, we consider the behavior with time of the infinitesimally perturbed flow

$$\mathbf{u} = \mathbf{U}(\mathbf{x}) + \tilde{\mathbf{v}}(\mathbf{x}) \exp(\sigma t). \quad (2.3)$$

Inserting (2.3) into (2.1) and (2.2), assuming \mathbf{U} to be an exact solution to the steady Navier-Stokes equations and neglecting quadratic terms in \mathbf{v} we get

$$\oint_{\partial\Omega_{i,j}} \mathbf{n} \cdot \tilde{\mathbf{v}} \, ds = 0, \quad (2.4)$$

and

$$\oint_{\partial\Omega_{i,j}} \mathbf{n} \times \left[(\nabla \times \mathbf{U}) \times \tilde{\mathbf{v}} + (\nabla \times \tilde{\mathbf{v}}) \times \mathbf{U} + \frac{1}{Re} \nabla \times (\nabla \times \tilde{\mathbf{v}}) \right] ds = -\sigma \oint_{\partial\Omega_{i,j}} \mathbf{n} \times \tilde{\mathbf{v}} \, ds. \quad (2.5)$$

The evaluation of the line integrals appearing in (2.4) and (2.5) follows very closely the ideas employed for the solution of the steady equations of linear momentum and conservation of mass described in Section 1.1.2: the line integrals are computed using the mid-point rule and in (2.5) a perturbation vorticity vector $\tilde{\boldsymbol{\omega}} = \nabla \times \tilde{\mathbf{v}}$ is defined at the centre of each finite volume. Face values of vorticity are then determined from simple averages of the cell-centred values in the cells either side of the face in question. The end result of following this procedure for the evaluation of (2.4) and (2.5) is a discrete algebraic system for the nodal values of $\tilde{\mathbf{v}}$ of the form

$$A\mathbf{x} = \sigma M\mathbf{x}, \quad (2.6)$$

A being almost the same (by construction) as the coefficient matrix arising from the discretization of the continuity equation and momentum equation, described in Section 1.1.2, the sole difference being that nodal values of \mathbf{u}^n (the n th Newton iterative value of velocity) are now replaced with the corresponding nodal values of \mathbf{U} . The matrix M in (2.6) is block bi-diagonal.

2.2 Linear Perturbation Equations for the Modified FENE Chilcott-Rallison Fluid

For the linear stability of two-dimensional flow of the MCR fluid (see equations (1.30), (1.31) and (1.32)) we consider the perturbed flow

$$\mathbf{u}(\mathbf{x}, t) = \mathbf{U}(\mathbf{x}) + \tilde{\mathbf{v}}(\mathbf{x}) \exp(\sigma t), \quad (2.7)$$

$$\boldsymbol{\tau}'(\mathbf{x}, t) = \mathbf{T}(\mathbf{x}) + \tilde{\boldsymbol{\tau}}(\mathbf{x}) \exp(\sigma t), \quad (2.8)$$

where $\mathbf{U}(\mathbf{x})$ and $\mathbf{T}(\mathbf{x})$ are the (numerically-determined) steady base flow velocity and elastic stress fields at given values of Re and We and $\tilde{\mathbf{v}}$ and $\tilde{\boldsymbol{\tau}}$ are infinitesimally small perturbations. Inserting (2.7) and (2.8) into the non-dimensional constitutive equation for the MCR model

$$\begin{aligned} & \int_{\Omega} (\mathbf{T} + \tilde{\boldsymbol{\tau}} \exp(\sigma t)) d\Omega + \int_{\Omega} \frac{We(b-d)}{b + \theta(tr\mathbf{T} + tr\tilde{\boldsymbol{\tau}} \exp(\sigma t))} [\sigma \tilde{\boldsymbol{\tau}} \exp(\sigma t)] d\Omega \\ & + \int_{\Omega} \frac{We(b-d)}{b + \theta(tr\mathbf{T} + tr\tilde{\boldsymbol{\tau}} \exp(\sigma t))} [(\mathbf{U} + \tilde{\mathbf{v}} \exp(\sigma t)) \cdot \nabla (\mathbf{T} + \tilde{\boldsymbol{\tau}} \exp(\sigma t))] d\Omega \\ & - \int_{\Omega} \frac{We(b-d)}{b + \theta(tr\mathbf{T} + tr\tilde{\boldsymbol{\tau}} \exp(\sigma t))} [\nabla (\mathbf{U} + \tilde{\mathbf{v}} \exp(\sigma t))^T (\mathbf{T} + \tilde{\boldsymbol{\tau}} \exp(\sigma t))] d\Omega \\ & - \int_{\Omega} \frac{We(b-d)}{b + \theta(tr\mathbf{T} + tr\tilde{\boldsymbol{\tau}} \exp(\sigma t))} [(\mathbf{T} + \tilde{\boldsymbol{\tau}} \exp(\sigma t)) \nabla (\mathbf{U} + \tilde{\mathbf{v}} \exp(\sigma t))] d\Omega \\ & = (1 - \beta) \oint_{\partial\Omega} [(\mathbf{U} + \tilde{\mathbf{v}} \exp(\sigma t))\mathbf{n} + ((\mathbf{U} + \tilde{\mathbf{v}} \exp(\sigma t))\mathbf{n})^T] ds. \end{aligned} \quad (2.9)$$

We note, following reasoning similar to that which led to (1.36), that

$$\begin{aligned} \frac{We(b-d)}{b + \theta(tr\mathbf{T} + tr\tilde{\boldsymbol{\tau}} \exp(\sigma t))} &= \frac{We(b-d)}{\theta \left(\frac{b}{\theta} + tr\mathbf{T} \right) \left(1 + \frac{tr\tilde{\boldsymbol{\tau}} \exp(\sigma t)}{\frac{b}{\theta} + tr\mathbf{T}} \right)} \\ &\approx \frac{We(b-d)}{(b + \theta tr\mathbf{T})} \left[1 - \frac{tr\tilde{\boldsymbol{\tau}} \exp(\sigma t)}{\left(\frac{b}{\theta} + tr\mathbf{T} \right)} \right], \end{aligned} \quad (2.10)$$

and inserting this into (2.9), further linearizing and exploiting the fact that \mathbf{T} is a solution to the steady constitutive equation with velocity field \mathbf{U}

$$\begin{aligned} & \int_{\Omega} \tilde{\boldsymbol{\tau}} d\Omega + \int_{\Omega} \frac{We(b-d)}{b + \theta \text{tr} \mathbf{T}} [\sigma \tilde{\boldsymbol{\tau}} + \mathbf{U} \cdot \nabla \tilde{\boldsymbol{\tau}} + \tilde{\mathbf{v}} \cdot \nabla \mathbf{T}] d\Omega \\ & - \int_{\Omega} \frac{We(b-d)}{b + \theta \text{tr} \mathbf{T}} [\nabla \mathbf{U}^T \tilde{\boldsymbol{\tau}} + \nabla \tilde{\mathbf{v}}^T \mathbf{T} + \mathbf{T} \nabla \tilde{\mathbf{v}} + \tilde{\boldsymbol{\tau}} \nabla \mathbf{U}] d\Omega \\ & - \int_{\Omega} \frac{\theta We(b-d)}{(b + \theta \text{tr} \mathbf{T})^2} \text{tr} \tilde{\boldsymbol{\tau}} [\mathbf{U} \cdot \nabla \mathbf{T} - \nabla \mathbf{U}^T \mathbf{T} - \mathbf{T} \nabla \mathbf{V}] d\Omega \\ & = (1 - \beta) \oint_{\partial\Omega} [\tilde{\mathbf{v}} \mathbf{n} + (\tilde{\mathbf{v}} \mathbf{n})^T] ds. \end{aligned} \quad (2.11)$$

Since \mathbf{T} is a solution to the steady constitutive equation we have

$$\mathbf{T} + \frac{We(b-d)}{b + \theta(\text{tr} \mathbf{T})} \overset{\nabla}{\mathbf{T}} = (1 - \beta)(\nabla \mathbf{U} + \nabla \mathbf{U}^T), \quad (2.12)$$

and therefore we may rewrite the last term on the left-hand side of (2.11) to get the equation

$$\begin{aligned} & \int_{\Omega} \tilde{\boldsymbol{\tau}} d\Omega + \int_{\Omega} \frac{We(b-d)}{b + \theta \text{tr} \mathbf{T}} [\sigma \tilde{\boldsymbol{\tau}} + \mathbf{U} \cdot \nabla \tilde{\boldsymbol{\tau}} + \tilde{\mathbf{v}} \cdot \nabla \mathbf{T}] d\Omega \\ & - \int_{\Omega} \frac{We(b-d)}{b + \theta \text{tr} \mathbf{T}} [\nabla \mathbf{U}^T \tilde{\boldsymbol{\tau}} + \nabla \tilde{\mathbf{v}}^T \mathbf{T} + \mathbf{T} \nabla \tilde{\mathbf{v}} + \tilde{\boldsymbol{\tau}} \nabla \mathbf{U}] d\Omega \\ & - \int_{\Omega} \frac{\theta \text{tr} \tilde{\boldsymbol{\tau}}}{(b + \theta \text{tr} \mathbf{T})} [(1 - \beta)(\nabla \mathbf{U} + \nabla \mathbf{U}^T) - \mathbf{T}] d\Omega \\ & = (1 - \beta) \oint_{\partial\Omega} [\tilde{\mathbf{v}} \mathbf{n} + (\tilde{\mathbf{v}} \mathbf{n})^T] ds. \end{aligned} \quad (2.13)$$

Discretizing the dimensionless perturbation equation (2.13) and those corresponding to the momentum-continuity pair leads to an algebraic system of equations

$$\mathbf{A} \mathbf{w} = \sigma \mathbf{M} \mathbf{w}, \quad (2.14)$$

for the vector \mathbf{w} of nodal values of the perturbation velocity $\tilde{\mathbf{v}}$ and the perturbation stress $\tilde{\boldsymbol{\tau}}$. The coefficient matrix \mathbf{A} in (2.14) is almost identical (by construction) to that which arises in the computations of the steady base flow using Newton's method. The matrices \mathbf{A} and \mathbf{M} in (2.14) are block penta-diagonal and block bi-diagonal, respectively.

2.3 The Arnoldi Method

The Arnoldi method is an orthogonal projection method onto a Krylov subspace. It can be viewed as a Modified Gram-Schmidt method for building an orthogonal basis of the Krylov subspace. The GEVP (2.6) and (2.14) is solved by applying the Arnoldi method [6, 121] to the equivalent system

$$\mathbf{C} \mathbf{x} = \mu \mathbf{x}, \quad (2.15)$$

where $\mathbf{C} = (\mathbf{A} - \lambda \mathbf{M})^{-1} \mathbf{M}$ and $\mu = (\sigma - \lambda)^{-1}$. A pseudo-code form of the Arnoldi method for a Krylov space of dimension m is given in Table 2.1 where $h_{i,j}$ is the (i, j) th element of

Table 2.1: Pseudo-code for the Arnoldi method. $h_{i,j}$ is the (i, j) th element of an upper Hessenberg matrix H . The vectors $\mathbf{x}_1, \mathbf{x}_2, \dots, \mathbf{x}_m$ form an orthonormal system by construction (modified Gram-Schmidt algorithm).

```

 $\mathbf{x}_1 = \frac{\mathbf{x}}{\|\mathbf{x}\|_2}$ 
for  $j = 1, 2, \dots, m$  do
   $\mathbf{w} = A^{-1}M\mathbf{x}_j$ 
  for  $i = 1, 2, \dots, j$  do
     $h_{i,j} = \mathbf{w} \cdot \mathbf{x}_i$ 
     $\mathbf{w} = \mathbf{w} - h_{i,j}\mathbf{x}_i$ 
  end for
   $h_{j+1,j} = \|\mathbf{w}\|_2$ 
   $\mathbf{x}_{j+1} = \mathbf{w}/h_{j+1,j}$ 
end for

```

an upper Hessenberg matrix H and the vectors $\mathbf{x}_1, \mathbf{x}_2, \dots, \mathbf{x}_m$ form an orthonormal system by construction called *Arnoldi vectors*. Application of the Arnoldi method to Eq. (2.15) results in the construction of an $m \times m$ upper Hessenberg matrix whose eigenvalues are approximations to a subset of the eigenvalues μ of \mathbf{C} (often called Ritz values). From the properties of the Arnoldi method and in the absence of a shift λ , best resolution of the σ -spectrum is expected to be near the origin [105]. In fact although - as will be seen in the numerical results in Section 5.4.1- the imaginary axis is first crossed by a complex conjugate *pair* of eigenvalues or a real eigenvalue, these are supposed to be adequately approximated by the reciprocals $\hat{\mu}^{-1}$ of the corresponding Ritz values. Incorporating a complex shift [105], although desirable from the point of view of accuracy, would necessitate working in complex arithmetic and increase significantly the computational cost. The Ritz values of H are computed by using the Intel Math Kernel Library which uses a multishift form of the upper Hessenberg QR algorithm. A Ritz eigenvector associated with the eigenvalue $\mu^{(m)}$ is defined by

$$u^{(m)} = V_m y^{(m)}, \quad (2.16)$$

where V_m is the matrix with column vectors $\mathbf{x}_1, \mathbf{x}_2, \dots, \mathbf{x}_m$ and $y^{(m)}$ is an eigenvector of the upper Hessenberg matrix H .

Solutions to all the discrete algebraic equations that arise in the steady, unsteady or eigenvalue problems of this thesis have been obtained by implementing the *MULTifrontal MASSively Parallel Solver (MUMPS)* of Amestoy *et al.* [3, 4] on parallel machines or using block Gaussian elimination on sequential machines. The multifrontal method used is a direct method based on LU decomposition for the solution of sparse systems of linear equations with optimum fill in. The algorithms employed by *MUMPS* use a dynamic distributed task scheduling technique that permits numerical pivoting and the transfer of computational tasks to lightly loaded processors. The use of the *MUMPS* library allows us to store very large sparse systems in factorized form which leads to a very efficient eigenvalue solver since at each Arnoldi itera-

tion we need to solve the same system of equations ($\mathbf{A}\mathbf{w} = \mathbf{b}$) with different right-hand sides. On sequential machines considerable computational time has been saved with extensive use of the Intel Math Kernel Library for block matrix-matrix and matrix-vector operations.

Chapter 3

Lid-Driven Cavity Flow at High Reynolds Numbers

3.1 Introduction

The lid-driven cavity flow of a Newtonian fluid has occupied the attention of the scientific computational community since the pioneering paper of Burggraf [21] back in 1966. Over the years the problem has spawned a huge number of papers; mainly concerned with the development of computational algorithms where, in a continuous drive to demonstrate the superior accuracy and stability properties of their latest numerical method, authors have applied it to one of the problem's two-dimensional rectangular or three-dimensional cubic forms.

Unsurprisingly, the majority of papers dealing with the numerical solution to the lid-driven cavity problem have been concerned with the two-dimensional problem, and accordingly and for the sake of brevity we will confine our literature review to computations in rectangles. In earlier papers the finite difference method was prominent and was adopted, for example, by Gatski et al. [54] (who used a velocity-vorticity formulation), Ghia et al. [57] in conjunction with a multigrid approach, Gustafson and Halasi [63, 64] who preferred the MAC method, and by Soh and Goodrich [136] and Goodrich et al. [58]. However, recent applications of finite difference schemes to the two-dimensional problem may sometimes be found in the literature: Kupferman [84], for example, used finite difference methods with a pure stream function formulation that bypassed the need for vorticity boundary conditions. More conventionally, Guo [62] used a staggered MAC-like second-order numerical scheme, applicable to either two or three-dimensional flows, for solving for flow in a two-dimensional square driven cavity at Reynolds numbers up to 3200. Papers for the two-dimensional problem incorporating finite element methods (see, for example [1, 80, 91]), finite volume methods in various guises [25, 27, 155], boundary element methods [8, 61, 60], a radial basis function network method [92] and the lattice Boltzmann method [70], have also appeared in the recent literature.

The presence of corner singularities in both the two-dimensional and three-dimensional geometries is potentially hazardous for high-order methods of the spectral or p -finite element type, due to the Gibbs phenomenon. Particularly dangerous are the singularities at the points or lines of intersection between the moving lid and stationary walls since here the velocity field is discontinuous. Various high-order methods have been employed with success despite the difficulties associated with accuracy and control of oscillations near the corner/edge singularities, however. One manner in which these difficulties have been overcome is to change the problem:

the tangential velocity on the moving lid is replaced by a polynomial that vanishes (together with at least its first derivatives) on the edges or corners where the lid and stationary walls meet. This is the so-called *regularized driven cavity problem*, assumed to have qualitatively the same dynamical properties as the driven cavity flow, and solved to good effect by, for example, Shen [132], Leriche and Deville [88] and Botella [16]. A piecewise linear approximation to the constant tangential lid velocity, made to vanish at the lid-wall singularities was used by Barragy and Carey [11] in their p -finite element approach to the two-dimensional lid-driven problem. No modification was made to the original problem by Henderson [69] in his hp -adaptive spectral element method: his calculations sought to resolve the singularity directly through mesh refinement near the corners. Arguably, the most satisfactory solution to the lid-driven problem is to subtract off the leading part of the known asymptotic form of the Navier-Stokes singularity, leaving a more regular problem to be tackled, say, by a Chebyshev collocation method. This is what was done by Botella and Peyret [17, 18]. Of course, corner singularities between a stationary and a moving wall of the type described by the asymptotic expansions of Moffatt [101] and Botella and Peyret [18], amongst others, are physically unrealizable. The infinite acceleration of fluid particles implied by the change of boundary conditions requires an infinite stress at the corner. This observation was made by G.I. Taylor in 1962 in the context of the now famous “scraper problem” [141]. What may be envisaged happening in reality for the lid-driven cavity problem is that fluid leaves or enters the cavity through “leaks” along the lines of contact between the vertical walls and the moving lid. The unregularized lid-driven cavity problem is thus a mathematical idealization of the physical problem (and all the more so when one confines the flow to two dimensions!) However, Hansen and Kelmanson [66] have shown that as the leak heights tend to zero excellent agreement between the leaky and unregularized problems may be obtained. In the present work we insert leaks across the heights of the finite volumes in the corners between the lid and the vertical walls for the two-dimensional problem. Although this regularizes the problem somewhat, the leak heights are only 5.7656×10^{-5} for the finest mesh used in our computations in the unit square.

There are several difficulties with many of the approaches cited in the previous paragraphs. The primitive variable form of the Navier-Stokes equations is difficult to solve due to lack of an independent equation for the pressure term. Velocity-vorticity formulations of the Navier-Stokes equations have advantages over the velocity-pressure-based equations in that the pressure term is eliminated from the equations, and the well-known difficulty associated with wall pressure boundary conditions is avoided. However, a potential difficulty with this approach is that the vorticity value on the wall is not generally known a priori. Moreover, with the majority of three-dimensional velocity-vorticity methods it is necessary to solve three transport equations for the vorticity components and three Poisson equations for the velocity components [36]. For a discussion of the issue of vorticity boundary conditions, as well as a description of a new velocity-vorticity method requiring no vorticity boundary conditions and the determination of only N primary variables for N -dimensional problems ($N = 2, 3$), the reader is referred to [36]. For earlier general reviews of the mathematical formulation of the incompressible Navier-Stokes equations we refer to [52, 59] where a large number of references are mentioned.

The finite volume method proposed in this thesis involves multiplication of the primitive variable-based momentum equation with the unit vector normal to a control volume boundary as described in Section 1.1. Integration thereafter around the boundary of the same control volume thus eliminates the pressure term from the governing equations. Therefore any difficulty associated with the pressure term is avoided in a similar manner to that achieved by the

velocity-vorticity formulation. Our method possesses two significant advantages over the majority of velocity-vorticity methods, however. First, unlike most velocity-vorticity formulations, no vorticity boundary conditions are required on the wall, since the resulting equations are expressed solely in terms of the velocity components. Only no-slip velocity boundary conditions are required. Secondly, the number of primary variables that need to be determined equals the number of space dimensions. The new velocity-vorticity formulation of Davies and Carpenter [36] referred to above also possesses these advantages over traditional velocity-vorticity methods. However, the method of Davies and Carpenter has been largely presented in the context of the disturbance equations in boundary layer flow and their method requires that the primary variables be constrained to satisfy certain limiting conditions. The method used in the present thesis suffers from neither of these limitations and since the primary variables are just the components of velocity, no determination of secondary variables in an iterative or time-marching scheme is required. The implementation in this respect is thus straightforward.

In addition to requiring no vorticity or pressure boundary conditions and using only the velocity components as primary variables, our finite volume method is fully implicit. Implicit finite volume methods have enjoyed widespread use in the literature, due in part, no doubt, to their attractive stability properties and the utility of finite volume methods for problems defined in complex geometries. Confining our attention to just the past five years, for example, implicit finite volume methods have been employed to good effect for computing the evolution of surfactant concentration in investigations of the effects of surfactants on the rheological properties of emulsions [118] and on the shape of fluid interfaces in Stokes flow [117]. They have also been used in the simulation of three-dimensional mould filling problems in injection moulding [28]. Three-dimensional time-dependent viscoelastic flows have been tackled with implicit finite volume methods [156, 157], and they have seen service in the numerical modelling of turbulence [97, 130]. Some attention in the literature has been given to the development and implementation of Krylov subspace methods for the resolution of the algebraic systems arising from a discretization using implicit finite volume methods of the convection-diffusion-reaction partial differential equations that describe the partially ionized flow in the boundary layer of a tokamak fusion reactor [130]. Comparisons have also been made of different Krylov subspace methods (GMRES, BiCGStab etc.) for the solution of the algebraic systems of equations arising from an implicit finite volume approximation of the Navier-Stokes equations on unstructured grids [96]. For an analysis of cell-vertex finite volume methods for the cases of pure convection and convection-diffusion problems, the reader is referred to the papers of Morton and Stynes [103] and Morton et al. [104].

This chapter of the thesis is dedicated to a discussion of the numerical results obtained for the two-dimensional lid-driven cavity problem at Reynolds numbers up to 10000. Computations are performed on three meshes of increasing mesh density; with the finest of which are associated 132,098 degrees of freedom. The accuracy of the results at various Reynolds numbers in the literature for the two-dimensional driven cavity problem is usually assessed by performing a comparison of the streamwise and spanwise velocity profiles along the vertical and horizontal lines of symmetry with those of other authors, or by a quantitative comparison of the stream function value at the centre of the primary vortex, for example. Similar comparisons may be found in the present chapter for the steady problem. Additionally, we consider convergence of the RMS value of the update vector for the velocity field in our Newton method, and demonstrate that this tends to zero in magnitude exponentially fast. Smooth solutions, in good (sometimes even excellent) agreement with those in the literature, are presented.

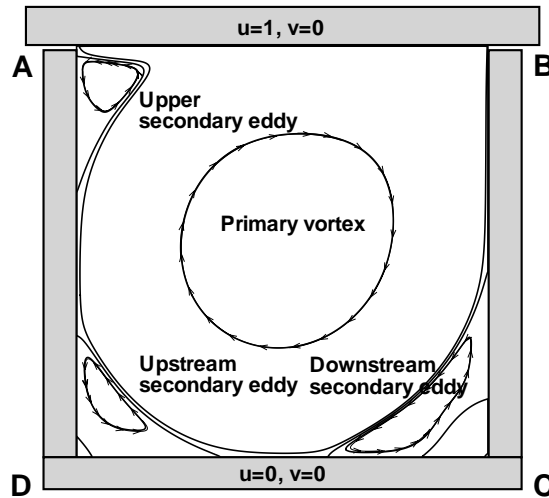


Figure 3.1: Lid-driven cavity boundary conditions with the basic features of cavity flow

3.2 Numerical Results

In order to verify its accuracy at high Reynolds numbers and compute the base flow required for a linear stability analysis, the present fully-implicit velocity formulation, described in Section 1.1, is applied to lid-driven cavity flow in a square $[0, 1] \times [0, 1]$, as shown in Fig. 3.1. The singularities situated between the lid and the cavity walls (at points *A* and *B* of Fig. 3.1), are handled by introducing “leaks” over the height of the upper corner finite volumes. In fact, this is the most suitable way of applying the physical boundary conditions. The mass flow between the lid and the cavity wall weakens the primary vortex strength within the cavity, depending on the size of the leaks. As the size of these leaks approaches zero, however, the solutions converge towards the solutions obtained with the physically unrealizable boundary conditions [66].

In the present work three different grids are employed: coarse (M1: 129×129 grid points), medium (M2: 193×193 grid points) and fine (M3: 257×257 grid points), in order to investigate grid dependency of the solution. These are shown in Fig. 3.2. The smallest finite volume cells are those situated at corners *A* and *B* and have heights 1.1665×10^{-4} , 7.7170×10^{-5} and 5.7656×10^{-5} for the coarse, medium and fine grids, respectively. As mentioned above, these cell sizes correspond to the size of the leaks between the lid and the vertical cavity walls. As may be seen in Fig. 3.2, the highest density of grid points is to be found near the lid and walls. This is done in order to make the size of the leaks as small as possible and to resolve adequately the very thin boundary layers on the lid and cavity walls. As will be seen from the vorticity plots (see Fig. 3.4) strong vorticity gradients occur on the lid and the cavity walls.

3.2.1 The lid-driven cavity problem: steady flow

The first numerical results correspond to the solution of the steady Navier-Stokes equations on the finest grid (M3) at Reynolds numbers ranging from 0 to 10000, where the Reynolds number for this flow is based on the lid velocity and cavity height. For the solution of the steady Navier-Stokes equations, Newton’s method is used, as explained in Section 2.2. The

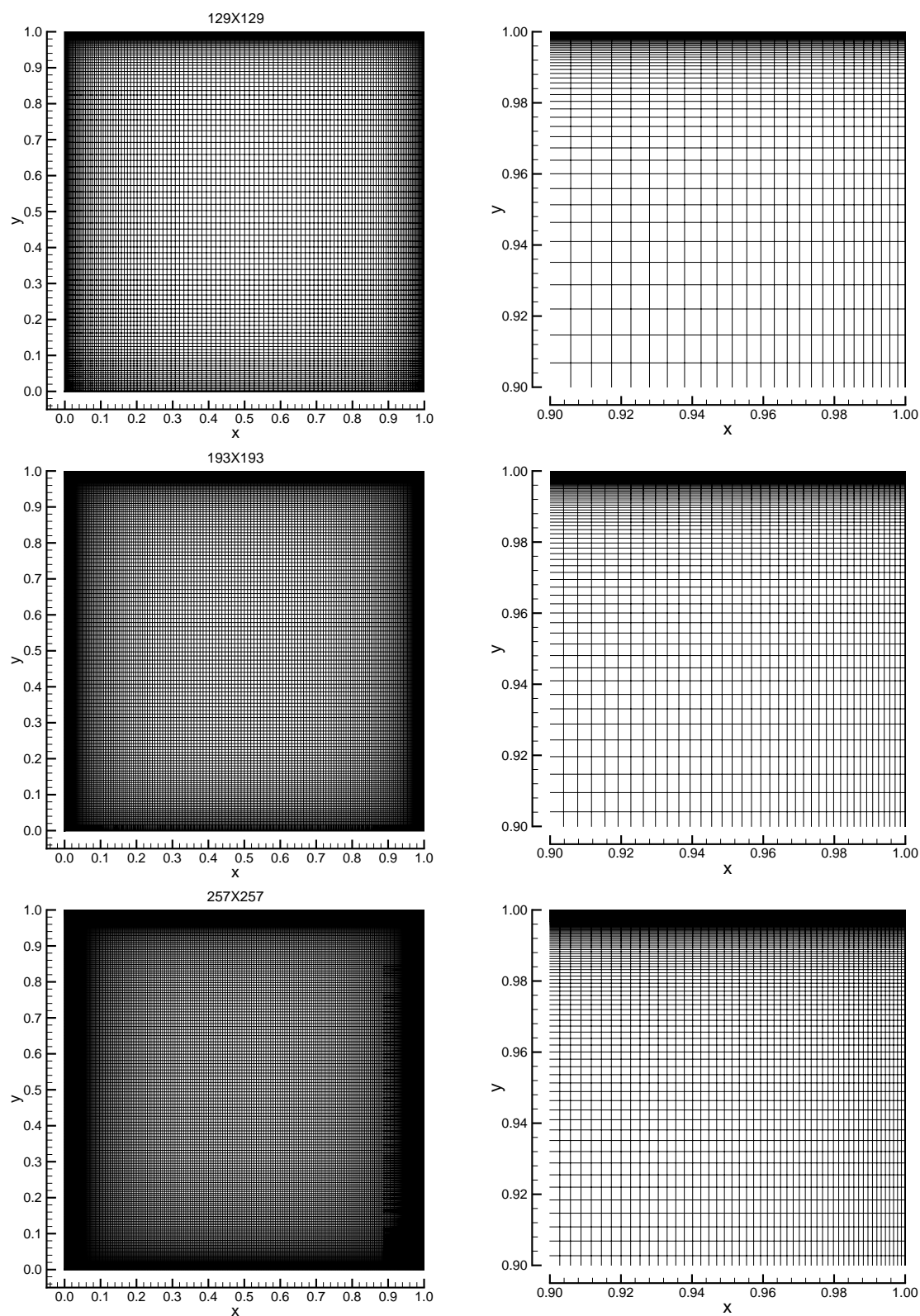


Figure 3.2: The three computational meshes (with detail of the top right-hand corner) used for the calculations presented in this chapter. Top to bottom: Mesh M1 (129×129 grid points), Mesh M2 (193×193 grid points), Mesh M3 (257×257 grid points)

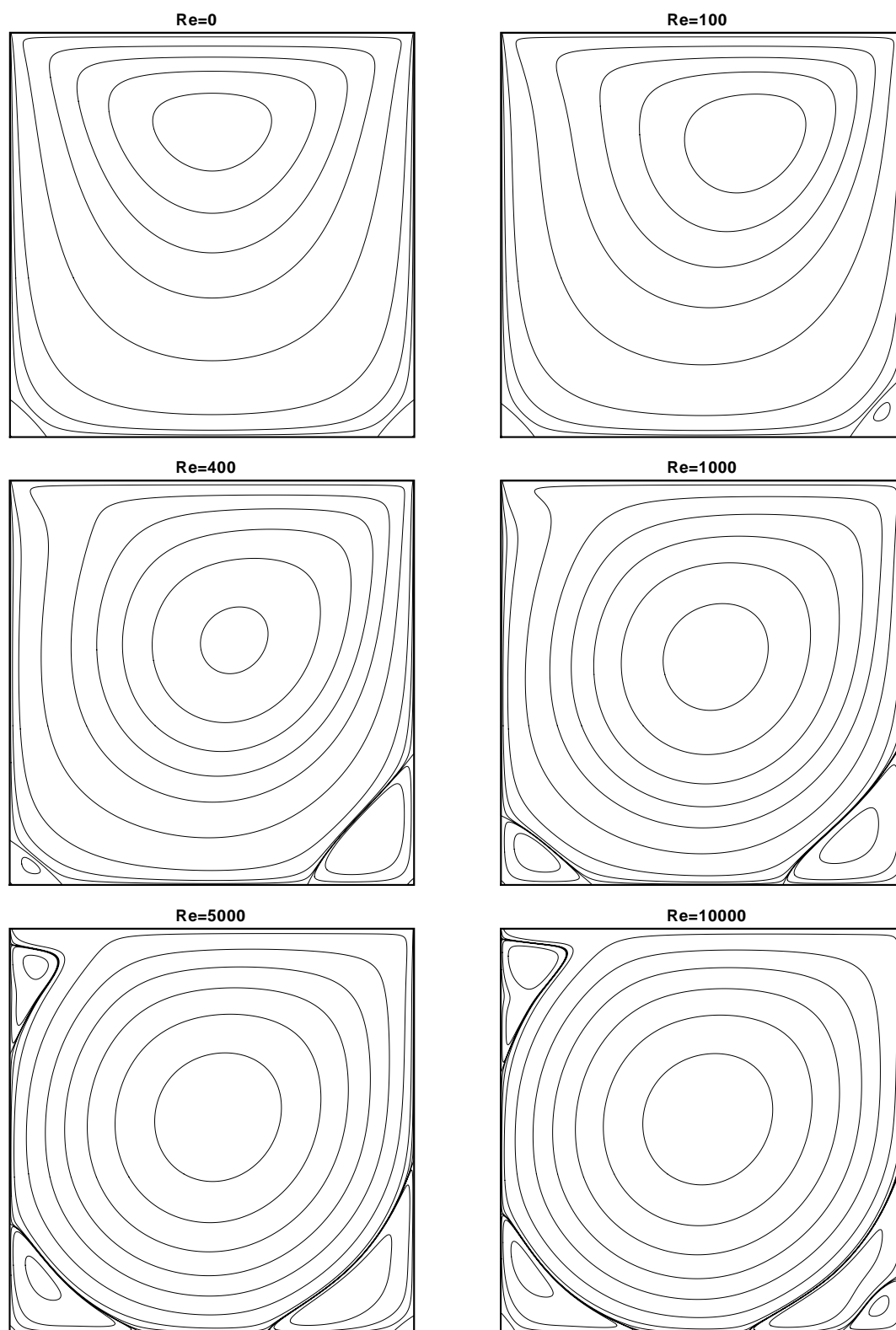


Figure 3.3: Streamlines computed with mesh M3. Reynolds numbers from 0 to 10000. The stream function equals 0 on the cavity boundary and the contour levels shown for each plot are -0.11, -0.09, -0.07, -0.05, -0.03, -0.01, -0.001, -0.0001, -0.00001, 0.0, 0.00001, 0.0001, 0.001 and 0.01

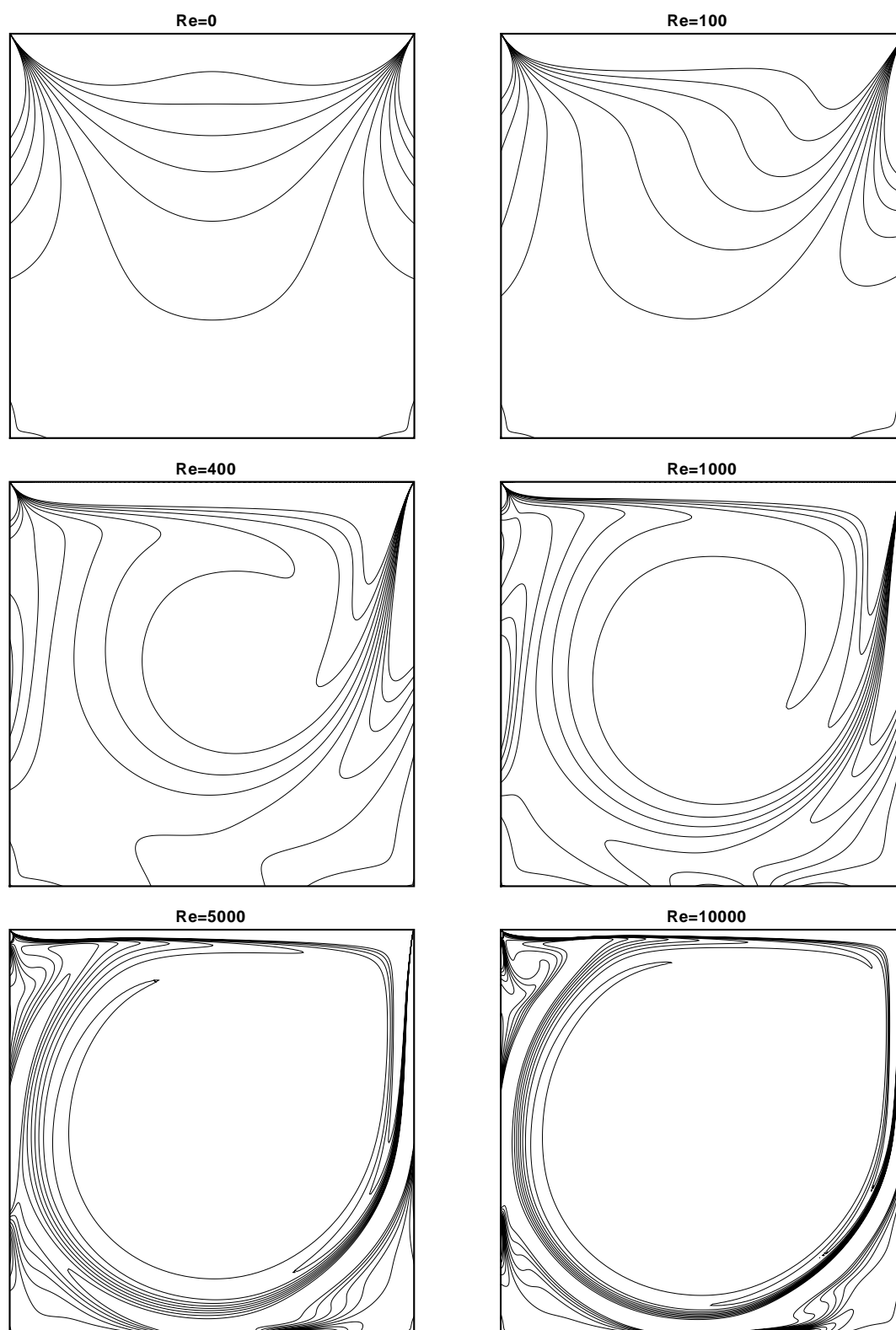


Figure 3.4: Contours of vorticity computed with mesh M3. Reynolds numbers from 0 to 10000. Contour levels shown for each plot are -5.0, -4.0, -3.0, -2.0, -1.0, 0.0, 1.0, 2.0, 3.0, 4.0 and 5.0

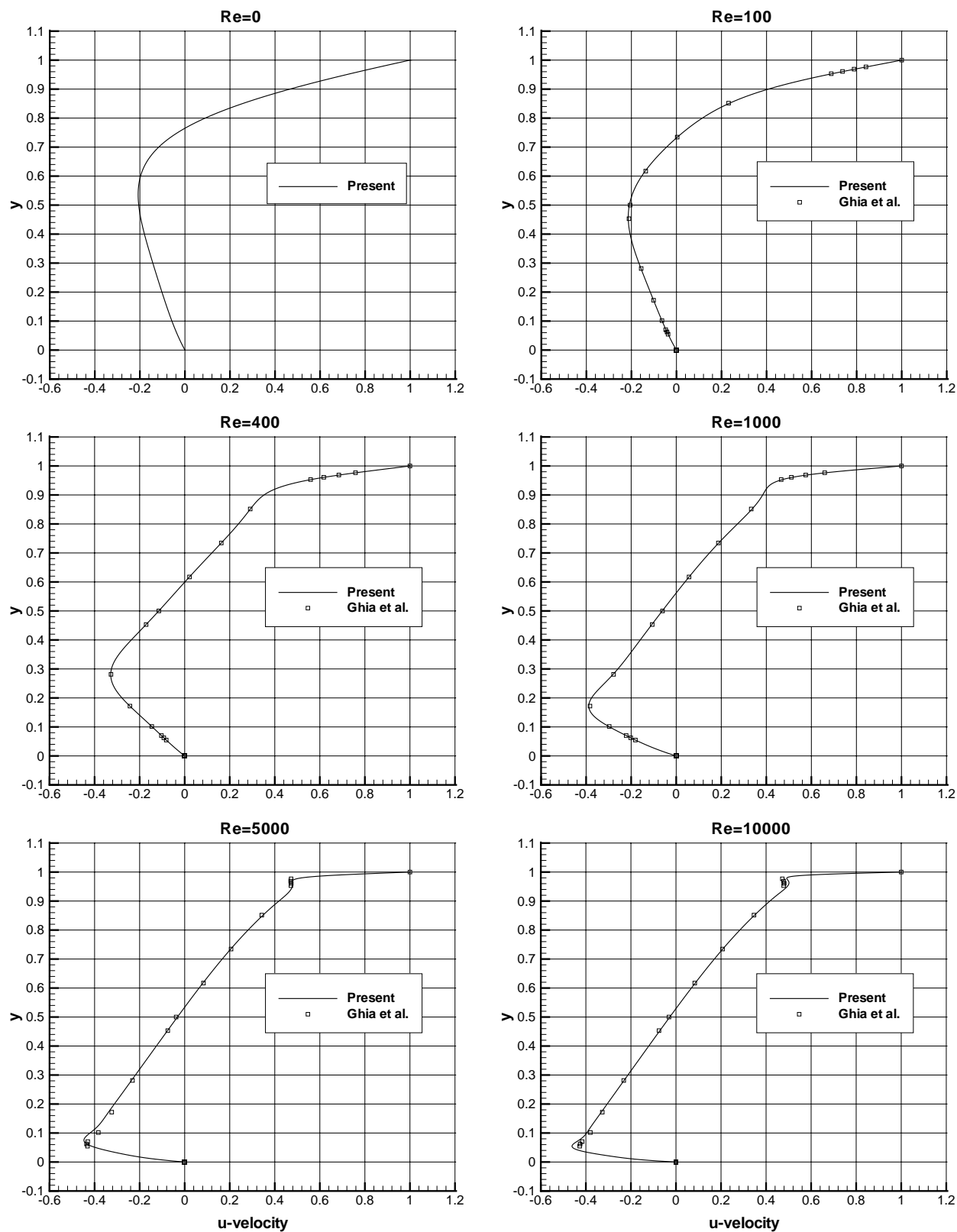


Figure 3.5: Profiles of u along the line $x = 0.5$ computed with mesh M3. Reynolds numbers from 0 to 10000. Also shown are the results (\square) of Ghia et al. [57]

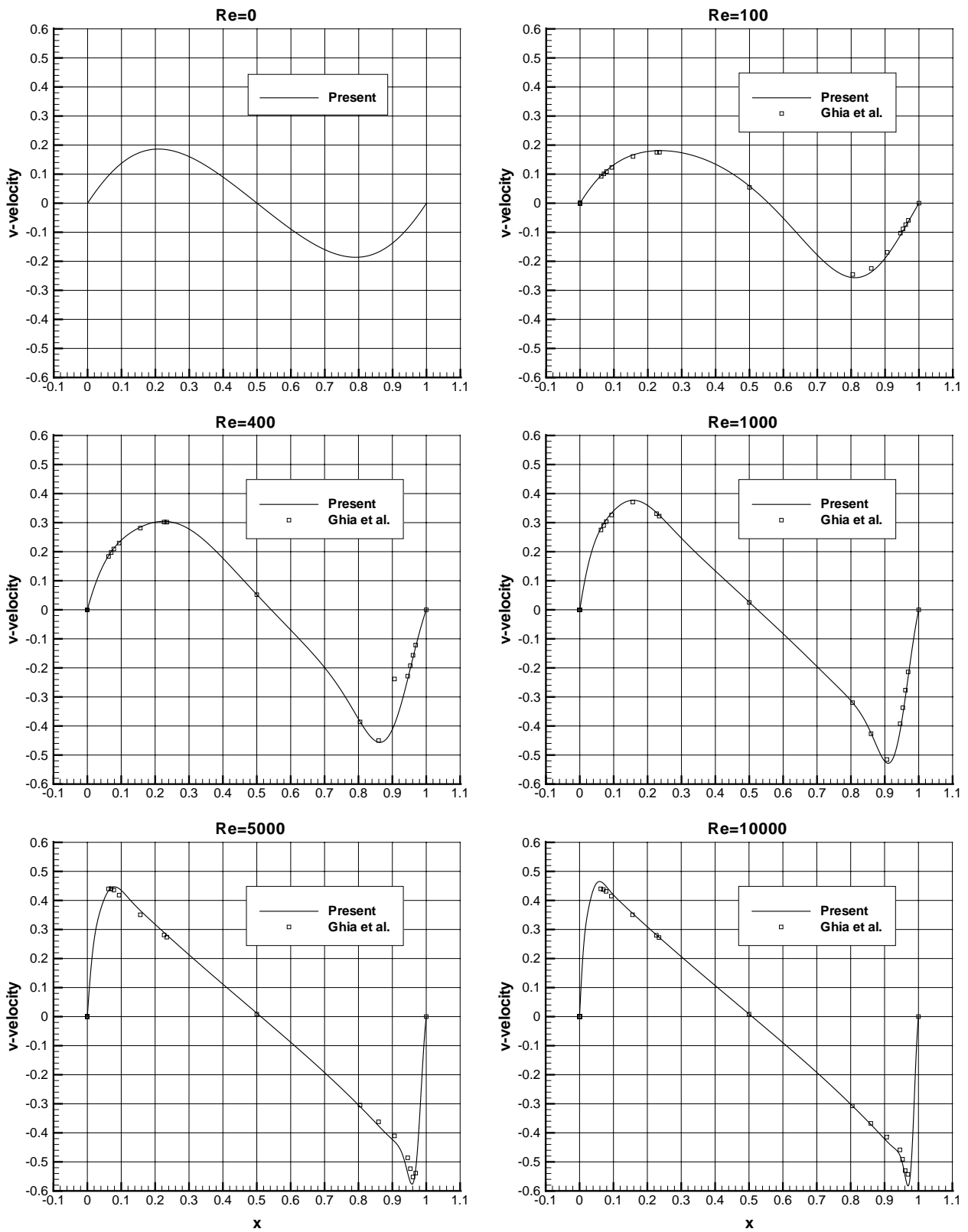


Figure 3.6: Profiles of v along the line $y = 0.5$ computed with mesh M3. Reynolds numbers from 0 to 10000. Also shown are the results (\square) of Ghia et al. [57]

Table 3.1: Table of vorticity values at the primary vortex centre. Mesh M3.

Re	vorticity at primary vortex centre
0	-3.2208
100	-3.1655
400	-2.2950
1000	-2.0664
3200	-1.9593
5000	-1.9392
7500	-1.9275
10000	-1.9231

initial conditions for Newton's method are calculated from the direct solution of Stokes flow. Then the flow at $Re = 100, 400, 1000, 3200, 5000, 7500$ and 10000 is solved using the previous solution as an initial condition.

The computed streamlines are presented in Fig. 3.3. At $Re = 0$, the streamlines and vorticity contours are symmetric about the vertical centreline of the cavity. At the lower corners upstream and downstream secondary eddies are visible and are equal in size. Although the analytical solution predicts an infinite number of exponentially decaying eddies at the corners [101], it is not possible to resolve these eddies with a finite number of grid points. At a Reynolds number of around 100, the primary vortex moves towards the right-hand wall and the downstream secondary eddy starts to enlarge in size. At a Reynolds number of 400, the primary vortex starts to move towards the cavity centre and it continues to move to the centre even at high Reynolds numbers. Evidence of growth in the upstream secondary eddy at a Reynolds number of 400 is also now visible. If the Reynolds number is increased further another secondary eddy emerges on the upper left-hand cavity wall. Further increases in the Reynolds number makes visible tertiary level vortices. It might be considered surprising that smooth solutions at these high Reynolds numbers are possible with a central difference scheme. However, Hafez and Soliman [65], who also used a central difference scheme, presented solutions of the steady Navier-Stokes equations for the lid-driven cavity problem at Reynolds numbers up to 30000 obtained using a Newton method combined with a direct solver.

In Fig. 3.4 we note that as the Reynolds number increases the vorticity contours move away from the cavity centre towards the cavity walls and indicates that very strong vorticity gradients develop on the lid and the cavity walls (especially the right-hand vertical wall) for higher Reynolds numbers. In contrast, in the centre of the cavity almost no vorticity gradient is evident at all. The fluid begins to rotate like a rigid body with a constant angular velocity. The vorticity values at the centre of the primary vortex - as computed with mesh M3 - are shown in Table 3.1. As the Reynolds number increases there is a clear trend towards the theoretical infinite Re value of -1.886 (see Burggraf [21]).

For an assessment of the accuracy of the present results, the velocity components through the vertical and horizontal centrelines of the cavity are compared with the corresponding numerical results of Ghia et al. [57] in Figs. 3.5 and 3.6. The comparison shows good agreement, particularly at Reynolds numbers up to 5000. However, at a Reynolds number of 10000 the present method (featuring a non-uniform grid) gives slightly higher extremal values of the velocity components since it is difficult to resolve the very thin boundary layer

Table 3.2: Table of (a) minimum values of u computed along $x = 0.5$ and the corresponding ordinate y_{min} , (b) maximum values of v computed along $y = 0.5$ and the corresponding abscissa x_{max} , (c) minimum values of v computed along $y = 0.5$ and the corresponding abscissa x_{min} , (d) minimum values of ψ and the corresponding coordinates x_{min}, y_{min} .

Reference	u_{min}	y_{min}	v_{max}	x_{max}	v_{min}	x_{min}	ψ_{min}	x_{min}, y_{min}
Re=0								
Present	-0.207754	0.5376	0.186273	0.2105	-0.186273	0.7894	-0.100054	0.5000,0.7626
Botella & Peyret [17].	-	-	-	-	-	-	-0.100076	-
Re=100								
Present	-0.213924	0.4598	0.180888	0.2354	-0.256603	0.8127	-0.103471	0.6189,0.7400
Ghia et al. [57]	-0.21090	0.4531	0.17527	0.2344	-0.24533	0.8047	-0.103423	0.5172,0.7344
Botella & Peyret [17].	-0.214042	0.4581	0.179572	0.2370	-0.253803	0.8104	-	-
Hou et al. [70]	-	-	-	-	-	-	-0.1030	0.6196,0.7373
Bruneau & Jouron [20]	-0.2106	0.4531	0.1786	0.2344	-0.2521	0.8125	-0.1026	0.6172,0.7344
Deng et al. [37]	-0.21315	-	0.17896	-	-0.25339	-	-	-
Re=400								
Present	-0.328375	0.2815	0.304447	0.2253	-0.456316	0.8621	-0.113897	0.5536,0.6075
Ghia et al. [57]	-0.32726	0.2813	0.30203	0.2266	-0.44993	0.8594	-0.113909	0.5547,0.6055
Hou et al. [70]	-	-	-	-	-	-	-0.1121	0.5608,0.6078
Deng et al. [37]	-0.32751	-	0.30271	-	-0.45274	-	-	-
Re=1000								
Present	-0.388103	0.1727	0.376910	0.1573	-0.528447	0.9087	-0.118800	0.5335,0.5639
Ghia et al. [57]	-0.38289	0.1719	0.37095	0.1563	-0.51550	0.9063	-0.117929	0.5313,0.5625
Botella & Peyret [17].	-0.388569	0.1717	0.376944	0.1578	-0.527077	0.9092	-0.118936	0.5308,0.5652
Barragy & Carey [11]	-	-	-	-	-	-	-0.118930	-
Hou et al. [70]	-	-	-	-	-	-	-0.1178	0.5333,0.5647
Bruneau & Jouron [20]	-0.3764	0.1602	0.3665	0.1523	-0.5208	0.9102	-0.1163	0.5313,0.5586
Deng et al. [37]	-0.38511	-	0.37369	-	-0.52280	-	-	-
Re=3200								
Present	-0.435402	0.0921	0.432448	0.0972	-0.569145	0.9491	-0.121628	0.5201,0.5376
Ghia et al. [57]	-0.41933	0.1016	0.42768	0.0938	-0.54053	0.9453	-0.120377	0.5165,0.5469
Re=5000								
Present	-0.447309	0.0741	0.446913	0.0799	-0.576652	0.9573	-0.122050	0.5134,0.5376
Ghia et al. [57]	-0.43643	0.0703	0.43648	0.0781	-0.55408	0.9531	-0.118966	0.5117,0.5352
Barragy & Carey [11]	-	-	-	-	-	-	-0.122219	0.5151,0.5359
Hou et al. [70]	-	-	-	-	-	-	-0.1214	0.5176,0.5373
Bruneau & Jouron [20]	-0.4359	0.0664	0.4259	0.0762	-0.5675	0.9590	-0.1142	0.5156,0.5313
Re=7500								
Present	-0.456054	0.0610	0.458048	0.0670	-0.580994	0.9649	-0.122302	0.5134,0.5289
Ghia et al. [57]	-0.43590	0.0625	0.44030	0.0703	-0.55216	0.9609	-0.119976	0.5117,0.5322
Barragy & Carey [11]	-	-	-	-	-	-	-0.122380	0.5132,0.5321
Hou et al. [70]	-	-	-	-	-	-	-0.1217	0.5176,0.5333
Bruneau & Jouron [20]	-0.4379	0.0508	0.4179	0.0625	-0.5640	0.9688	-0.1113	0.5156,0.5234
Re=10000								
Present	-0.461617	0.0549	0.465210	0.0598	-0.582351	0.9684	-0.122489	0.5134,0.5289
Ghia et al. [57]	-0.42735	0.0547	0.43983	0.0625	-0.54302	0.9688	-0.119731	0.5117,0.5333
Barragy & Carey [11]	-	-	-	-	-	-	-0.122393	0.5113,0.5302
Bruneau & Jouron [20]	-0.4373	0.0430	0.4141	0.0547	-0.5610	0.9727	-0.1053	0.5156,0.5234

Table 3.3: Variation in location of the secondary eddies with Re number. Mesh M3.

Re	Downstream secondary eddy		Upstream secondary eddy		Upper secondary eddy	
	x_{max}, y_{max}	ψ_{max}	x_{max}, y_{max}	ψ_{max}	x_{max}, y_{max}	ψ_{max}
0	0.9630,0.0378	0.222065E-05	0.0369,0.0378	0.222065E-05	-	-
100	0.9424,0.0610	0.126584E-04	0.0332,0.0352	0.179303E-05	-	-
400	0.8835,0.1203	0.640440E-03	0.0508,0.0461	0.142720E-04	-	-
1000	0.8658,0.1119	0.172397E-02	0.0826,0.0776	0.233014E-03	-	-
3200	0.8259,0.0847	0.282335E-02	0.0799,0.1203	0.111207E-02	0.0530,0.8984	0.705801E-03
5000	0.8081,0.0741	0.306508E-02	0.0720,0.1382	0.136890E-02	0.0621,0.9108	0.143828E-02
7500	0.7894,0.0642	0.322261E-02	0.0645,0.1525	0.151998E-02	0.0670,0.9108	0.211980E-02
10000	0.7796,0.0610	0.319479E-02	0.0598,0.1624	0.159044E-02	0.0694,0.9108	0.261144E-02

with a uniform grid, even with one as fine as the 257×257 grid of Ghia et al. [57]. As may be seen from Figs. 3.5 and 3.6, as the Reynolds number increases the extremal values of the velocity components increase in magnitude and the turning points get progressively closer to the wall. The values of the extrema in the velocity components and the minimum values of the stream function are given in Table 3.2 and are compared with other results in the literature. Although the results at low Reynolds numbers are in good agreement, at high Reynolds number they deviate from each other, particularly at $Re = 10000$. The present results are in very close agreement with those of Barragy and Carey [11] and the maximum difference in the minimum value of the stream function computed by these authors and by us is less than 0.138%. The results of Botella and Peyret [17], calculated with a Chebyshev collocation method and featuring subtraction of the leading part of the corner singularities, are believed to be very accurate but their results do not extend to high Reynolds numbers. In addition, in Table 3.3 we present results showing how the location of the secondary eddies change with the Reynolds number.

In order to demonstrate the convergence characteristics of the present method, we calculate the RMS value $RMS(n)$ of the update vector $\delta \mathbf{u}^{n+1}$ at the $(n+1)$ th Newton iterate as

$$RMS(n) = \sqrt{\frac{1}{N_x N_y} \sum_{i,j=1}^{N_x, N_y} (u_{i,j}^{n+1} - u_{i,j}^n)^2 + (v_{i,j}^{n+1} - v_{i,j}^n)^2} = \frac{1}{\alpha \sqrt{N_x N_y}} \|\delta \mathbf{u}^{n+1}\|_2, \quad (3.1)$$

where α is the under-relaxation parameter introduced in Chapter 1 and N_x and N_y denote the number of grid points in the x and y directions, respectively. Fig. 3.7 shows a plot on a log-normal scale of $RMS(n)$ versus the iteration number n at Reynolds numbers of 100 and 10000. The figure shows an exponential decay in $RMS(n)$ and in both cases $RMS(n)$ is of the order of 1×10^{-8} after 70 Newton iterations. From our numerical experiments it would seem that the rate of convergence is independent of the Reynolds number for a sufficiently large value of α . To gain insight into why this might be so, we follow an approximate error analysis and consider the non-linear system (2.1) and (2.2) summed up over the appropriate i, j and supplemented with velocity boundary conditions. This system might be written in the form

$$\mathbf{F}(\mathbf{u}) = \mathbf{0}, \quad (3.2)$$

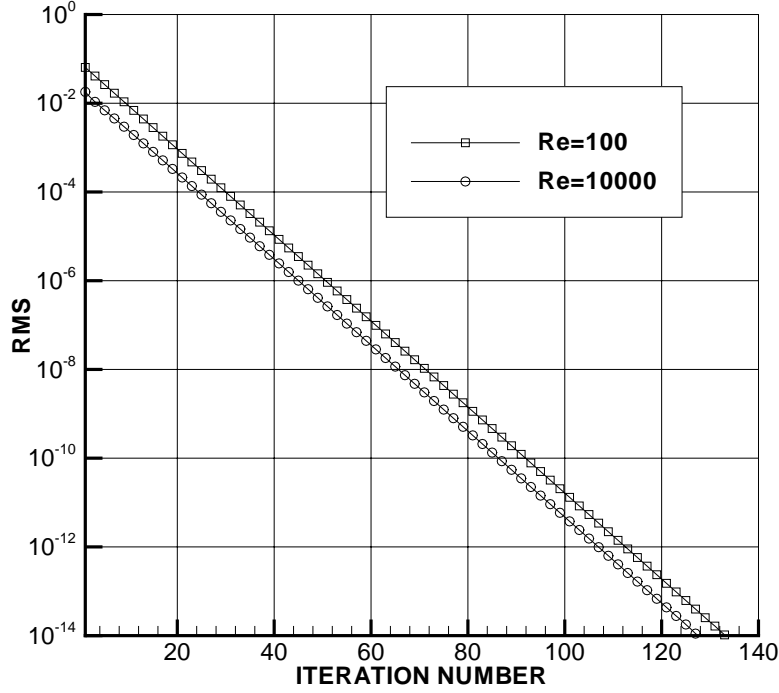


Figure 3.7: RMS value $RMS(n)$ (see Eq. (3.1)) against iteration number n . Mesh M3. $\alpha = 5.0$.

for some vector-valued functional \mathbf{F} , so that from (1.19)

$$\mathbf{u}^{n+1} - \mathbf{u}^n = -\frac{1}{\alpha} \left(\frac{\partial \mathbf{F}}{\partial \mathbf{u}} \right)_{\mathbf{u}=\mathbf{u}^n}^{-1} \mathbf{F}(\mathbf{u}^n), \quad (3.3)$$

and

$$\mathbf{u}^{n+2} - \mathbf{u}^{n+1} = -\frac{1}{\alpha} \left(\frac{\partial \mathbf{F}}{\partial \mathbf{u}} \right)_{\mathbf{u}=\mathbf{u}^{n+1}}^{-1} \mathbf{F}(\mathbf{u}^{n+1}). \quad (3.4)$$

We let ε_n denote the L_2 norm of $\mathbf{u}^{n+1} - \mathbf{u}^n$ and from (3.3) – (3.4) see that

$$\begin{aligned} \frac{\varepsilon_{n+1}}{\varepsilon_n} &= \frac{\left\| \left(\frac{\partial \mathbf{F}}{\partial \mathbf{u}} \right)_{\mathbf{u}=\mathbf{u}^{n+1}}^{-1} \mathbf{F}(\mathbf{u}^{n+1}) \right\|_2}{\left\| \left(\frac{\partial \mathbf{F}}{\partial \mathbf{u}} \right)_{\mathbf{u}=\mathbf{u}^n}^{-1} \mathbf{F}(\mathbf{u}^n) \right\|_2} \\ &\approx \frac{\left\| \left(\frac{\partial \mathbf{F}}{\partial \mathbf{u}} \right)_{\mathbf{u}=\mathbf{u}^{n+1}}^{-1} \left[\mathbf{F}(\mathbf{u}^n) - \frac{1}{\alpha} \left(\frac{\partial \mathbf{F}}{\partial \mathbf{u}} \right)_{\mathbf{u}=\mathbf{u}^n} \left(\frac{\partial \mathbf{F}}{\partial \mathbf{u}} \right)_{\mathbf{u}=\mathbf{u}^n}^{-1} \mathbf{F}(\mathbf{u}^n) \right] \right\|_2}{\left\| \left(\frac{\partial \mathbf{F}}{\partial \mathbf{u}} \right)_{\mathbf{u}=\mathbf{u}^n}^{-1} \mathbf{F}(\mathbf{u}^n) \right\|_2} \\ &= \left(1 - \frac{1}{\alpha} \right) \frac{\left\| \left(\frac{\partial \mathbf{F}}{\partial \mathbf{u}} \right)_{\mathbf{u}=\mathbf{u}^{n+1}}^{-1} \mathbf{F}(\mathbf{u}^n) \right\|_2}{\left\| \left(\frac{\partial \mathbf{F}}{\partial \mathbf{u}} \right)_{\mathbf{u}=\mathbf{u}^n}^{-1} \mathbf{F}(\mathbf{u}^n) \right\|_2}. \end{aligned} \quad (3.5)$$

Supposing that the Jacobian matrix is approximately constant, Eqn. (3.5) leads to

$$\frac{\varepsilon_{n+1}}{\varepsilon_n} \approx 1 - \frac{1}{\alpha}, \quad (3.6)$$

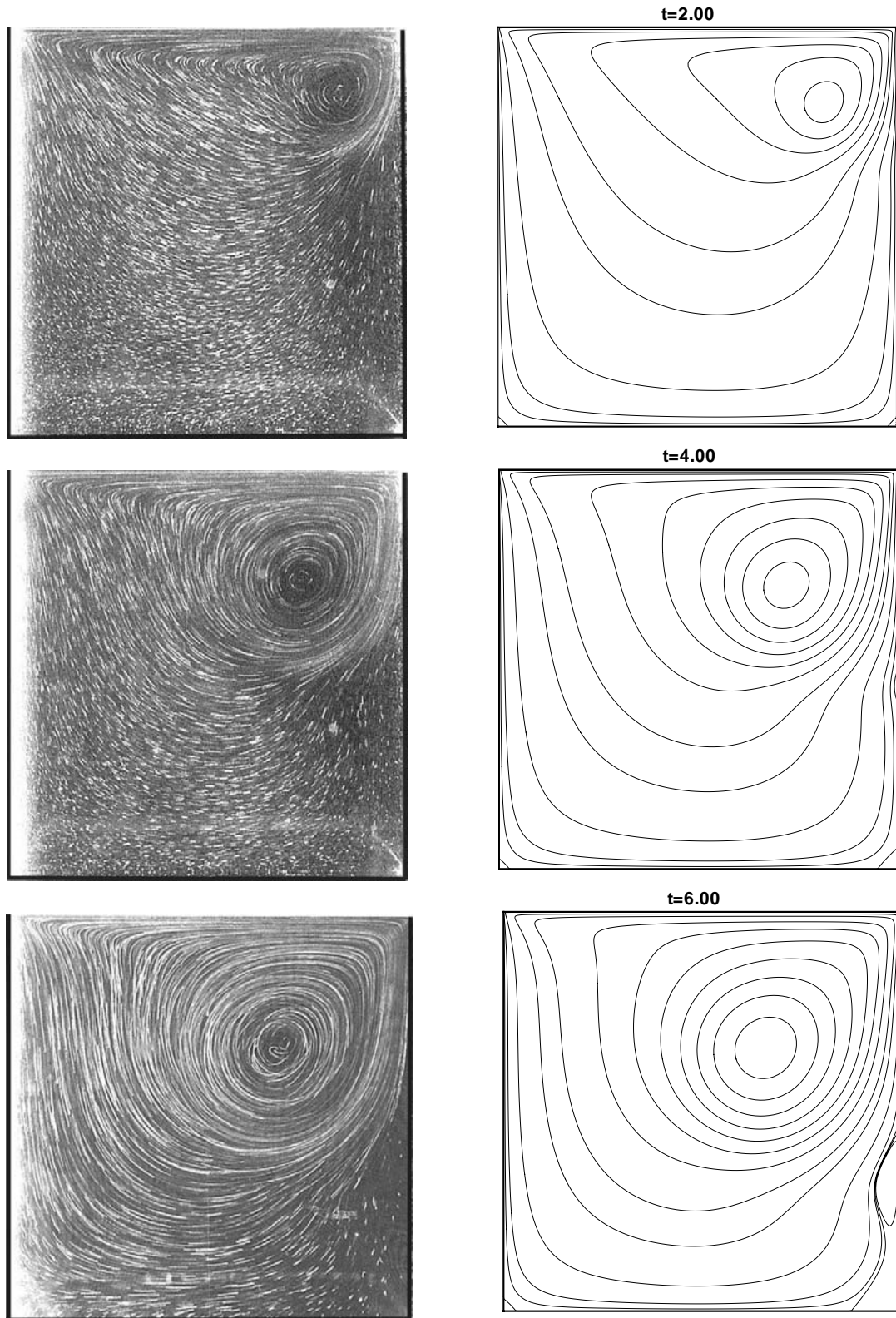


Figure 3.8: Comparison of the computed streamlines with the particle streak visualizations of Migeon et al. [99] for an impulsively accelerated lid-driven cavity problem at $Re=1000$. The contour levels are $-0.11, -0.10, -0.09, -0.08, -0.07, -0.06, -0.05, -0.04, -0.03, -0.02, -0.01, -0.005, -0.001, -0.0001, -0.00001, 0.0, 0.00001, 0.0001, 0.0005, 0.001$.

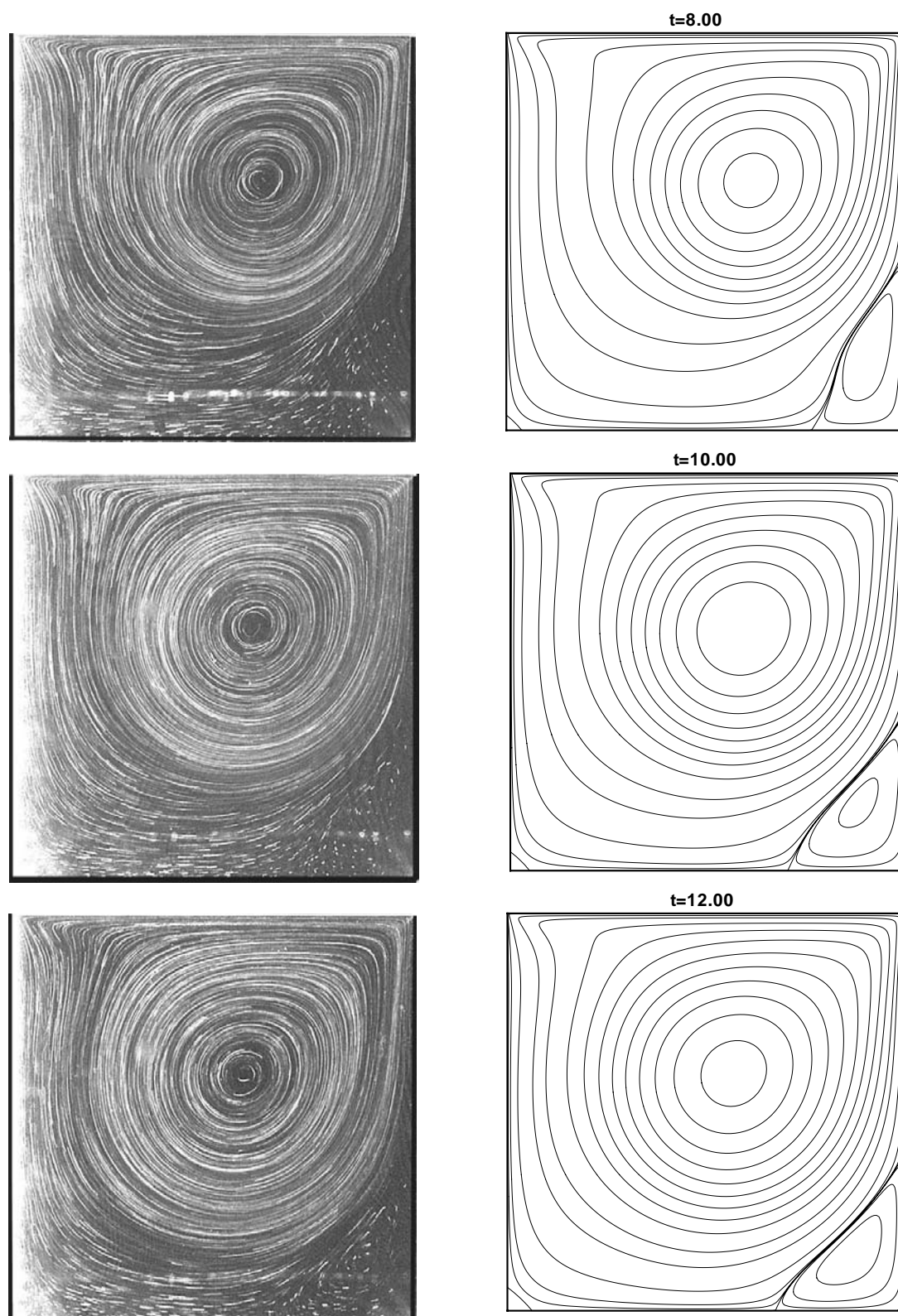


Figure 3.9: Comparison of the computed streamlines with the particle streak visualizations of Migeon et al. [99] for an impulsively accelerated lid-driven cavity problem at $Re=1000$. The contour levels are $-0.11, -0.10, -0.09, -0.08, -0.07, -0.06, -0.05, -0.04, -0.03, -0.02, -0.01, -0.005, -0.001, -0.0001, -0.00001, 0.0, 0.00001, 0.0001, 0.0005, 0.001$.

so that

$$\log \varepsilon_{n+1} - \log \varepsilon_n = \log \left(1 - \frac{1}{\alpha} \right), \quad (3.7)$$

and hence

$$\log \varepsilon_n - \log \varepsilon_0 = n \log \left(1 - \frac{1}{\alpha} \right). \quad (3.8)$$

From the above relation we computed the gradient of the function $\varepsilon_n / \sqrt{N_x N_y}$ of n and found this to be -0.0969 for $\alpha = 5.0$. This is identical to four decimal places with the slopes computed from the RMS plots for $Re = 100$ and $Re = 10000$ shown in Fig. 3.7. However this level of agreement may not hold at even higher Reynolds numbers since it may not be possible to use the same α value in order to maintain convergence. The initial value of the RMS depends upon the difference between the initial condition and the converged solution. This explains why the initial RMS value and all subsequent RMS values at $Re = 100$ are larger than those computed at the same iteration count at $Re = 10000$.

3.2.2 The lid-driven cavity problem: start-up flow

The second set of numerical results corresponds to the time-dependent direct numerical simulation of an impulsively accelerated lid-driven cavity flow at Reynolds numbers of 1000 and 10000. The computed results at a Reynolds number of 1000 are compared with the experimental results of Migeon et al. [99]. Although the authors presented their results in [99] for an impulsively accelerated lid-driven square cavity flow with a spanwise aspect ratio of 2.0, the authors kindly provided us their original particle-streak images for a square cavity flow with a spanwise aspect ratio of 5.0 which is highly two-dimensional until a non-dimensional time level of 12. The comparison of the computed streamlines with the particle-streak visualizations is given in Figs. 3.8 and 3.9 at non-dimensional time levels of 2, 4, 6, 8, 10, and 12. The comparison of the primary vortex core locations and the overall flow structure seem to be in good agreement. As indicated in [99] the primary vortex core is almost moving along the square cavity diagonal line. It may not be possible to see the secondary eddies from the particle traces clearly. However, the authors presented similar secondary eddy formations in their paper from enlarged images of particle traces. It may be seen that the size of the downstream eddy in the experiments is equal to our numerical calculations at a non-dimensional time level of 12. The evolution of the primary vortex in time is presented in Fig. 3.11. In addition to streamlines and vorticity contours the computed velocity components through the vertical and horizontal centrelines of the cavity at several non-dimensional time levels are presented in Fig. 3.10.

The streamlines of the time-dependent solutions at a Reynolds number of 10000 are presented in Fig. 3.12 at non-dimensional time levels of 2, 4, 6, 8, 10 and 12. The formation of the primary vortex and its transport towards the cavity centre may be seen clearly. On the current PC (with a 1200MHz Pentium IV processor) we could only afford to continue calculations up to a non-dimensional time level of 20, although we would like to determine at which Reynolds number a Hopf bifurcation takes place by computing time-accurate solutions. Unfortunately, near the critical Reynolds number the most dangerous eigenvalue has a real part which is very small. As a consequence, determination of whether or not a steady solution exists at a near-critical Reynolds number may take a very long time and is computationally very expensive. Therefore, in Chapter 4 we employ a linear stability analysis to determine the critical Reynolds number at which a Hopf bifurcation takes place.

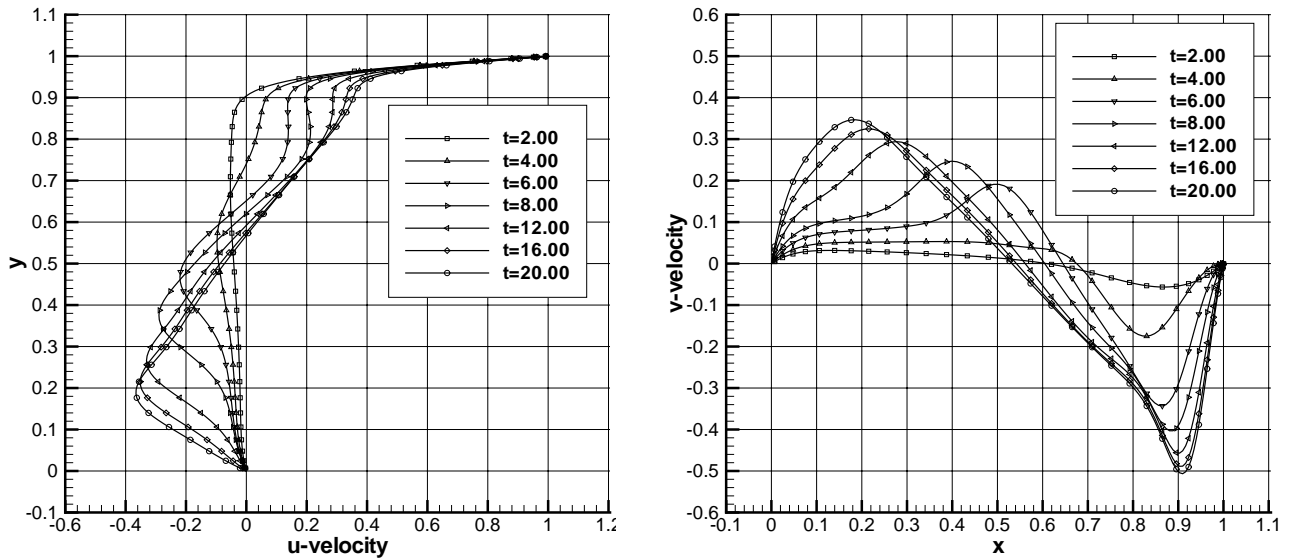


Figure 3.10: An impulsively accelerated lid-driven cavity velocity components (u, v) through the vertical and horizontal centrelines of the cavity at several non-dimensional time levels at $Re=1000$.

3.3 Conclusions

The novel finite volume method described in Section 1.1 has been used for the solution of both the steady and unsteady incompressible Navier-Stokes equations. The method involves multiplication of the primitive-variable based momentum equation with a unit vector normal to a finite volume boundary and subsequent integration of this equation along the boundary of the same control volume. Thus any difficulties associated with the pressure term or vorticity boundary conditions are obviated. The velocity components are solved in strong coupled form by using a direct solver. The method is applied to the lid-driven cavity problem for both steady and unsteady flows at Reynolds numbers up to 10000. Our solutions are smooth and in excellent agreement with benchmark results in the literature. Use of a direct solution technique ensures a solenoidal velocity field at each iterative or time step for the steady and unsteady cases, respectively.

Although we have presented only a two-dimensional application of the present method, the extension of the method to three-dimensional problems would be interesting since there are only three unknowns that would need to be determined, which is lower than both the primitive-variable-based and most velocity-vorticity formulations [36]. This may be done by imposing the continuity equation within each control volume and by computing the closed-line integral of the product of a normal vector with the momentum equation around the control volume faces in a similar manner to (1.15). A weakness of the present method, however, is that due to the linear dependence of some of the closed-line integrals, it may be difficult to match the number of equations to the number of unknowns for more complex configurations. One possible solution, for cuboidal finite volumes, at least, might be to adopt a staggered grid arrangement with velocity components now defined at the centre of the faces with respect to which they point in the normal direction.

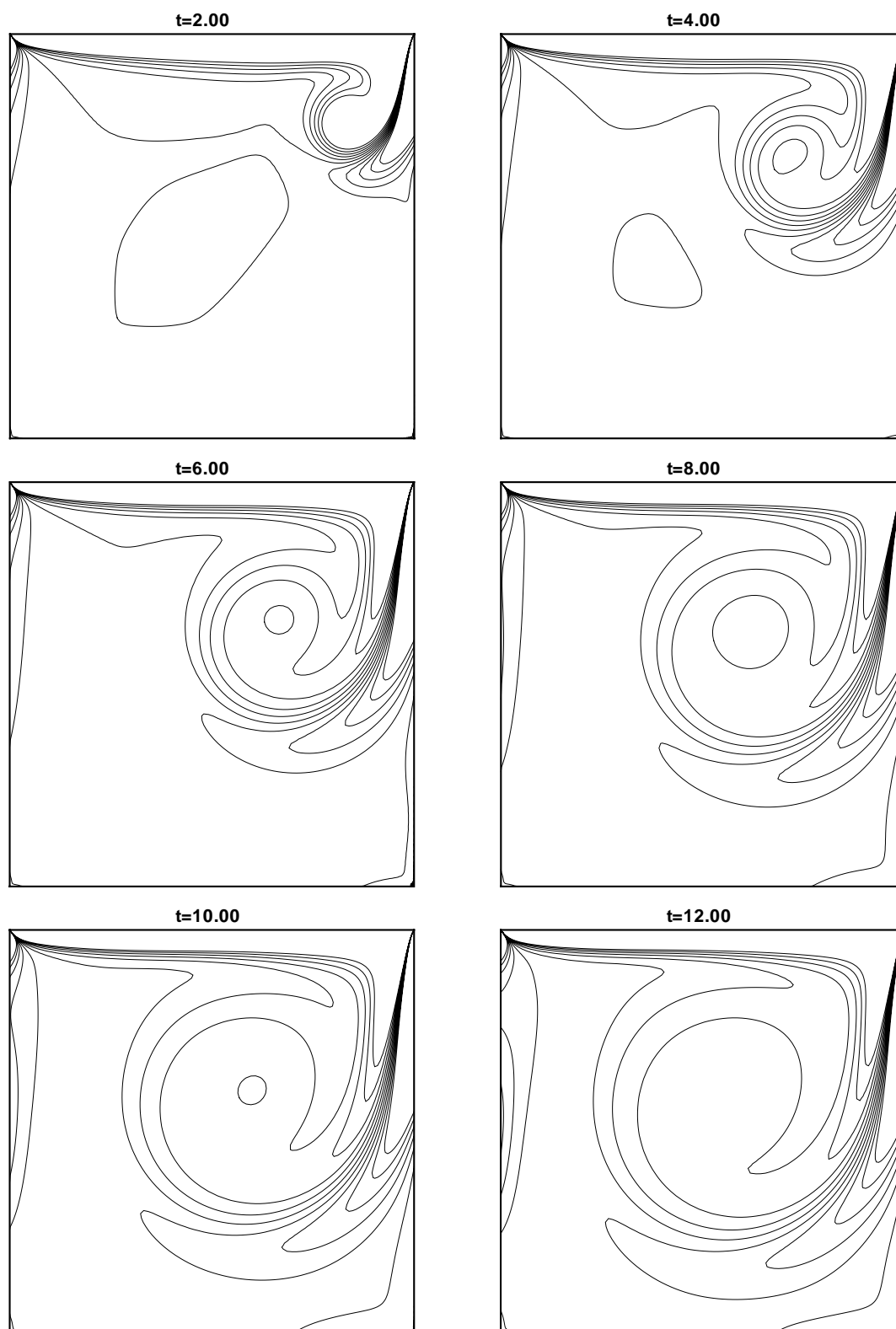


Figure 3.11: The computed vorticity contours for an impulsively accelerated lid-driven cavity problem at $Re=1000$. The contour levels are -5, -4, -3, -2, -1, 0, 1, 2, 3, 4, 5.

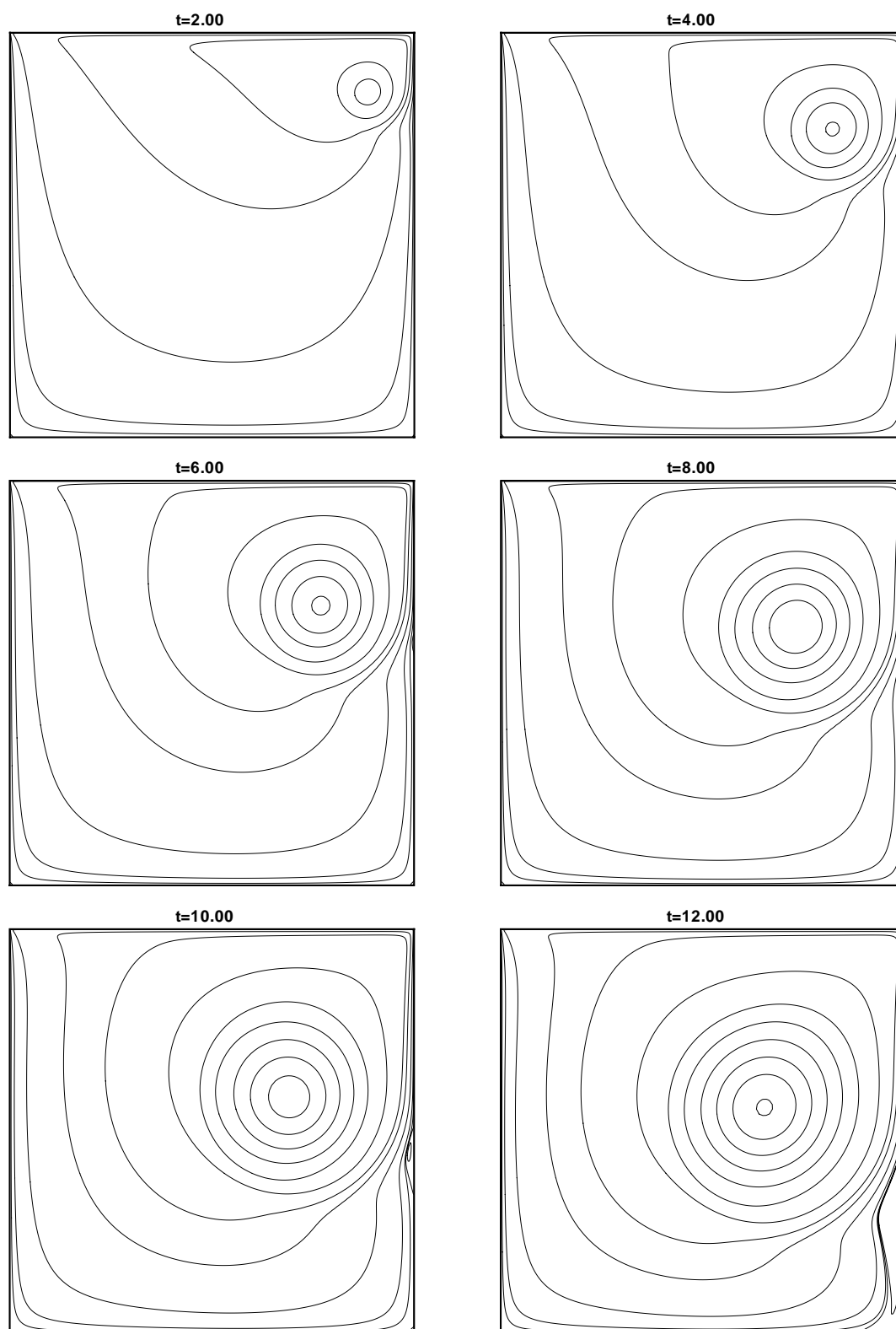


Figure 3.12: Contours of computed streamlines with mesh M2 for an impulsively accelerated lid-driven cavity at $Re=10000$. Contour levels shown for each plot are $-0.10, -0.09, -0.08, -0.07, -0.06, -0.05, -0.04, -0.03, -0.02, -0.01, -0.005, -0.001, -0.0001, -0.00001, 0.0, 0.00001, 0.0001, 0.001$ and 0.005

Chapter 4

Linear Stability Analysis of a Lid-Driven Cavity Flow

4.1 Introduction

The problem of lid-driven cavity flow of a Newtonian fluid is a particularly alluring one for the computational fluid dynamicist in view not only of the simplicity of the flow geometry - making for easy meshing - but also the richness of the fluid mechanical phenomena realizable at various Reynolds numbers: corner eddies, flow bifurcations and transition to turbulence, amongst them. For a detailed but readable treatise of the fluid mechanics in the driven cavity, the reader is referred to that of Shankar and Deshpande [131].

In the literature, however, in contrast with the proliferation of papers evaluating the performance of computational algorithms for the incompressible Navier-Stokes equations in the lid-driven cavity problem, only a handful of papers consider the question of the linear stability of this flow. In conformity with expectation, given the reduced severity of the lid-wall singularities, the regularized lid-driven cavity problem is more stable than in the unregularized case. Taking a tangential velocity profile $u(x) = 16x^2(1-x)^2$ along the lid $\{(x, 1) : 0 \leq x \leq 1\}$ in the two-dimensional case, Shen [132] was able to compute steady solutions for Reynolds numbers up to 10000. However, taking the steady solution at $Re = 10000$ as initial data, a periodic solution was found at $Re = 10500$; his Chebyshev code thus indicating the presence of a Hopf bifurcation somewhere in the interval $[10000, 10500]$. Another bifurcation was believed to occur at a critical Reynolds number in the interval $[15000, 15500]$ with the flow becoming two-periodic. Both Batoul et al. [12] and Botella [16] confirmed Shen's observation of a Hopf bifurcation at a critical Reynolds number in the range $[10000, 10500]$ by computing a solution to the same regularized problem at a Reynolds number of 10300 starting from a steady solution at $Re = 10000$. In both cases a periodic flow was reached, the period based on the kinetic energy being 3.03 for Batoul et al. and 3.0275 for Botella. A finite element method, in combination with the simultaneous inverse iteration method of Jennings [75], was used by Fortin et al. [50] in 1997 to compute a subset of the eigenvalues for the linear stability problem. The first critical eigenvalue was found at a Reynolds number of approximately 10255, consistent with the results of Shen [132]. However, the calculated fundamental frequency for the periodic flow was $f \approx 0.331$; rather different from that of Shen. Recent computations by Leriche and Deville [88] for the same regularized problem at a Reynolds number of 10500 yielded a periodic solution with fundamental frequency $f \approx 0.330$, in good agreement with previous results.

As a case in between the regularized lid profile of Shen [132] and the unregularized constant lid-velocity $u(x) = 1$, Leriche and Deville [88] also considered the high-order polynomial approximation $u(x) = (1 - x^{14})^2$ where the lid was now defined to be $\{(x, 1) : -1 \leq x \leq 1\}$. A direct numerical simulation by the authors with their Chebyshev- τ method at $Re = 8500$ gave rise to a periodic solution with fundamental frequency 0.434 and a kinetic energy signal exhibiting a period of 2.305. Thus the critical Reynolds number had already been exceeded.

The solution to the high-order regularized problem obtained by Leriche and Deville [88] was in good agreement with the results of computations by other authors on the unregularized problem: in two recent papers Pan and Glowinski [114] and Kupferman [84] both obtained limit cycle solutions at $Re = 8500$ with the kinetic energy period of Kupferman's calculations equal to 2.5 approximately. The results of Botella and Peyret [18] indicated a kinetic energy period of 2.246 at a Reynolds number of 9000.

It would seem that very few authors have wished to commit themselves to stating a value for the first critical Reynolds number Re_{crit} for lid-driven cavity flow. The reasons for this would certainly include the cost of determining the Hopf bifurcation point, as well as the computational difficulties associated with its accurate evaluation. For a detailed consideration of these points we refer the reader to the discussion by Poliashenko and Aidun [115] where three types of strategy (time evolution, test function and direct approaches) for analyzing the stability of equilibrium states and their bifurcation are presented. Additionally, we should add that the computation of the critical Reynolds number is a stringent test of the quality of the numerics, and more so, possibly, than that which is involved in comparisons of various variable values (stream function, velocity components etc.) This is borne out in the numerical results to be presented in this chapter, but the magnification brought to bear by critical Reynolds number calculations on the differences between one scheme and another has been seen already in the literature, in the comparison performed by Gervais et al. [56], for example, of differing finite element discretizations for lid-driven flow. Interestingly in this paper the introduction of SUPG-type stabilization via an enrichment of the velocity trial space with cubic bubbles led to an over diffusive scheme and a critical Reynolds number (9200) which was well outside the range predicted by the second-order finite elements tested. Thus streamline upwinded methods, although enhancing stability may compromise accuracy to the point that the predicted critical Reynolds numbers are of questionable value. No upwinding or artificial viscosity model is used in the finite volume scheme described in this thesis.

Although, at the time of writing, the first critical Reynolds number for the square two-dimensional lid-driven cavity problem is still not known, a consensus seems to be emerging that $Re_{crit} \approx 8000$. Poliashenko and Aidun [115] used a direct method for the computation of the critical Reynolds number by augmenting the generalized eigenvalue problem with normalizing conditions on the real and imaginary parts of the eigenvectors. Re_{crit} was then determined as part of the solution of the enlarged system and on their finest mesh a value of $Re_{crit} \approx 7763$ was predicted with a fundamental frequency of about 2.863. Excellent agreement with the Poliashenko and Aidun value was obtained by Cazemier et al. [26]. The authors employed a proper orthogonal decomposition (POD) of the flow in a square cavity at $Re = 22,000$ in order to construct a low-dimensional model for driven cavity flows. Only the first 80 POD modes were used but these were shown to capture 95% of the fluctuating kinetic energy. By linear extrapolation of the real parts of the most dangerous eigenvalues computed using the 80 dimensional model, Cazemier et al. predicted a critical Reynolds number of 7819, just 0.7% greater than that of Poliashenko and Aidun. A second-order finite element method

and the iteration method of Jennings [75], enabled Fortin et al. [50] to conclude that the critical Reynolds number was around 8000. Since the most dangerous eigenvalues crossed the imaginary axis as a complex conjugate pair, and since the amplitude of the fundamental frequency at the point of bifurcation was very small (9×10^{-5}) in their computations, sufficient evidence had been amassed by Fortin et al. to support the conclusion that the bifurcation is a supercritical Hopf bifurcation. From the scanty evidence available in the literature, two-dimensional driven cavity flow in non-square (but still rectangular) domains, or subject to three-dimensional infinitesimal perturbations, is less stable than that in square cavities with two-dimensional disturbances. See the papers of Poliashenko and Aidun [115], or of Goodrich et al. [58].

The present chapter is dedicated to a discussion of the numerical results for a lid-driven cavity problem in a square enclosure. Computations are performed on three meshes M1-M3 as shown in Fig. 3.2 of Chapter 3; with the finest of which are associated 132,098 degrees of freedom. For the linear stability calculations, different size Krylov spaces in the Arnoldi method are chosen to confirm the good accuracy of the eigenspectrum near the imaginary axis. Linear interpolation of the real parts of the most dangerous eigenvalues for the three meshes and extrapolation to zero mesh size of the curve fitted to the Re_{crit} -control volume size data, give us a predicted Re_{crit} of 8031.93 - a 0.40% difference from that of Fortin et al. [50], 2.72% difference from that of Cazemier et al. [26] and 3.46% difference from that of Poliashenko and Aidun [115].

4.2 Numerical Results

The use of the steady Navier-Stokes solver described in Chapter 1 of this thesis and the Arnoldi method (see Section 2.3) applied to the GEVP in Section 2.1 enable us to compute the first critical Reynolds number at which a Hopf bifurcation occurs. This is done by inspecting the real part of the most dangerous reciprocal Ritz value pair $\hat{\mu}_{1,2}^{-1}$. For any given mesh this is done for a variety of Krylov space dimensions m and the process repeated over a range of Reynolds numbers until the real part of the aforementioned reciprocal Ritz values is positive. For reasonable accuracy the incremental step size in Reynolds number during the search for a Hopf bifurcation should be kept as small as possible. The critical Reynolds number on a given mesh is then determined by a linear interpolation between the last point on the graph of $\Re(\hat{\mu}_{1,2}^{-1})$ vs. Re having $\Re(\hat{\mu}_{1,2}^{-1}) < 0$ and the first with $\Re(\hat{\mu}_{1,2}^{-1}) > 0$. For the finest mesh the critical Reynolds number is determined to be $Re = 8069.76$. The computed streamlines and vorticity contours at this Reynolds number are given in Fig. 4.1. The complete reciprocal Ritz value spectrum computed at this Reynolds number with a Krylov subspace dimension $m = 250$ is presented in Fig. 4.2 and the values of the first ten leading eigenvalues is given in Table 4.1 for further comparison. For the eigenspectrum we observe good agreement with the results of Fortin et al. [50]. The imaginary part of the leading eigenvalue is computed on mesh M3 to be 2.8251 which is also in good agreement with the corresponding value (2.8356) of Fortin et al. [50] bearing in mind the fact that the two imaginary parts (ours and that of Fortin et al.) are computed at rather different Reynolds numbers. The critical Reynolds numbers are also computed with meshes M1 and M2. The precise critical values are tabulated in Table 4.2. The Krylov space dimension m corresponding to mesh M3 and shown in the third column is the largest that we can afford with the current PC. Columns 4 and 5 detail, respectively,

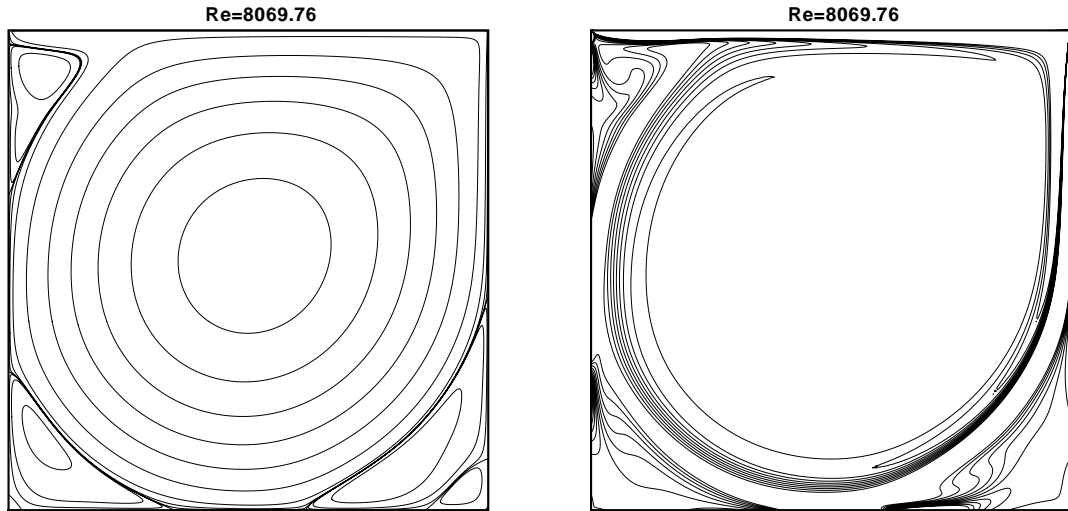


Figure 4.1: Streamlines and vorticity contours computed at critical Reynolds number of 8069.76 with mesh M3. The stream function contour levels shown are -0.11, -0.09, -0.07, -0.05, -0.03, -0.01, -0.001, -0.0001, -0.00001, 0.0, 0.00001, 0.0001, 0.001 and 0.01. Contour levels for the vorticity plot are -5.0, -4.0, -3.0, -2.0, -1.0, 0.0, 1.0, 2.0, 3.0, 4.0 and 5.0

the real and absolute value of the imaginary parts (σ_R and σ_I) of the most dangerous pair of reciprocal Ritz values computed at the interpolated critical Reynolds number. We note from the spread of values in the second column of Table 4.2 that critical Reynolds number calculations would seem to be a much more discerning measure of solution accuracy than, for example, the streamline or velocity values that are habitually presented in the literature (see Table II of [124]). Thankfully, for any given mesh, σ_R was not found to be an overly sensitive function of m . As an example, in Table 4.3 we show the ten reciprocal Ritz values having largest real parts, as computed on mesh M1 with Krylov spaces of dimensions $m = 250$ and $m = 500$. Very good agreement in both the real imaginary parts of these leading reciprocal Ritz values can be seen.

In order to estimate a value for the critical Reynolds number based on a zero mesh size (Re_{crit} , say), a relationship was sought of the form

$$Re_{crit}(h) = Re_{crit} + ch^p, \quad (4.1)$$

between Re_{crit} and the critical Reynolds number $Re_{crit}(h)$ computed on a mesh having average cell length h . Thus, identifying an average cell length h with mesh M1, we have

$$\begin{aligned} \frac{Re_{crit}(h) - Re_{crit}(2h/3)}{Re_{crit}(h) - Re_{crit}(h/2)} &= \frac{(Re_{crit}(h) - Re_{crit}) - (Re_{crit}(2h/3) - Re_{crit})}{(Re_{crit}(h) - Re_{crit}) - (Re_{crit}(h/2) - Re_{crit})}, \\ &= \frac{ch^p - c\left(\frac{2}{3}\right)^p h^p}{ch^p - c\left(\frac{1}{2}\right)^p h^p}, \\ &= \frac{1 - \left(\frac{2}{3}\right)^p}{1 - \left(\frac{1}{2}\right)^p} = \frac{8244.55 - 8109.38}{8244.55 - 8069.76}, \end{aligned} \quad (4.2)$$

which yields a solution $p \approx 2.4906$.

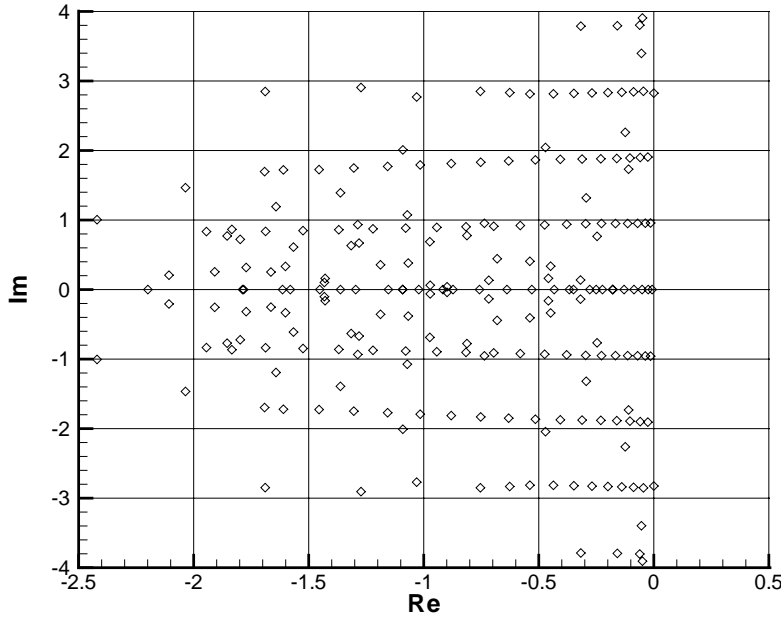


Figure 4.2: Reciprocal Ritz values computed on mesh M3 at $Re = 8069.76$ with Krylov space dimension $m = 250$.

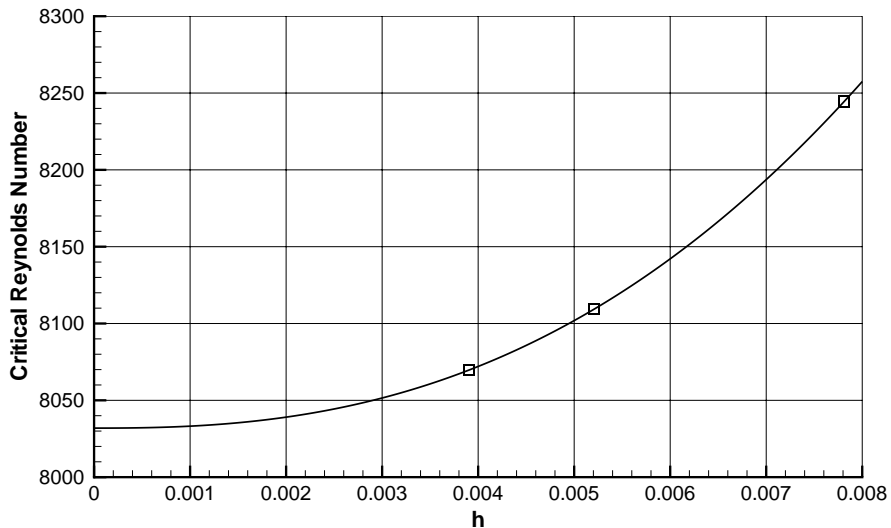


Figure 4.3: Critical Reynolds number $Re_{crit}(h)$ plotted as a function of the average finite volume cell size h . The equation for the continuous curve drawn through the three data points is given by (4.1).

Table 4.1: The first 10 reciprocal Ritz values computed on mesh M3 at $Re = 8069.76$.

n	σ_R	σ_I
1	-1.9025×10^{-7}	± 2.8251
2	-7.3257×10^{-3}	0.0000
3	-1.4161×10^{-2}	± 0.9576
4	-2.4387×10^{-2}	0.0000
5	-2.5916×10^{-2}	± 1.9062
6	-3.7116×10^{-2}	± 0.9551
7	-4.5205×10^{-2}	± 2.8520
8	-4.9557×10^{-2}	± 3.9063
9	-5.0851×10^{-2}	0.0000
10	-5.3889×10^{-2}	± 3.3969

Table 4.2: Computed critical Reynolds numbers $Re_{crit}(h)$ for meshes M1 to M3. The final value of $Re_{crit}(h)$ is the extrapolated value Re_{crit} .

Mesh	$Re_{crit}(h)$	m	σ_R	σ_I
M1	8244.55	250	-5.9487×10^{-8}	± 2.8315
M2	8109.38	250	-1.7769×10^{-7}	± 2.8256
M3	8069.76	250	-1.9025×10^{-7}	± 2.8251
Extrap	8031.92	-	-	-

Table 4.3: 10 leading reciprocal Ritz values computed at $Re = 8244.55$ on mesh M1 with Krylov subspace dimensions $m = 250$ and $m = 500$.

$m = 250$		$m = 500$	
σ_R	σ_I	σ_R	σ_I
-5.9487×10^{-8}	± 2.8315	-4.7800×10^{-8}	± 2.8315
-7.0198×10^{-3}	0.0000	-7.0198×10^{-3}	0.0000
-1.4154×10^{-2}	± 0.9643	-1.4154×10^{-2}	± 0.9643
-2.3571×10^{-2}	0.0000	-2.3571×10^{-2}	0.0000
-2.4539×10^{-2}	± 1.9159	-2.4539×10^{-2}	± 1.9160
-3.6512×10^{-2}	± 0.9593	-3.6512×10^{-2}	± 0.9593
-4.0236×10^{-2}	± 2.8600	-4.0234×10^{-2}	± 2.8600
-4.4007×10^{-2}	± 3.8954	-4.4746×10^{-2}	± 3.8951
-4.8049×10^{-2}	± 3.3908	-4.8055×10^{-2}	± 3.3908
-4.9438×10^{-2}	0.0000	-4.9438×10^{-2}	0.0000

Now

$$\frac{Re_{crit} - Re_{crit}(h)}{Re_{crit} - Re_{crit}(h/2)} = \frac{ch^p}{c \left(\frac{1}{2}\right)^p h^p} = 2^p. \quad (4.3)$$

Therefore, rearranging, we get

$$Re_{crit} = \frac{1}{2^p - 1} [2^p Re_{crit}(h/2) - Re_{crit}(h)], \quad (4.4)$$

and with p as calculated above we get $Re_{crit} \approx 8031.93$. In Fig. 4.3 we present a graph of both the interpolatory function given in Eqn. (4.1) and the data points corresponding to the critical values of the Reynolds number computed with the three meshes M1-M3. The extrapolated result agrees well with the prediction of Fortin et al. [50] ($Re_{crit} \approx 8000$), and represents only a 3.46% difference from the value of Re_{crit} calculated by Poliashenko and Aidun [115] ($Re_{crit} = 7763$) and a 2.72% difference from the Re_{crit} value of Cazemier et al. [26] ($Re_{crit} = 7819$). Most probably, the introduction of small leaks in the upper corners of the cavity in the present numerical method smooths out the solution and leads to the flow becoming unstable at a slightly larger critical Reynolds number.

4.3 Conclusions

In this chapter we have presented application of a novel implicit finite volume method to the linear stability analysis of a lid-driven cavity flow. The method is combined with the Arnoldi method for the determination of the linear stability properties. We have obtained a first critical Reynolds number in very good agreement with the few others published to date. We observed that its value is highly sensitive to the accuracy of the method and to the treatment of the singularities. Although eigenvalue calculations are computationally very expensive, the block banded matrix structure of the coefficient matrix in the GEVP and the use of the Arnoldi method allows us to compute the first 250 eigenvalues using the finest mesh.

Chapter 5

Flow Around a Confined Circular Cylinder in a Channel

5.1 Introduction

It is no exaggeration to say that an enormous (and still rapidly growing) corpus of literature on the subject of bluff body wakes has developed since the pioneering work of von Kármán early last century. This fact is an attestation to both the difficulty in understanding and adequately describing the flow bifurcations that occur at various values of the Reynolds number in viscous flows and the interest in doing so. Flows having particularly simple setups such as those past a sphere or cylinder have succeeded in drawing experimentalists, theoreticians and computational fluid dynamicists into the fray that has gone on through the decades and only very recently are consensuses emerging. In the paragraphs that follow we attempt to elucidate some of these for viscous flow past a cylinder. The reader is referred, additionally, to the review paper of Williamson [153] where further detail on this topic may be found.

It is now well established that for sufficiently low Reynolds numbers uniform flow past an infinitely long cylinder whose axis lies in the direction transverse to the flow is two dimensional and laminar everywhere and that in the wake of the cylinder two symmetric vortices are visible. For low Reynolds numbers (less than about 35 [55]) the length of the region containing the vortices increases with Reynolds number. As the flow rate increases further, the vortex pair loses its symmetry and oscillations begin to be observable in the wake (trail and vortices). Tiny irregular “gathers” begin to move down the outer boundary of the vortex pair, away from the cylinder [55, 140]. It is not until a slightly higher Reynolds number (approximately 46, see discussion below) is reached, however, that the gathers on the twin vortex boundaries begin to be shed alternately and give rise to the well-known vortex street.

Various different criteria have been used by experimentalists to determine the Reynolds number at which the wake loses stability. Coutanceau and Bouard [34], for example, considered the birth of the first instability to occur when a difference in the distance of the cores of these two recirculatory regions from the cylinder’s rear stagnation point could be detected. For the unbounded cylinder this happened at a Reynolds number of 34. Fortuitously, Gerrard [55] established that it was at this same Reynolds number that the bubble boundary containing the standing eddies began to exhibit gathers. By this stage the length of the bubble was approximately two cylinder diameters. In the experiments of Taneda [140] the appearance of gathers on the boundary of the twin vortices did not occur until the Reynolds number

exceeded 35, although oscillations in the wake trail could be seen as early as $Re = 30$. The onset of periodic two-dimensional vortex shedding in the wake of the cylinder is now known to be a supercritical Hopf bifurcation which may be modelled using the Landau equation ([119, 108, 42]). What is less clear, however, is the value of the critical Reynolds number Re_{crit1} at which this vortex shedding first occurs. Experimentalists have variously estimated Re_{crit1} to be around 40 [106, 143], 45 [140], 47 [119] or 48 [107]. Undoubtedly, factors influencing the spread of values reported for Re_{crit1} and associated Strouhal numbers St include the severe difficulty entailed in detecting the onset of oscillations in the wake, cylinder roughness, the need to eliminate background fluid motion and temperature variation, as well as the pernicious influence of three-dimensional, wall and end effects. Much better agreement exists on $St - Re$ data for established laminar parallel shedding amongst various experimental research groups, however (see Fig. 7(b) of [153]). Numerical simulations using finite element methods of the transition from steady to periodic flow have been performed by Jackson [72] and Ding and Kawahara [39], for example. Jackson identified the transition as a Hopf bifurcation and solved an extended system of equations to pinpoint the critical parameters as $Re_{crit1} = 46.184$ and $St = 0.13804$. Use of an Arnoldi method permitted Ding and Kawahara to estimate the critical values of the primary instability as $Re_{crit1} = 46.389 \pm 0.010$ and $St = 0.12619$. Thus, reasonable agreement was obtained with the results of Jackson. The low-dimensional Galerkin projection method of Noack and Eckelmann [108] led to a prediction of $Re_{crit1} = 50$ and $St = 0.132$. The authors attributed the inaccuracy in this case to an insufficient number of expansion modes.

The transition to three-dimensional vortex shedding was first measured by Roshko [120] and has been described by Williamson [150] as happening in two distinct stages. These manifest themselves in discontinuities (but see comments later in the Introduction) in the $St - Re$ curve at Reynolds numbers of the order 180 – 190 and 230 – 250, and are associated, respectively, with the appearance of large-scale structures (mode A) and fine-scale structures (mode B) in the span-wise direction. The first discontinuity has been found experimentally to be hysteretic. Numerical simulations may show a rather different picture, however. Karniadakis and Triantafyllou [78] used both three-dimensional spectral element and spectral element/Fourier discretizations to investigate three-dimensional dynamics of flow past a cylinder at Reynolds numbers up to 500. Span-wise lengths equal to $\pi/2$ and π cylinder diameters were considered and 34 spectral elements used. A secondary instability of the two-dimensional vortex street leading to a soft transition to periodic three-dimensional shedding was seen to appear at a Reynolds number between 200 and 210 on the domain having the greater span-wise depth. Unlike the experimental findings of Williamson [150] no hysteresis phenomenon could be observed. It should be added at this point, however, that Karniadakis and Triantafyllou were principally concerned with the description of the route to chaos in the wake of a circular cylinder, something that they identified as happening through a sequence of period-doubling bifurcations. In a later paper Thompson et al. [142] also used a spectral element/Fourier series discretization but with 60 spectral elements and a span-wise depth between π and 2π cylinder diameters. The paper is important in that modes A and B were captured computationally for the first time. Mode A shedding was found to be periodic and the onset Reynolds number was computed to be slightly less than 200. However, neither the hysteretic behavior at the first of the secondary instabilities, nor the abrupt change in the associated shedding frequency could be seen. The three-dimensional simulations cited above and others like them have all indicated a soft transition to three-dimensional periodic flow. The first numerical reproduction of Williamson's experimental finding of a hard hysteretic onset of three dimensionality was

published by Zhang et al. [158] who used a finite difference method and a span-wise domain equal to 24 cylinder diameters. It was found that the crucial missing ingredient in previous simulations was a “vortex adhesion mode” of the secondary instability. The mode was induced by Zhang et al. by injecting a strongly localized span-wise inhomogeneity into the initial conditions. For span-wise lengths sufficiently large (an order of magnitude greater than in previous simulations) this instability mode was found to be self-sustaining, at least for the range of Reynolds numbers corresponding to the onset of mode A and mode B instabilities. The hard hysteretic transition to three dimensionality could be clearly seen in a discontinuity in the $St - Re$ curve at the onset of mode A instabilities. Previous computations took span-wise domain lengths too short for the vortex adhesion modes to be sustainable.

The linear stability of the two-dimensional periodic wake to three-dimensional perturbations has been investigated using Floquet stability theory by several authors. Noack and Eckelmann [108] predicted an absolute three-dimensional secondary instability in the span-wise direction of the von Kármán vortices at a critical Reynolds number of $Re_{crit2} = 170$ and a span-wise wavenumber k_z of 1.75 cylinder diameters. The results were in qualitative but not quantitative agreement with those of Barkley and Henderson [10] who used a highly accurate spectral element method with up to 362 elements and $O(10^4)$ spatial degrees of freedom. The critical parameters for the onset of the mode A instability were given by these authors as $Re_{crit2} = 188.5 \pm 1$ and $k_z = 3.96$ cylinder diameters, and were in close accord with the experimental values of Williamson [152]. Correctly capturing mode B, however, involved non-linear interactions outside the scope of the authors’ linear approximations. Ding and Kawahara [40] claimed that their finite element/Arnoldi method for determining the dominant Floquet multipliers was more accurate than the spectral element method of Barkley and Henderson, and the authors succeeded in verifying the existence of both modes. The computed critical parameters were very similar to those of Barkley and Henderson. Despite the encouraging agreement that exists between the predictions by a Floquet analysis of the critical secondary instability parameters and those found experimentally (see, for example, [152]), it should be noted, as do Barkley and Henderson [10], that at the secondary instability the leading Floquet multiplier is real and positive so that no new shedding frequency is anticipated. The change of shedding frequency at the onset of mode A is a non-linear phenomenon, possibly explainable in terms of the vortex-adhesion modes mentioned above [158].

In the above paragraphs we have only briefly touched upon some of the span-wise length effects in three-dimensional computational domains and the topic is treated in greater detail elsewhere [86, 142, 158]. Discussion on experimentally observed end effects such as oblique vortex shedding modes and discontinuities in the $St - Re$ relationship may be found in several papers by Williamson (see, for example, [151, 153]). We shall say no more on this matter since our interest in this chapter is rather a careful analysis of *lateral* wall effects on viscous flow past a confined cylinder. What we have in mind is depicted in Fig. 5.1. In this figure an infinitely long cylinder of diameter D is placed symmetrically between parallel lateral walls a distance H apart. The parameter $\Lambda \equiv D/H$ is usually termed the blockage ratio. In stark contrast to the wealth of insight and commentary available on vortex dynamics in the wake of an unbounded cylinder we find ourselves with only a handful of papers offering a serious treatment of the blockage ratio effects present in the confined cylinder problem. This paucity of scientific literature should not be interpreted as implying that the problem is an unimportant one, however. On the contrary, even for unbounded flow past a cylinder the (infinite) flow domain has to be replaced with (or mapped onto) a finite one, thus introducing numerical or

experimental blockage effects that may have considerable influence over the determined values of the flow parameters [5, 34]. Many of the blockage ratio effects described in the literature are more or less evident:

1. In the steady flow regime, bringing the walls closer to the cylinder results in the appearance of the twin vortices in the cylinder wake at higher Reynolds numbers.
2. At any given modest ($\lesssim 50$) Reynolds number and for $\Lambda \leq 0.2$ the length of the closed vortex bubble decreases with wall proximity, whilst remaining a linear function of Re [5, 29, 34].
3. For increasing blockage ratios Λ up to 0.5 the steady two-dimensional base flow is stabilized with respect to infinitesimal perturbations due to constraint by the confining walls of the separating shear layer that exists between the cylinder wake and the wall boundary layer vorticity [29, 34].
4. Once the critical Reynolds number for the primary instability has been exceeded the frequency with which periodic two-dimensional vortex shedding takes place at a given Reynolds number is an increasing function of Λ [5, 15, 29, 137]¹.
5. At $Re = O(100)$ both the mean drag coefficient C_d and the separation angle of the vortex bubble increase as the walls approach the cylinder [5, 15, 34, 137].

A problem bearing some similarities to that of flow past a confined cylinder is that of flow around a cylinder placed at various heights above a plane boundary. A recent literature survey of experimental investigations into this problem may be found in the paper of Lei et al. [85]. These studies have sought to address the issue of how forces on the cylinder and vortex shedding frequency depend on the ratio G/D of the gap between the cylinder and the wall, G , and the cylinder diameter, D . They have also been concerned with understanding the effect on these quantities of the boundary layer thickness and the velocity gradient. Most of the experiments have been conducted at Reynolds numbers in the sub-critical regime ($Re = O(1 \times 10^4)$) in which the boundary layer is still laminar. Lei et al. [85] found that the drag coefficient C_d increased with increasing gap ratio because of the reduction in the base pressure. The same trend in base pressure dependence had been observed by Bearman and Zdravkovich [14]. The latter authors further found that the Strouhal number for $G/D \gtrsim 0.3$ was more or less constant in their experiments at a Reynolds number of 4.8×10^4 . Lei et al. [85] also noted only slight fluctuations in a Strouhal number computed from the free-stream velocity for a similar range of gap to diameter ratios. However, for gaps less than 0.3 cylinder diameters [14] or 0.2 – 0.3 diameters (depending on the boundary layer thickness, [85]) vortex shedding was suppressed. Differences in the quantification of the vortex shedding suppression gap ratio were due possibly to differences in the boundary layer thicknesses generated by the experimentalists and also to the manner in which the critical gap ratio was identified: Bearman and Zdravkovich [14] using a spectral analysis of hot-wire signals in the cylinder wake whereas the method of Lei et al. [85] was based on observation of the spectrum of the lift coefficient. Suppression of vortices for a sufficiently small gap ratio was also confirmed by Zovatto and Pedrizzetti [160], who used a finite element method based on a vorticity-streamfunction formulation to analyze flow around

¹The spurious result obtained by Stansby and Slaouti [137] for $\Lambda = 0.5$ is thought to be due to neglect of the boundary layers in their numerical simulation using random vortex methods.

a cylinder positioned eccentrically between two lateral walls. For very small gap ratios Zovatto and Pedrizzetti [160] found a recirculating bubble on the wall downstream of the cylinder. A separation bubble on the wall had also been seen earlier by Bearman and Zdravkovich [14] for gap ratios smaller than the critical value for vortex suppression. We will return to some of these flow phenomena in our discussion of our numerical results for large blockage ratios.

The motivation for the present study is two-fold. First, the rich fluid dynamics in the wake and near the lateral walls deserves to be investigated with greater numerical accuracy than has been possible with the computational resources available to other researchers at the time at which they prepared their manuscripts. Computations on meshes allowing for only tens of thousands of degrees of freedom have been typical (for example, [29, 72]). In the present study a novel finite volume method [123, 124, 125] is used in a parallel implementation, permitting up to 1.8 million degrees of freedom and thus a higher resolution of the wake and boundary layer structures. Secondly, the only previous numerical linear stability analysis of flow past a confined cylinder available to us [29] went no further than a blockage ratio of $\Lambda = 0.7$. From the results of this publication the trend seemed to be one of decreasing linear stability of the two-dimensional flow for $\Lambda > 0.5$. Stability was always lost over the range of blockage ratios considered through a symmetry-breaking supercritical Hopf bifurcation. We wish in this chapter to investigate the effect on the critical Reynolds number of choosing $\Lambda > 0.7$ and to identify the nature of the flow instabilities by means of an Arnoldi method.

The outline of the present chapter is as follows: In Section 5.2 we describe the problem to be solved. In Section 5.3 is dedicated to validation of our numerical scheme for the classical problem of unbounded two-dimensional flow past a circular cylinder. Extensive comparison with other results in the literature is made. In particular we find excellent agreement with previously obtained values for the drag coefficients, first critical Reynolds numbers Re_{crit1} and the corresponding critical Strouhal numbers. In Section 5.4 we are concerned with a detailed description of wake dynamics and interactions of the wake and wall boundary layers for blockage ratios up to 0.9. For blockage ratios below approximately 0.85 the locus of a supercritical Hopf bifurcation may be traced out in parameter space. At higher Reynolds numbers and for blockage ratios sufficiently large there is a pitchfork bifurcation of the steady symmetric state to one of two asymmetric steady states. Either side of the curve of neutral stability for the pitchfork bifurcation the steady solutions are linearly stable but appear on the basis of direct numerical simulations to be unstable to finite two-dimensional perturbations. Finally, for yet larger Reynolds numbers and $\Lambda \gtrsim 0.82$ a Hopf bifurcation of the asymmetric state occurs. The oscillations are now quite different from those associated with the first symmetry-breaking instability, the amplitude of the drag and lift coefficients being much stronger and the oscillations are now asymmetric in time. Finally, we draw some conclusions.

5.2 Mathematical Problem

An infinitely long cylinder of diameter D is placed midway between two parallel planes which are a distance H apart, as shown in Fig. 5.1. Let us denote by U_{max} the maximum inlet fluid speed. In the present chapter the Reynolds number is defined as $Re = U_{max}D/\nu$ where ν is the kinematic viscosity. In the presentation of results in Section 5.3 and Section 5.4 for those flows exhibiting periodic vortex shedding, a Strouhal number St is defined by $St = D/(TU_{max})$, where T is the period of vortex shedding. We denote by $(\mathbf{x}, t) = ((x_1, x_2), t)$ a generic point in

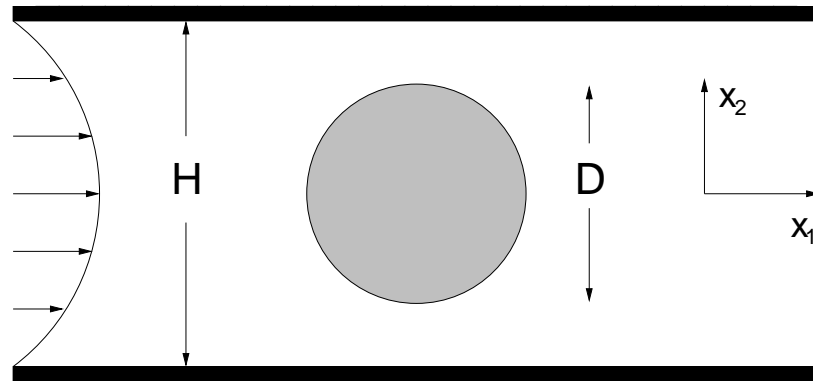


Figure 5.1: Schematic of a cylinder placed symmetrically in a plane channel. The cylinder diameter is D and the channel height H .

space and time.

In Section 5.3 we approximate the unbounded cylinder geometry by choosing $\Lambda = 0.01$ and the following boundary conditions:

$$\text{Cylinder surface : } \mathbf{u} = (0, 0), \quad (5.1)$$

$$\text{Lateral walls : } \mathbf{u} = (1, 0), \quad (5.2)$$

$$\text{Inflow : } \mathbf{u} = (1, 0), \quad (5.3)$$

$$\text{Outflow : } \frac{\partial^2 u_1}{\partial x_1^2} = 0, \quad \frac{\partial u_2}{\partial x_1} = 0. \quad (5.4)$$

For the confined cylinder problem (see Section 5.4) equations (1.3)-(1.8) are solved subject to the following boundary conditions on the components of velocity:

$$\text{Cylinder surface : } \mathbf{u} = (0, 0), \quad (5.5)$$

$$\text{Lateral walls : } \mathbf{u} = (0, 0), \quad (5.6)$$

$$\text{Inflow : } \mathbf{u} = (1 - x_2^2, 0), \quad (5.7)$$

$$\text{Outflow : } \frac{\partial^2 u_1}{\partial x_1^2} = 0, \quad \frac{\partial u_2}{\partial x_1} = 0. \quad (5.8)$$

Some care needs to be taken with how the second normal derivative outflow condition is imposed, due to possible linear dependence in the discrete equation set of this condition with the discrete form of the continuity equation. More precisely stated, the second normal derivative outflow condition will be automatically satisfied at $x_2 = 0$ upon imposition of the continuity equation (1.3) within each finite volume. For all the results presented in Section 5.3 the dimensionless upstream and downstream channel lengths were set equal to $400D$. In Section 5.4 these lengths were chosen to both be equal to $40D$. The choice of outflow boundary conditions (5.4) and (5.8) was motivated by the fact that our numerical method uses a velocity-only formulation so that the usual traction-free conditions could not easily be implemented. The free boundary layer type of conditions (5.4) and (5.8) were used successfully by Kourta et al. [83] in finite volume simulations of a two-dimensional plane mixing layer. Although Jin and Braza [76] later developed a non-reflecting outlet condition that greatly reduced feedback noise

Λ	M1				M2				M3			
	i_{max}	k_{max}	k_{wall}	N	i_{max}	k_{max}	k_{wall}	N	i_{max}	k_{max}	k_{wall}	N
0.01	181	301	137	89,336	361	601	273	355,312	721	1201	545	1,417,184
0.1	181	441	77	116,536	361	881	153	462,512	721	1761	305	1,842,784
0.2	181	421	57	109,336	361	841	113	433,712	721	1681	225	1,727,584
0.3	181	411	47	105,736	361	821	93	419,312	721	1641	185	1,669,984
0.5	181	401	37	102,136	361	801	73	404,912	721	1601	145	1,612,384
0.7	181	391	27	98,536	361	781	53	390,512	721	1561	105	1,554,784
0.9	181	381	17	94,936	361	761	33	376,112	721	1521	65	1,497,184

Table 5.1: Values of grid parameters i_{max} , k_{max} , k_{wall} and N .

when compared with the outlet condition of Kourta et al. [83], the outlet length used for the calculations in the present work are considered sufficiently great that the difference between the influence of the one set of exit conditions and the other on drag, linear stability and Strouhal number would be negligible. The more complicated exit conditions of Jin and Braza [76] are therefore not implemented.

In our numerical scheme the continuity equation (1.3) is satisfied within each finite volume whilst (1.8) is applied to each finite volume except the finite volumes next to the wall. Therefore, vorticity creation is allowed within these finite volumes in order to satisfy the no-slip boundary conditions. Equations (1.3) and (1.8) with no-slip boundary conditions are enough to solve the problem in a simply-connected domain (such as that found in the lid-driven cavity problem, for example [124]). However, if the domain is not simply-connected there is a need for additional equations. This is because there is a potential problem in our velocity-only formulation with multi-valuedness of the pressure field, even though the pressure does not appear explicitly as a dependent variable in our formulation. To rectify this a Kutta-like condition

$$\oint_{\Gamma} \mathbf{n} \times \left[\frac{\partial \mathbf{u}}{\partial t} + (\nabla \times \mathbf{u}) \times \mathbf{u} + \frac{1}{Re} \nabla \times (\nabla \times \mathbf{u}) \right] ds = \mathbf{0}, \quad (5.9)$$

is imposed around the closed path Γ formed from the union of the outer edges of the finite volumes on the cylinder surface. The condition (5.9) guarantees that

$$\oint_{\Gamma} \mathbf{n} \times \nabla p ds = \mathbf{k}[p] = \mathbf{0}, \quad (5.10)$$

where \mathbf{k} is a unit vector normal to the plane of the flow, and $[p]$ denotes the jump in the pressure on passing once around Γ . Since (1.8) is satisfied in every interior finite volume, satisfaction of (5.9) ensures that p is single-valued at every interior finite volume vertex. The pressure can be obtained by integrating the two components of the pressure gradient appearing in the equations of linear momentum in a manner analogous to that used in finding a streamfunction from a given velocity. The values of p on the domain boundaries, when required, are determined by first computing $\partial p / \partial n$ from (1.2).

Three different finite volume grids (M1-M3) have been used for each value of the blockage ratio considered in this chapter. Each of the meshes has been generated algebraically and then smoothed by solving elliptic partial differential equations for the spatial variables x_1 and x_2 where derivatives are with respect to mapped variables in a space in which the mesh appears rectangular [138]. For the present problem the physical grid is ‘‘cut’’ along the line $x_2 = 0$

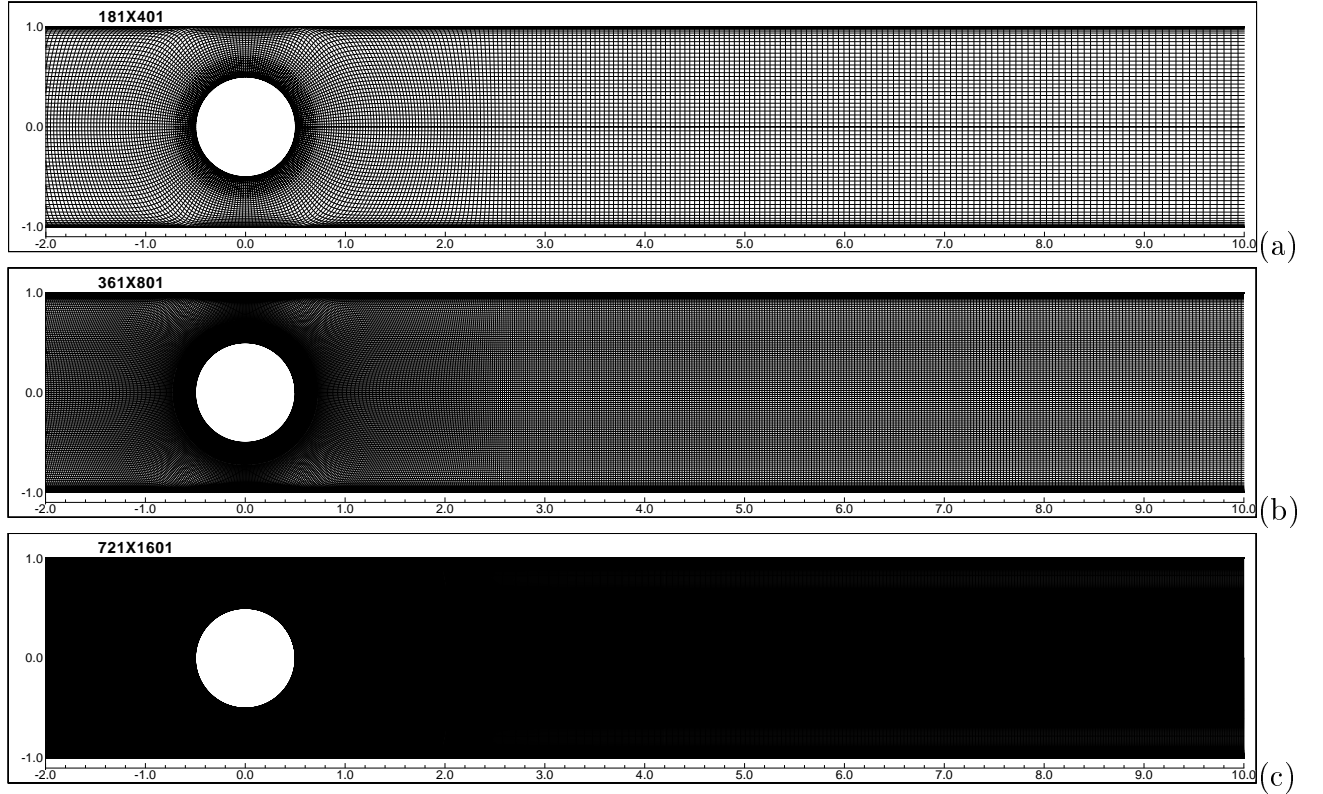


Figure 5.2: Computational meshes used for blockage ratio $\Lambda = 0.5$. (a) Mesh M1: Number of degrees of freedom = 102,136. (b) Mesh M2: Number of degrees of freedom = 404,912. (c) Mesh M3: Number of degrees of freedom = 1,612,384.

from the rear stagnation point to the outlet before being mapped. The method of Steger and Sorenson [138] allows both grid cell sizes and grid cell skewness to be controlled at the inner and outer boundaries. In order to control these parameters the authors solved the following governing equations:

$$\xi_{xx} + \xi_{yy} = P_1(\xi) \exp(-a(\eta - \eta_1)), \quad (5.11)$$

$$\eta_{xx} + \eta_{yy} = Q_1(\xi) \exp(-b(\eta - \eta_1)), \quad (5.12)$$

where (ξ, η) represents a point in the computational domain, (x_1, x_2) is denoted by (x, y) and P_1 and Q_1 are forcing terms defined at $\eta = \eta_1$ where the grid points are to be clustered. These equations can be transformed to the computational domain as

$$\alpha x_{\xi\xi} - 2\beta x_{\xi\eta} + \gamma x_{\eta\eta} = -J^2(P_1 \exp(-a(\eta - \eta_1))x_\xi + Q_1 \exp(-b(\eta - \eta_1))x_\eta), \quad (5.13)$$

$$\alpha y_{\xi\xi} - 2\beta y_{\xi\eta} + \gamma y_{\eta\eta} = -J^2(P_1 \exp(-a(\eta - \eta_1))y_\xi + Q_1 \exp(-b(\eta - \eta_1))y_\eta), \quad (5.14)$$

where J is the Jacobian $J = x_\xi y_\eta - x_\eta y_\xi$ of the transformation and

$$\alpha = x_\eta^2 + y_\eta^2, \quad (5.15)$$

$$\beta = x_\xi x_\eta + y_\xi y_\eta, \quad (5.16)$$

$$\gamma = x_\xi^2 + y_\xi^2. \quad (5.17)$$

To find the forcing terms P_1 and Q_1 Eqns. (5.13) and (5.14) are applied at $\eta = \eta_1$

$$\alpha x_{\xi\xi} - 2\beta x_{\xi\eta} + \gamma x_{\eta\eta}|_{\eta=\eta_1} = R_1 = -J^2(P_1 x_\xi + Q_1 x_\eta), \quad (5.18)$$

$$\alpha y_{\xi\xi} - 2\beta y_{\xi\eta} + \gamma y_{\eta\eta}|_{\eta=\eta_1} = R_2 = -J^2(P_1 y_\xi + Q_1 y_\eta), \quad (5.19)$$

and P_1 and Q_1 can be calculated as

$$P_1 = J^{-1}(y_\eta R_1 - x_\eta R_2)|_{\eta=\eta_1}, \quad (5.20)$$

$$Q_1 = J^{-1}(-y_\xi R_1 + x_\xi R_2)|_{\eta=\eta_1}. \quad (5.21)$$

To control the normal grid space the authors imposed the following condition

$$ds = \sqrt{dx^2 + dy^2} = \sqrt{[(x_\eta)^2 + (y_\eta)^2]}d\eta|_{\xi=const.}, \quad (5.22)$$

In order to ensure the orthogonality on the boundary Steger and Sorenson required that

$$\nabla\xi \cdot \nabla\eta = 0 = x_\xi x_\eta + y_\xi y_\eta. \quad (5.23)$$

Therefore, using Eqns. (5.22) and (5.23) we can compute x_η and y_η as

$$x_\eta = -y_\xi / \sqrt{[(x_\xi)^2 + (y_\xi)^2]} \frac{ds}{d\eta}, \quad (5.24)$$

$$y_\eta = x_\xi / \sqrt{[(x_\xi)^2 + (y_\xi)^2]} \frac{ds}{d\eta}. \quad (5.25)$$

where $ds/d\eta$ corresponds to the normal grid space. Smoothed out meshes M1-M3 are presented in Fig. 6.1 and they are characterized by i_{max} : the number of nodes on the surface of the cylinder, k_{max} : the number of nodes along the line $x_2 = 0$ from the rear stagnation point on the cylinder to the outflow boundary and k_{wall} : the number of nodes in the gap between the cylinder and a lateral wall. The values of i_{max} , k_{max} , k_{wall} and N (the number of degrees of freedom) for the three meshes are supplied in Table 5.1 for different blockage ratios.

5.3 Flow Past an Unbounded Circular Cylinder

Flow around an unbounded circular cylinder is a classical benchmark problem for which a large number of numerical and experimental results exists. In this problem, and in approximation to the case of an unbounded flow domain, a circular cylinder of diameter $D = 1.0$ is placed symmetrically in a channel with blockage ratio $\Lambda = 0.01$. For the numerical linear stability analysis the three meshes M1 to M3 were used, with i_{max} , k_{max} and k_{wall} as given in Table 5.1. However, for unsteady time-dependent simulations we were only able to afford to use M1 and M2, the unsteady calculations on M3 proving to be prohibitively expensive. On the boundaries of the computational domain the conditions (5.1)-(5.4) were imposed.

The linear stability analysis predictions of the critical Reynolds and Strouhal numbers corresponding to the onset of the first flow instability are supplied in Table 5.2, as computed on meshes M1 to M3. Also shown are the values of these quantities when extrapolated to zero mesh size. The extrapolated critical Reynolds number is found to be $Re_{crit1} = 46.74$

with a corresponding Strouhal number of $St_{crit1} = 0.1167$. These values are compared with others in the literature in the same table. Although we find good agreement for the critical Reynolds number with the result of Ding and Kawahara [39] ($Re_{crit1} = 46.389$), and Jackson [72] ($Re_{crit1} = 46.184$), the critical Strouhal number manifests wider scatter in the cited references. Issues such as the blockage ratios chosen, distances from the cylinder of the upstream and downstream boundaries, boundary conditions, mesh resolution and number of eigenvalues determined may be amongst the reasons for discrepancies in the numerical results. In addition to our mesh convergence study, we present a convergence study of the leading eigenvalues on mesh M1 with the Krylov subspace dimension m and shift parameter λ in Table 5.3 in order to show that our leading eigenvalue is essentially independent of both m and λ for sufficiently large values of these two parameters. Although the leading eigenvalue converges very rapidly with a suitably chosen complex shift around the leading eigenvalue, it requires complex arithmetic. A real shift also dramatically improves the convergence of the leading eigenvalue whilst avoiding complex arithmetic which significantly increases the memory requirements during LU factorization. Our calculations show that a Krylov subspace dimension as low as 250 can be enough to compute the leading eigenvalue with $\lambda = 0.50 \pm 0.00i$ whilst with no shift a Krylov subspace dimension larger than 1000 may be required.

The computed eigenspectrum on mesh M3 at the critical Reynolds number is given in Fig. 5.3. Although we present the first 250 computed eigenvalues, calculations with higher Krylov subspace dimensions showed that only the leading eigenvalues and the eigenvalues around the origin were properly converged. As may be seen, the most dangerous eigenvalue pair is well separated from the rest of the spectrum, unlike the eigenspectrum for the two-dimensional lid-driven cavity problem (see, for example, Fig. 4.2 of Chapter 4). This is likely to be the reason for well-developed periodic flow observed far beyond the critical Reynolds number. Our critical Strouhal number (0.1167) compares very well with the Strouhal number $St = 0.1179$ computed at the same Reynolds number (46.74) from a curve fit of the two-dimensional experimental data of Williamson [151]. In addition, our critical Strouhal number agrees quite well with the Strouhal number ($St = 0.11834$) of the direct numerical simulation of Posdziech and Grundmann [116], even though their critical Strouhal number and ours were computed at two slightly different Reynolds numbers ($Re = 47.50$ and $Re = 46.74$, respectively).

In Fig. 5.4 we present comparisons of the Strouhal number versus Reynolds number and in Fig. 5.5 comparisons of the drag coefficient $C_d = F_x/0.5U_{max}^2D$ versus Reynolds number, in further verification of our numerical scheme. The computed values are supplied in Table 5.4. Our Strouhal numbers were found to be in very good agreement with those from the experimental work of Williamson [151] for Reynolds numbers up to 200. Beyond this point the flow becomes three-dimensional and we do not expect to have agreement with the experimental results. Good agreement was also observed with the two-dimensional numerical simulations of Henderson [68] and Posdziech and Grundmann [116]. Although both Henderson [68] and Posdziech and Grundmann [116] used high-order spectral elements the differences between these two sets of results are due to the use of different blockage ratios in their calculations. However, as the Reynolds number increases the difference in their computed results becomes smaller. An interesting convergence study on the extension of the computational domain boundary is given by Posdziech and Grundmann [116] at $Re = 200.00$. The authors concluded that the lateral boundaries should be set at a distance of at least 70 diameters away in order to obtain a Strouhal number independent of yet smaller blockage ratios. At lower Reynolds number the effect of the lateral boundaries becomes more severe (see, for example [49]). In

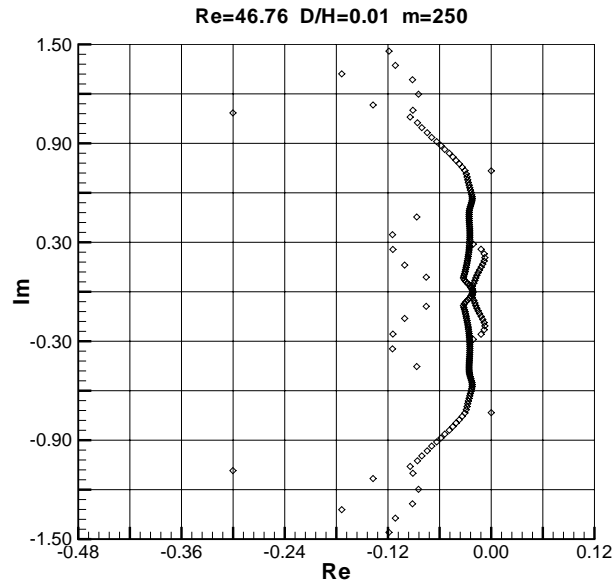


Figure 5.3: Reciprocal Ritz values for unbounded flow around a circular cylinder at $Re = 46.76$ computed on mesh M3 with Krylov space dimension $m = 250$ and shift parameter $\lambda = 0.50 \pm 0.00i$ ($\Lambda = 0.01$).

	M1	M2	M3	Extrapolated	Jackson	Ding & Kawahara	Noack & Eckelmann	Chen et al.
Re_{crit1}	47.08	46.82	46.76	46.74	46.184	46.389	50	47.9
St_{crit1}	0.1163	0.1166	0.1167	0.1167	0.13804	0.12619	0.132	0.138

Table 5.2: Unbounded flow past a cylinder. Comparison of critical Reynolds numbers computed on M1-M3 with others in the literature.

m	$\lambda = 0.00 \pm 0.00i$	$\lambda = 0.25 \pm 0.00i$	$\lambda = 0.50 \pm 0.00i$
250	$-2.499530 \times 10^{-3} \pm 0.716816$	$-2.362255 \times 10^{-6} \pm 0.730913$	$-2.666849 \times 10^{-6} \pm 0.730912$
500	$+3.029965 \times 10^{-3} \pm 0.726480$	$-2.668530 \times 10^{-6} \pm 0.730912$	$-2.668473 \times 10^{-6} \pm 0.730912$
1000	$+2.230634 \times 10^{-4} \pm 0.729683$	$-2.668474 \times 10^{-6} \pm 0.730912$	$-2.668473 \times 10^{-6} \pm 0.730912$

Table 5.3: Unbounded flow past a cylinder. Convergence of the leading eigenvalue at $Re=47.08$ on M1 with the Krylov space dimension m and shift parameter λ .

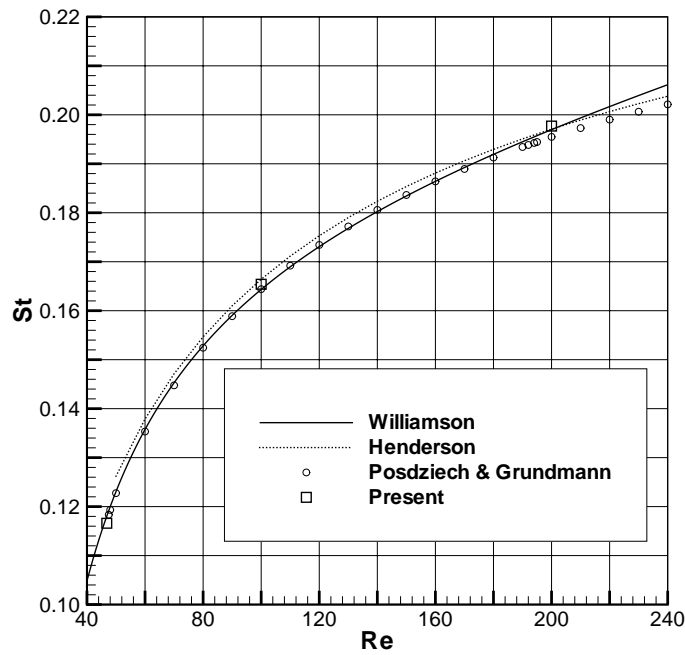


Figure 5.4: Comparison of Strouhal number versus Reynolds number for unbounded flow around a circular cylinder with other results in the literature: (—), experimental work of Williamson [151]; (\cdots), numerical results of Henderson [68]; (\circ), numerical results of Posdziech and Grundmann [116]; (\square), present ($\Lambda = 0.01$, mesh M2).

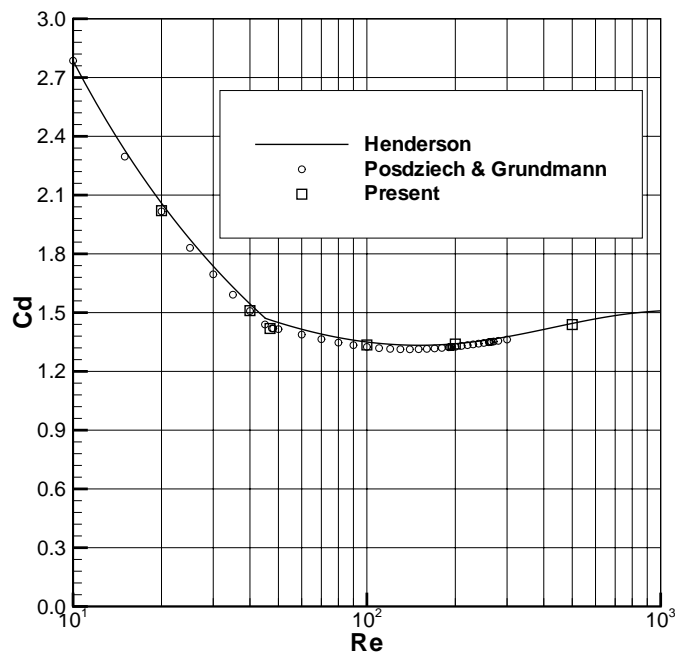


Figure 5.5: Comparison of drag coefficient versus Reynolds number for unbounded flow around a circular cylinder with other results in the literature: (—), numerical results of [68]; (\circ), numerical results of [116]; (\square), present ($\Lambda = 0.01$, mesh M2).

Literature	C_d	C_l	St
Re=20.00			
Dennis & Chang	2.045	-	-
Fornberg	2.0001	-	-
Ye et al.	2.03	-	-
Henderson	2.0587	-	-
Posdziech & Grundmann	2.01677	-	-
Present	2.0205	-	-
Re=40.00			
Dennis & Chang	1.522	-	-
Fornberg	1.4980	-	-
Ye et al.	1.52	-	-
Henderson	1.5445	-	-
Posdziech & Grundmann	1.50814	-	-
Present	1.5102	-	-
Re=100.00			
Henderson	1.35000	-	0.166427
Posdziech & Grundmann	1.32487 ± 0.008970	± 0.32104	0.16440
Williamson	-	-	0.1643
Present	1.3349 ± 0.0095	± 0.3333	0.1654
Re=200.00			
Henderson	1.34116	-	0.197072
Posdziech & Grundmann	1.32564 ± 0.043558	± 0.67315	0.19549
Williamson	-	-	0.1970
Present	1.3396 ± 0.0452	± 0.6861	0.1977
Re=500.00			
Henderson	1.4448	-	-
Present	1.4390 ± 0.2263	± 1.1748	0.2297

Table 5.4: Unbounded flow past a cylinder. Comparison with some results in the literature of lift coefficient C_l , drag coefficient C_d and Strouhal number St computed on M2 .

addition, Zisis and Mitsoulis [159] showed that the convergence of the total drag at $Re=0.00$ may be very poor as Λ goes to zero.

5.4 Flow Past a Confined Circular Cylinder ($0.1 < \Lambda < 0.9$)

Flow around a confined circular cylinder (as opposed to the unbounded case) is an attractive benchmark problem in numerical simulation since it does not suffer from any of the difficulties associated with far-field boundary conditions (particularly at very low Reynolds numbers) and permits the use of grid points more efficiently in smaller computational domains. Somewhat surprising, therefore, is that the only numerical linear stability analysis of Newtonian flow past a confined cylinder available in the literature would seem to be that of Chen et al. [29]. These authors went no further than identifying the curve of neutral stability for the supercritical Hopf bifurcation at blockage ratios up to $\Lambda = 0.7$. This is regrettable, because as we shall see in the paragraphs to follow, the linear stability properties of the flow become rich and therefore

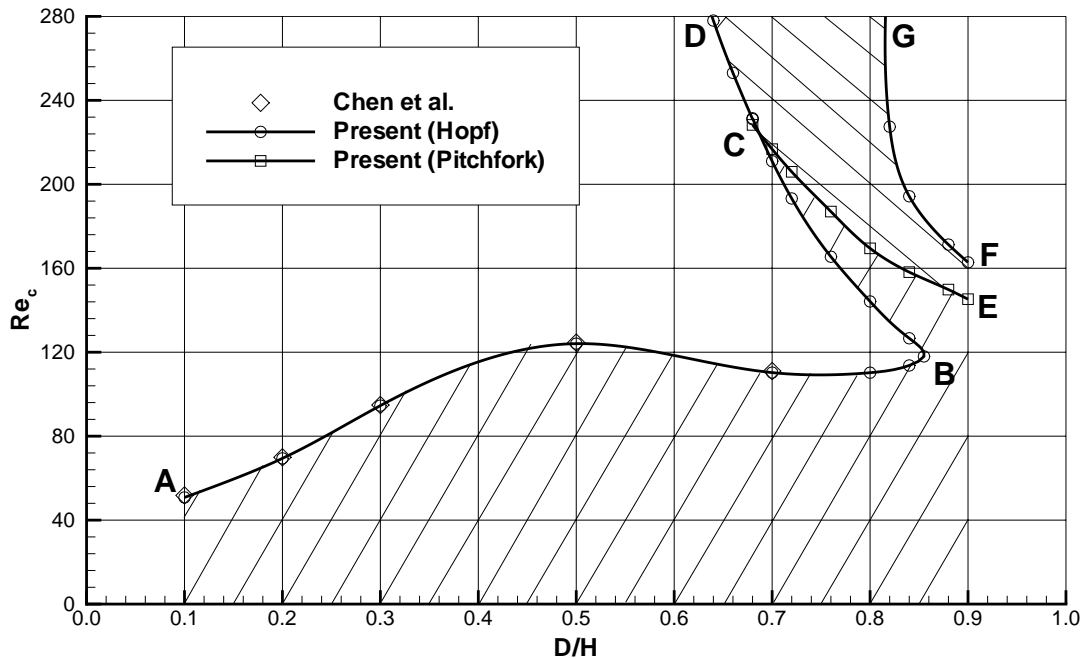


Figure 5.6: Change of critical Reynolds number corresponding to both Hopf and pitchfork bifurcations with blockage ratio Λ , computed on M2. AC : curve of neutral stability for Hopf bifurcations about symmetric solution; CD : transition curve from asymmetric vortex shedding (smaller Λ) to a steady asymmetric solution (larger Λ); CE : neutral stability curve for pitchfork bifurcation of steady symmetric solution (smaller Λ) to a steady asymmetric state (larger Λ); FG : Hopf bifurcation of an asymmetric solution (smaller Λ) to asymmetric vortex shedding (larger Λ). C is a co-dimension 2 point where Hopf and pitchfork bifurcations occur simultaneously.

interesting at higher blockage ratios and Reynolds numbers than those considered by Chen et al. In the present study we consider two-dimensional flow at Reynolds numbers up to 280 and for blockage ratios in the range 0.1 to 0.9.

5.4.1 Linear stability analysis

The curves of neutral stability computed from the GEVP with a Krylov subspace dimension $m = 250$ on mesh M2 for $\Lambda \in [0.1, 0.9]$ and $Re < 280$ are presented in Fig. 5.6. Our discussion of these curves will focus on the five distinct curve sections labelled AB , BC , CD , CE and FG in the same figure. The critical Reynolds numbers and corresponding Strouhal numbers (where appropriate) for points on each curve section and computed on meshes M1 to M3 are supplied in Table 5.5.

Curve section AB

Validation of our numerical stability analysis and direct numerical simulations for flow past an unbounded cylinder $\Lambda \approx 0$ has been described in Section 5.3. For the confined cylinder

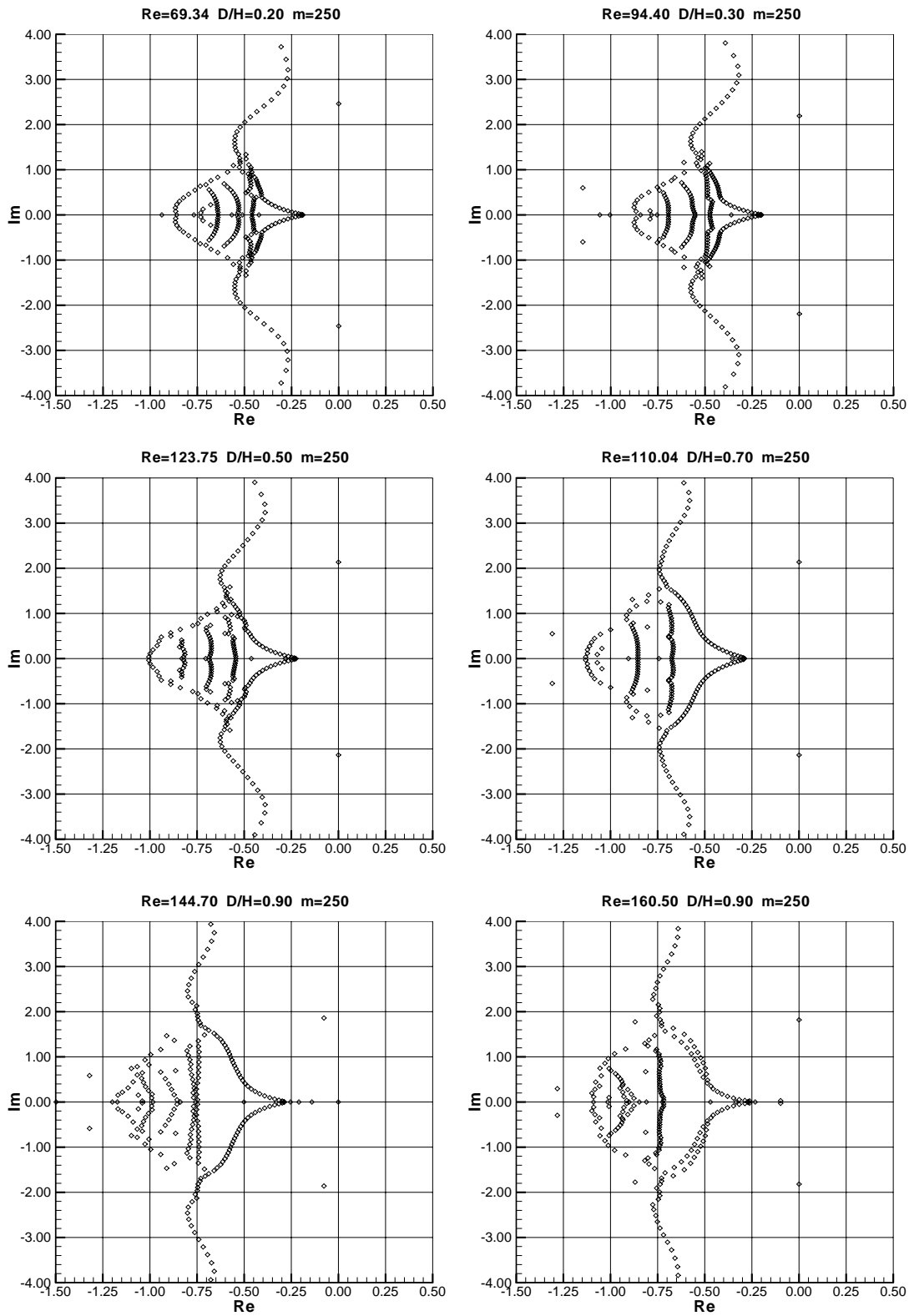


Figure 5.7: Reciprocal Ritz values computed on mesh M3 for different blockage ratios with Krylov space dimension $m = 250$ and shift parameter $\lambda = 0$.

Curve section (See Fig. 5.6)	Λ	m	M1		M2		M3		Chen et al.	
			Re_{crit}	St_{crit}	Re_{crit}	St_{crit}	Re_{crit}	St_{crit}	Re_{crit}	St_{crit}
AC	0.10	500	51.00	0.1206	50.81	0.1210	50.75	0.1211	51.77	0.1116
	0.20	250	69.86	0.1559	69.43	0.1566	69.34	0.1567	69.93	0.1559
	0.30	250	95.24	0.2079	94.56	0.2090	94.40	0.2093	94.85	0.2085
	0.50	250	125.23	0.3369	124.09	0.3393	123.75	0.3399	124.58	0.3382
	0.70	250	111.32	0.4714	110.29	0.4752	110.04	0.4762	111.04	0.4744
	0.80	250	111.45	0.5324	110.24	0.5363	109.98	0.5374		
	0.84	250	114.44	0.5530	113.69	0.5568				
	0.84	250	130.92	0.5510	126.64	0.5557				
	0.80	250	148.24	0.5324	144.19	0.5383	143.29	0.5398		
	0.76	250	169.75	0.5115	165.49	0.5186				
	0.72	250	198.94	0.4872	193.25	0.4955				
	0.70	250	218.03	0.4737	211.01	0.4827	209.40	0.4851		
CE	0.70	250	221.87		216.75		215.53			
	0.72	250	210.17		205.95					
	0.76	250	190.65		187.01					
	0.80	250	173.97		169.49		168.29			
	0.84	250	161.57		158.15					
	0.88	250	152.93		149.84					
	0.90	250	147.78		145.27		144.70			
CD	0.68	250	237.33	0.4596	231.06	0.4695				
	0.66	250	259.55	0.4477	253.08	0.4566				
	0.64	250	284.56	0.4351	278.01	0.4441				
	0.62	250	312.66	0.4235	306.27	0.4326				
FG	0.82	250			319.80	0.4664				
	0.82	250			227.44	0.4719				
	0.84	250	331.02	0.4954						
	0.84	250	214.00	0.4794	194.30	0.4979				
	0.88	250	180.43	0.5097	171.28	0.5234				
	0.90	250	169.44	0.5146	162.82	0.5202	160.50	0.5212		

Table 5.5: Convergence of critical Reynolds number for different blockage ratios with $\lambda = 0.00 \pm 0.00i$

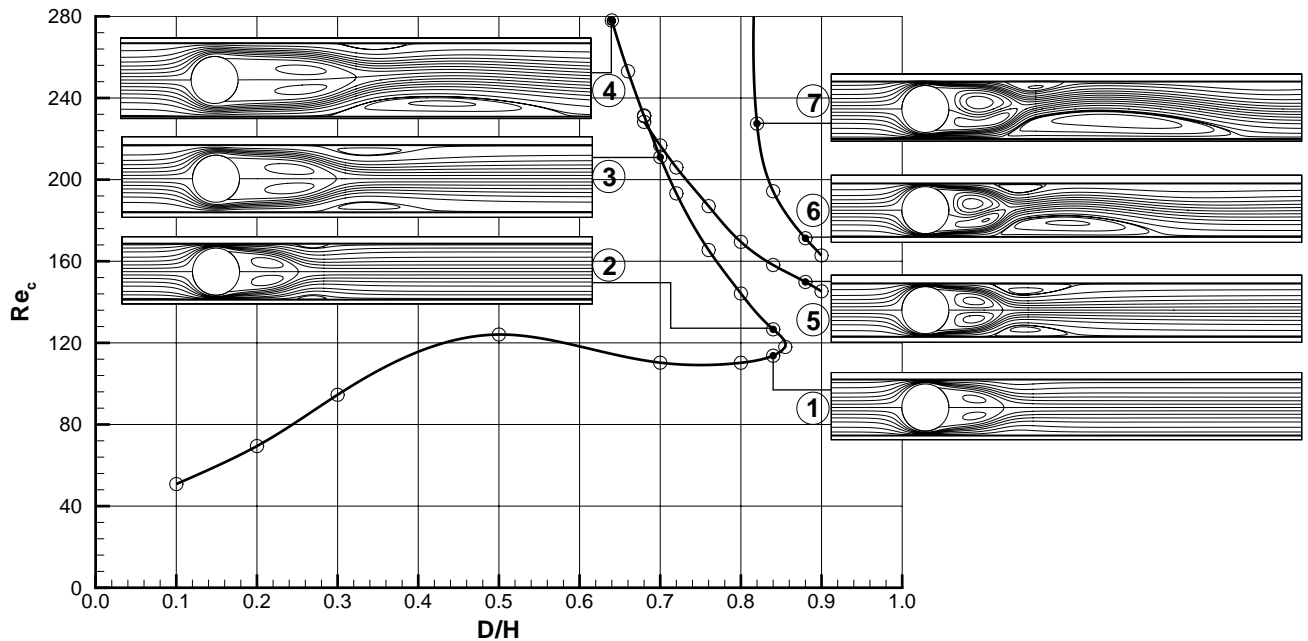


Figure 5.8: Change of base flow with critical Reynolds number and blockage ratio Λ , computed on M2.

problem we have been able to compare our critical Reynolds and Strouhal numbers for the bifurcation for the symmetric state with the values for these quantities computed by Chen et al. [29]. The available results ($0.1 \leq \Lambda \leq 0.7$) of the critical Reynolds number calculations of Chen et al. are plotted in Fig. 5.6 and agreement between our results and theirs over this limited section of the curve AB is excellent. Similarly excellent agreement in the computed Strouhal numbers was seen over the same range of blockage ratios, both our results and those of Chen et al. revealing a monotonic increase in the critical Strouhal number with the blockage ratio (see Table 5.5.)

Up to a blockage ratio $\Lambda = 0.5$ Table 5.5 and the neutral stability curve AB of Fig. 5.6 indicate that the flow becomes more stable to two-dimensional infinitesimal disturbances as the blockage ratio increases. The eigenspectrum resulting from the GEVP computed with the Krylov subspace dimension $m = 250$ and on mesh M3 for the points on AB corresponding to blockage ratios of 0.2, 0.3, 0.5 and 0.7 are shown in the upper four plots of Fig. 5.7. The positions of the leading eigenvalues indicate that the flow loses stability to a Hopf bifurcation and that the Strouhal number over this range of blockage ratios is increasing. Between $\Lambda = 0.75$ and 0.85 it may be seen from Table 5.5 and section AB of Fig. 5.6 that the flow restabilizes slightly leading up to point B ($\Lambda = \Lambda_B \approx 0.855$). In Fig. 5.8 we show the streamlines of the steady base flow at seven points on the neutral stability curves. Those corresponding to point 1 are typical of those at points on and below curve AB in Fig. 5.6 where the steady solution is symmetric and the only recirculatory region observed is the vortex pair immediately in the wake of the cylinder itself. That is, for solutions corresponding to parameter space on and below AB in Fig. 5.6 no flow separation on the walls is observed.

Curve sections BC and CE

In Fig. 5.6 section BC represents the part of the critical $\Lambda - Re$ curve on which the time-dependent state (symmetric periodic oscillations), passed into by crossing AB in the direction of increasing Reynolds number, restabilizes to a symmetric steady state once more. Further increases in the Reynolds number for blockage ratios in the range Λ_C to Λ_B or for choices of Λ greater than Λ_B may result in the steady symmetric solution becoming unstable to two-dimensional perturbations via a pitchfork bifurcation into one of two asymmetric states. The curve of neutral stability for this transition is labelled CE in Fig. 5.6.

The point C is a co-dimension 2 point where Hopf and pitchfork bifurcations occur simultaneously. We are able to estimate the coordinates (Λ_C, Re_{crit}) of this point by considering it to be the point of intersection of two straight lines drawn through the pairs of points on AC , CD and EC that correspond to $\Lambda = 0.68$ and 0.7 . Since $\Lambda = 0.68$ is outside the range of blockage ratios corresponding to EC the ordinate for this value of Λ is computed to be that at which the leading real eigenvalue in the spectrum of linear perturbations about the (linearly unstable) steady symmetric solution is at the origin. The critical Reynolds numbers at $\Lambda = 0.68$ and 0.7 computed on curves AC , CD and EC are detailed in Table 5.5 and lead to the estimate $(\Lambda_C, Re_{crit}) = (0.687, 224.142)$.

The occurrence of the transition from a symmetric steady state to an asymmetric one on CE is preceded (in Reynolds number) by the appearance in the streamlines of a pair of downstream separation bubbles on the walls. For example, in the eigenspectrum we observed that for $\Lambda = 0.9$ and at Reynolds numbers increasing up to approximately 110 the complex conjugate pair of leading eigenvalues moved in the direction of the positive real part of the spectrum. At a Reynolds number of around 110 separation bubbles appeared on the walls and with the appearance of the separation bubbles the leading eigenpair now started to move in the opposite direction while the eigenvalue on the real axis having largest real part moved right towards the origin. In Fig. 5.8 we plot the streamlines on BC at points 2 and 3 to demonstrate how the size of these recirculatory regions as well as their attachment distance downstream of the cylinder increase as C is approached along the curve BC . In the context of a circular cylinder near a plane boundary such downstream separation bubbles have been observed both experimentally [14] and numerically [160] for cylinders sufficiently close to the boundary.

To gain further insight into the flow transition from steady symmetric flow (between BC and CE and for $\Lambda \geq \Lambda_B$) via a pitchfork bifurcation to steady asymmetric flow (between DE and FG) we plot in Fig. 5.9 the streamlines of two solutions at a Reynolds number of 150 and blockage ratio of 0.9. It may be seen from Fig. 5.6 that this point lies between E ($Re = 144.7, \Lambda = \Lambda_E = 0.9$) and G ($Re = 160.5, \Lambda = \Lambda_G = 0.9$). Thus, the symmetric solution in the upper plot in Fig. 5.9 is linearly unstable and the lower plot represents the streamlines of one of the stable asymmetric solutions. The disturbance velocity \mathbf{v} in equation (2.4) is, of course, solenoidal. In Fig. 5.10 we plot the streamlines associated with the disturbance field and corresponding to the dominant eigenvalue at E . The addition of a multiple of the eigenvector shown in Fig. 5.10 to the symmetric steady base flow leads to one or other of the two asymmetric steady flows, the choice dependent on the direction of circulation around the symmetric streamlines in Fig. 5.10. An anti-clockwise direction leads to reinforcement of the lower recirculation region and reduction in the size of the upper bubble. A clockwise direction has the opposite effect. The drag coefficient associated with the steady asymmetric solution shown in Fig. 5.9 is slightly larger than that of the corresponding unstable symmetric one.

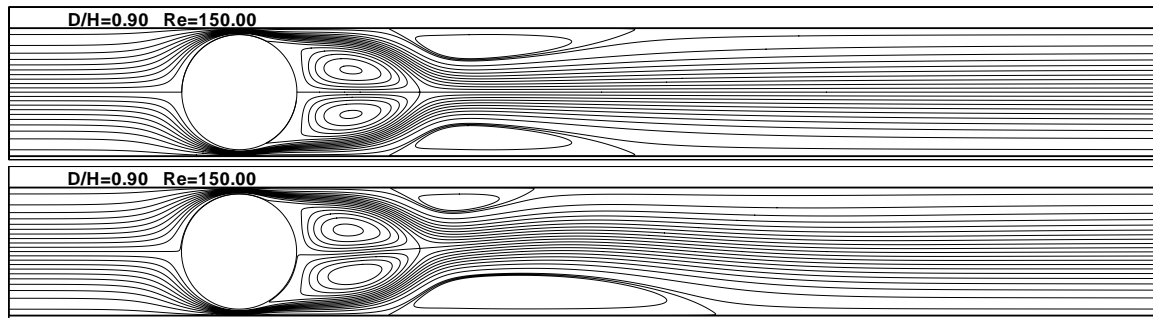


Figure 5.9: Streamlines of unstable symmetric and stable asymmetric solutions at $Re=150.00$ for $\Lambda = 0.9$ computed on M3.

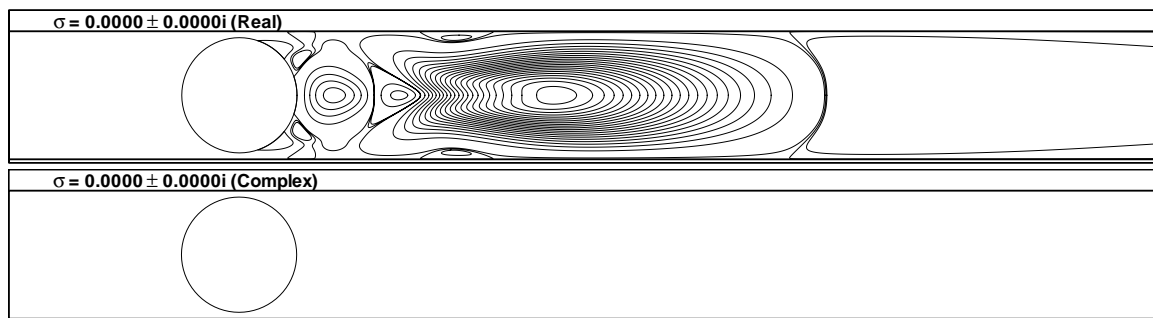


Figure 5.10: Streamlines for the disturbance velocity corresponding to the first leading eigenvector at $Re=144.70$ for $\Lambda = 0.9$ computed on M3.

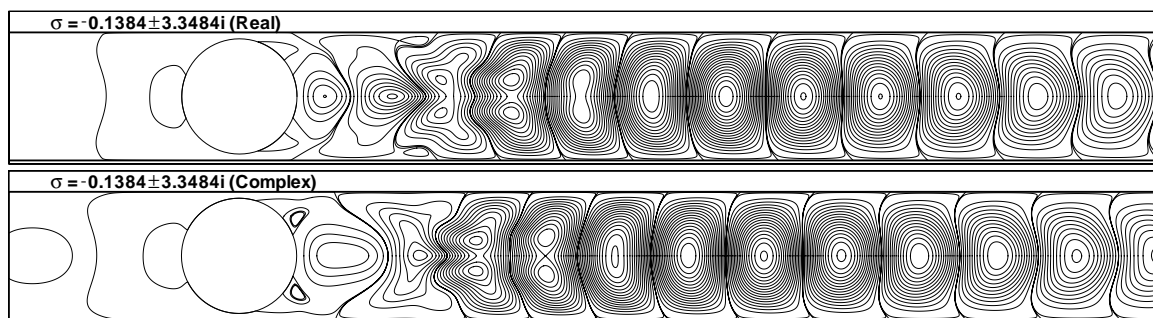


Figure 5.11: Streamlines for the disturbance velocity corresponding to the second leading eigenvector at $Re=144.70$ for $\Lambda = 0.9$ computed on M3.

The eigenspectrum at E is shown in the lower left plot of Fig. 5.7.

Curve section CD

The section of the neutral stability curves labelled CD in Fig. 5.6 represents a transition curve with increasing Λ from periodic vortex shedding to the left of this curve (smaller Λ) to a steady asymmetric state (larger Λ). At point C the steady solution is symmetric but moving along the curve CD towards D causes the growth of one of the recirculatory wall regions relative to the other.

Since all curves of neutral stability in Fig. 5.6 have been determined using a linear stability analysis about a steady flow as described in Sec. 5.2 we have been unable to plot the precise boundaries of the transition region that must exist from symmetric oscillations to asymmetric-in-time oscillations as the curve CD is approached in parameter space from the left (smaller Λ).

Curve section FG

Finally, the steady asymmetric solution of the region between curves DE and FG can become unstable via a Hopf bifurcation to unsymmetric vortex shedding (see discussion in Section 5.4.2). The transition curve is plotted as FG and the streamlines of two steady base flows at points 6 and 7 of this curve are shown in Fig. 5.8. In Fig. 5.11 we plot the streamlines of the disturbance velocity corresponding to the leading complex eigenvalue pair in the spectrum shown in the lower left-hand plot of Fig. 5.7 (point E). It is the addition of a mode similar in form to this (but at a higher Reynolds number) that leads to vortex shedding about the asymmetric state. The eigenspectrum for perturbations about the steady asymmetric base flow at F is shown in the lower right plot of Fig. 5.7. If the Reynolds number is further increased on the curve FG additional separation bubbles appear on the wall further downstream. We also remark that on the curve FG the separation bubble just behind the cylinder is generally shorter and more rounded than that computed on the curves BC and CD .

A strong parallel is thus seen in the present results with those of numerous other authors (see, for example [13, 41, 48, 67, 100, 110]) for flows through both two-dimensional and three-dimensional symmetric expansions. All the cited authors report that steady flow with symmetric recirculatory regions through an expansion geometry encounters a supercritical pitchfork bifurcation at a certain Reynolds number (dependent, of course, on the channel geometry) and becomes asymmetric. The difference in the streamwise attachment length of the two recirculatory regions (still in the steady regime) becomes larger as the Reynolds number is further increased from the critical value. In the two-dimensional case, increasing the expansion ratio decreases the critical Reynolds number [13]. In the three-dimensional case, Schrek and Schäfer [129] found that fixing the expansion ratio at 1 : 3 and decreasing the width of the channel relative to the downstream channel height from ∞ (two-dimensional flow) through 5 to 2 resulted in a stabilization of the flow.

It will be noted from Table 5.5 that for the choices of $\Lambda = 0.82$ and 0.84 critical Reynolds numbers of 319.8 and 331.02, respectively, are added to those that are shown in Fig. 5.6. This is to indicate how the curve FG would continue if the range of Reynolds numbers were to be extended in Fig. 5.6, although at these higher Reynolds numbers it is highly unlikely that the flow would in reality remain two-dimensional.

5.4.2 Direct numerical simulations

A few verifications were performed on the results of our direct numerical simulations in order to establish their reliability. First, Strouhal numbers near the critical Reynolds numbers corresponding to the onset of periodic vortex shedding and computed with direct numerical simulation were found to be in good agreement in a couple of cases with those predicted on the basis of the eigenvalue analysis of Section 5.4.1. For example, at a blockage ratio of $\Lambda = 0.3$ and at $Re = 100$ the corresponding Strouhal number was computed from the lift coefficient data over extended time intervals and found to be equal to 0.2115. This compares well with the value of 0.2090 supplied in Table 5.5 and computed at $Re_{crit} = 94.56$. Secondly, we present in Table 5.6 results of computations using the three meshes M1 to M3 of the drag on the cylinder for various blockage ratios. These are compared with the recent numerical data of Zisis and Mitsoulis [159] and Liu et al. [90] and the agreement is convincing. It should be further added that the drag result of Liu et al. for $\Lambda = 0.1$ is within 0.007% of the theoretically predicted value of Faxén [47]. The drag coefficient versus Reynolds number is given in Fig. 5.12 for several blockage ratios. At all the blockage ratios considered here the drag coefficient behaves like $1/Re$ at low Reynolds numbers. As the blockage ratio increases the range of values of Re over which this remains true gets larger. A full presentation of our predictions of C_l , C_d and St for blockage ratios from 0.1 to 0.9 and Reynolds numbers from 0.1 to 200 is to be found in Table 5.7.

In order to elucidate the variation in the critical Reynolds number with blockage ratio observed from the eigenvalue analysis of Section 5.4.1 we used direct numerical simulation to investigate the wake structure at five different locations in the $\Lambda - Re$ parameter space and labelled 1-5 in Fig. 5.13. As an aside and before discussing our results in detail we simply note that at blockage ratios $\Lambda < 0.5$ direct numerical simulations revealed that the vortex shedding over the cylinder was quite similar to that of the unbounded case, although the vortex street is shorter due to shear in the free stream.

Time-dependent solutions are presented in Fig. 5.14 for $\Lambda = 0.5$ at a Reynolds number of 200 (point 1 of Fig. 5.13). At this Reynolds number the flow has lost its stability to two-dimensional disturbances and has become time-periodic with $St = 0.3513$, which is higher than for unbounded flow around a circular cylinder ($St = 0.1965$). The sequences of three “snapshots” in Fig. 5.14 are taken at times $t = 0$, $T/3$ and $2T/3$, the period T being approximately equal to 2.85 and determined from the lift coefficient data (part of which is shown in Fig. 5.15) over long time periods. $t = 0$ corresponds to a minimum in the lift coefficient once fully periodic vortex shedding is established. In Fig. 5.16 we show the $C_d - C_l$ phase-space plot and the average lift is zero. It may be seen from Fig. 5.14(a)-(c) that vortex shedding occurs both from the cylinder and the channel walls. As these vortices move downstream the trajectories of clockwise vortices shed from the upper part of the cylinder cross those having opposite sign (and shed from the lower part of the cylinder) so that wall proximity effects are seen to give rise to a reverse von Kármán street. The same phenomenon has been documented by other authors [160].

At a blockage ratio of 0.7 the flow is periodic at a Reynolds number of 200.00 (point 2 of Fig. 5.13) with $St = 0.4881$. The streamlines and vorticity contours at times $t = 0$, $T/3$ and $2T/3$ are shown in Fig. 5.17(a)-(c), with the period $T \approx 2.05s$. Unlike in the case of $\Lambda = 0.5$ described in the paragraph above, vortex shedding from the cylinder seems to be almost suppressed at this Reynolds number, due to the proximity of point 2 to the curve of

Λ	M1	M2	M3	Extrapolated	Zisis & Mitsoulis	Liu et al.
0.1	8.9125	8.9100	8.9089	8.9080	8.912	8.9067
0.2	1.6221×10^1	1.6215×10^1	1.6211×10^1	1.6200×10^1	-	-
0.3	2.7923×10^1	2.7910×10^1	2.7902×10^1	2.7886×10^1	-	-
0.5	8.8354×10^1	8.8294×10^1	8.8263×10^1	8.8227×10^1	8.8207×10^1	8.8227×10^1
0.7	4.0347×10^2	4.0318×10^2	4.0299×10^2	4.0257×10^2	-	-
0.9	7.7057×10^3	7.6988×10^3	7.6959×10^3	7.6941×10^3	-	-

Table 5.6: Comparison with the results of Zisis and Mitsoulis [159] and Liu et al. [90] of computed total drag at $Re=0.0$ for different blockage ratios Λ .

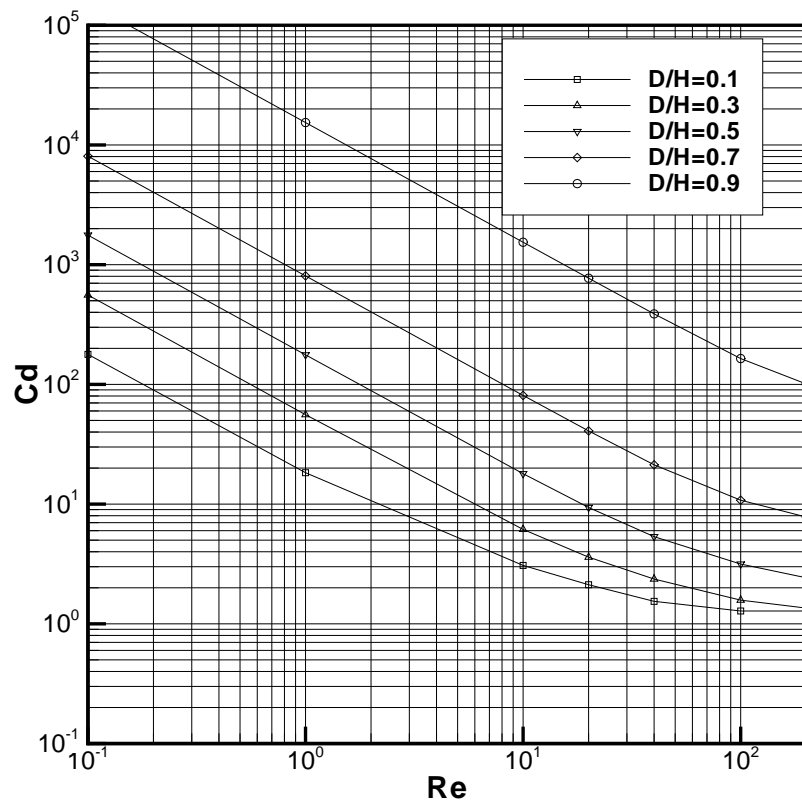


Figure 5.12: Computed drag coefficient versus Reynolds number at blockage ratios $\Lambda = 0.1, 0.3, 0.5, 0.7$ and 0.9 .

Λ	C_d	C_l	St
Re=0.10			
0.10	1.7823×10^2		
0.20	3.2423×10^2		
0.30	5.5804×10^2		
0.50	1.7653×10^3		
0.70	8.0598×10^3		
0.90	1.5392×10^5		
Re=1.00			
0.10	1.8298×10^1		
0.20	3.2574×10^1		
0.30	5.5875×10^1		
0.50	1.7656×10^2		
0.70	8.0601×10^2		
0.90	1.5392×10^4		
Re=10.00			
0.10	3.0758		
0.20	4.1081		
0.30	6.1464		
0.50	1.7957×10^1		
0.70	8.0891×10^1		
0.90	1.5400×10^3		
Re=20.00			
0.10	2.1218		
0.20	2.6248		
0.30	3.6052		
0.50	9.3786		
0.70	4.0874×10^1		
0.90	7.7124×10^2		
Re=40.00			
0.10	1.5412		
0.20	1.8264		
0.30	2.3664		
0.50	5.3470		
0.70	2.1298×10^1		
0.90	3.8816×10^2		
Re=100.00			
0.10	1.2799 ± 0.0084	± 0.3066	0.1607
0.20	1.3222 ± 0.0039	± 0.2231	0.1718
0.30	1.5770 ± 0.0004	± 0.0943	0.2115
0.50	3.1570		
0.70	1.0782×10^1		
0.90	1.6438×10^2		
Re=200.00			
0.10	1.2768 ± 0.0416	± 0.6446	0.1932
0.20	1.2385 ± 0.0328	± 0.5718	0.1948
0.30	1.3540 ± 0.0191	± 0.4826	0.2216
0.50	2.4250 ± 0.0034	± 0.2556	0.3513
0.70	7.8013 ± 0.0003	± 0.0993	0.4881
0.90	$1.0092 \times 10^2 \pm 1.1676$	± 6.9909	0.5314

Table 5.7: Comparison of computed lift coefficient C_l , drag coefficient C_d and Strouhal number St on M2.

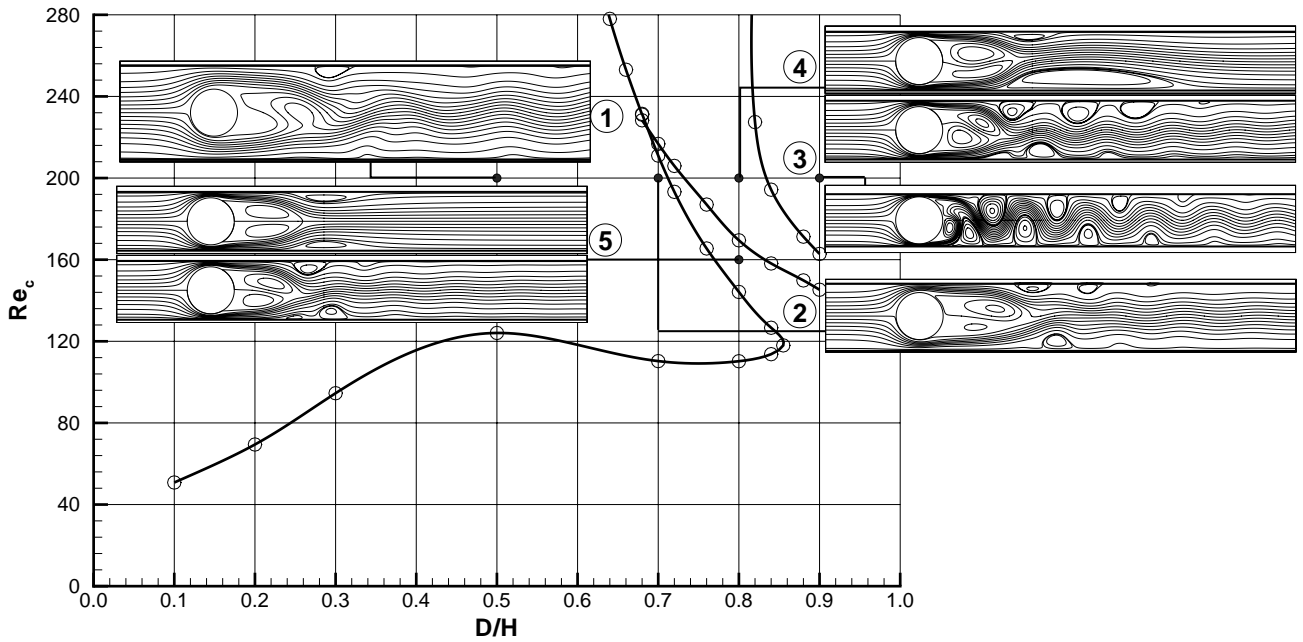


Figure 5.13: Change of time-dependent flow with Reynolds number and blockage ratio Λ , computed on M2.

neutral stability BC . However, there are very weak vortices shed from both upper and lower lateral walls. These are well separated from each other and their interaction is weak. The graphs of the lift and drag coefficients at this blockage ratio are shown in Fig. 5.18 over several cycles of the vortex shedding. Although the time-averaged value of the drag coefficient C_d has increased it is notable that the amplitude of the C_d oscillations is an order of magnitude less than that seen at $\Lambda = 0.5$. It may be seen more clearly from Fig. 5.19 that the average lift is slightly larger than zero.

At a blockage ratio of 0.9 and $Re > 160.5$ the flow is unsteady and very strong vortices are shed from both the cylinder and the walls. The computed streamlines and vorticity contours at $Re = 200.00$ (point 3 of Fig. 5.13) are shown in Fig. 5.20(a)-(c), each separated from the previous in the series by a third of a period $T/3$. At this Reynolds number the flow is periodic with $St = 0.5314$ ($T \approx 1.88$) and this compares reasonably well (see Table 5.5) with the Strouhal number of 0.5202 computed from the GEVP on mesh M2 at the critical Reynolds number $Re_{crit} = 162.82$. Vortices having the same sign merge just behind the cylinder and are then transported downstream. However, the vortex street formed behind the cylinder is quite different from the well-known von Kármán street in that very strong opposite-sign vortices with smaller structure move downstream and interact with the wall, creating strong vortices there. Although the streamlines of the eigenvector shown in Fig. 5.11 will be slightly modified by the time the Reynolds number reaches 200, the size of the cellular structures in the wake of the eigenvector are close to what is seen in the direct numerical solution for the vorticity in Fig. 5.20. Oscillations are now about an asymmetric state and lead to drastic increases in both the lift and drag coefficient values. Their variation with dimensionless time is shown in Fig. 5.21 and their phase-space plot is shown in Fig. 5.22. In this figure it may be seen that not only is the time-averaged value of C_d greater than for the two previous blockage ratios

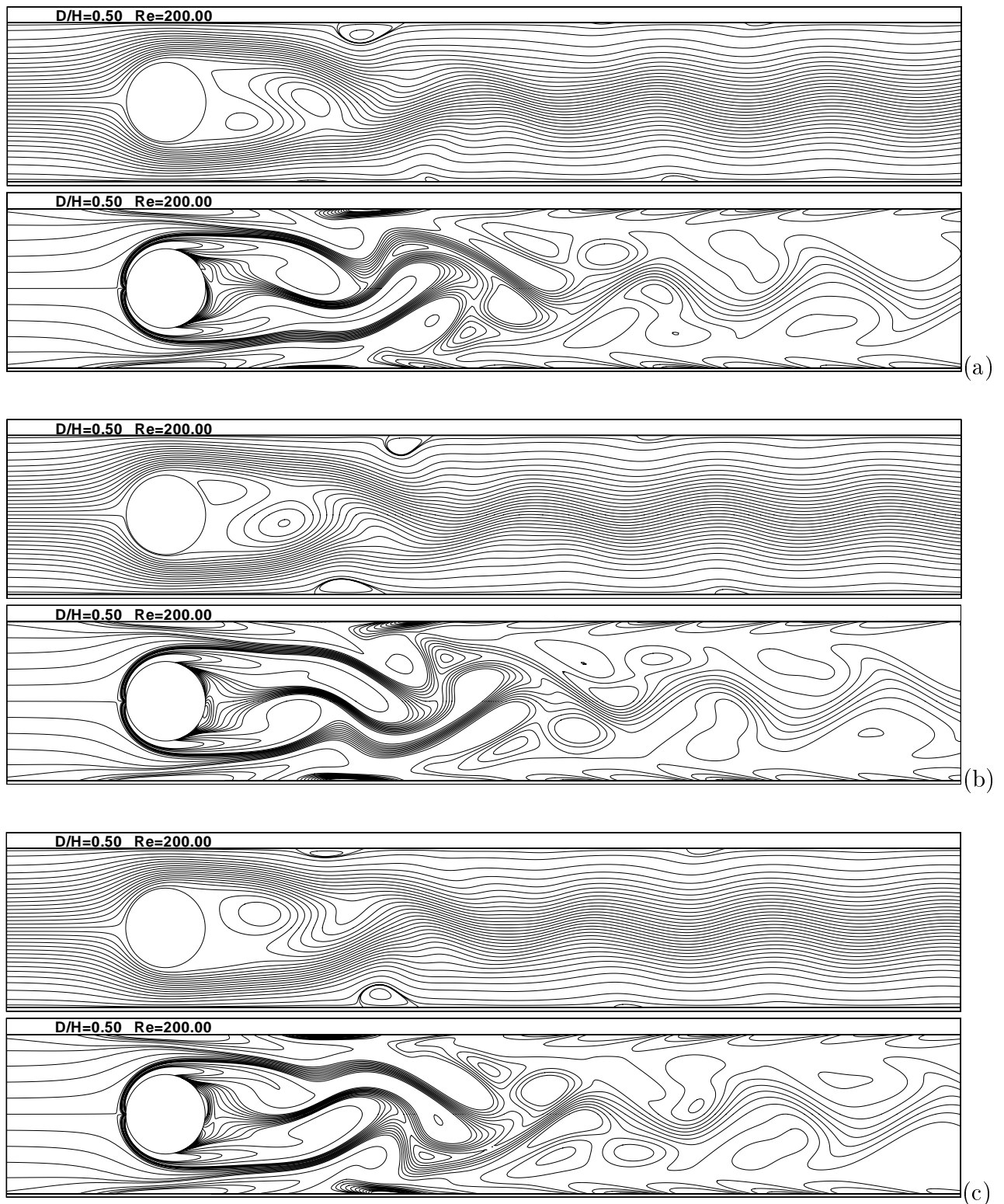


Figure 5.14: Streamlines (upper plots) and vorticity contours (lower plots) of the periodic flow at (a) $t = 0$, (b) $T/3$ and (c) $2T/3$ for $Re = 200.00$ and $\Lambda = 0.5$ (point 1 in Fig. 5.13) computed on M2. $t = 0$ corresponds to the solution having minimum lift coefficient and the period $T \approx 2.85$.

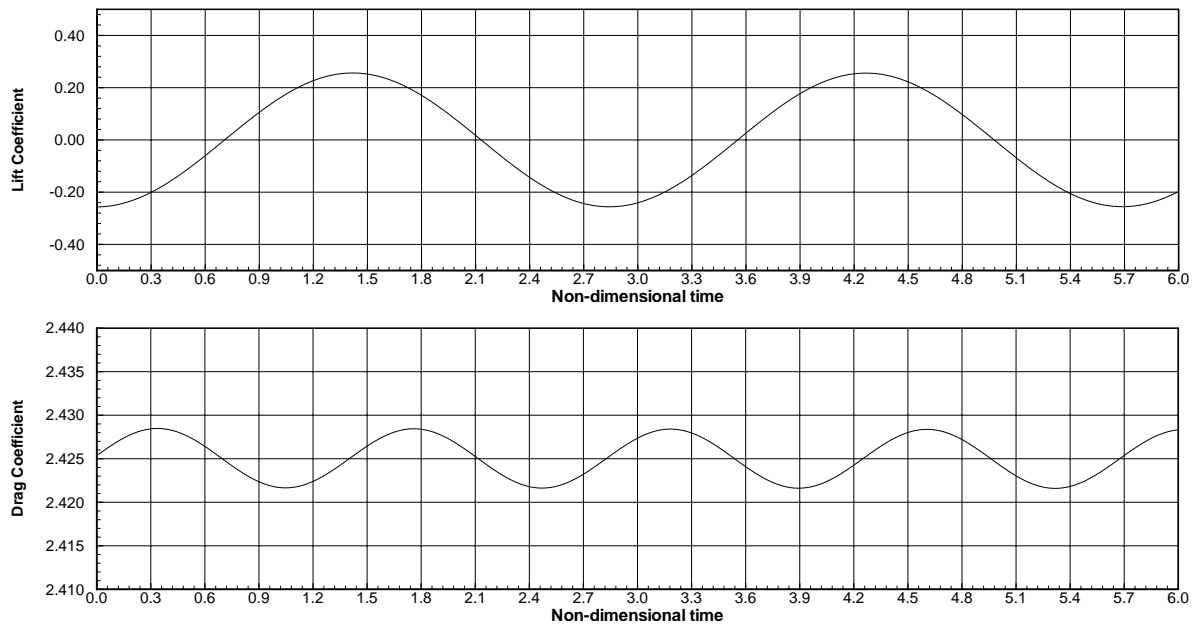


Figure 5.15: Time variation of lift and drag coefficients with non-dimensional time (tU_{max}/D) at $Re=200.00$ for $\Lambda = 0.5$ (point 1 in Fig. 5.13) computed on M2.

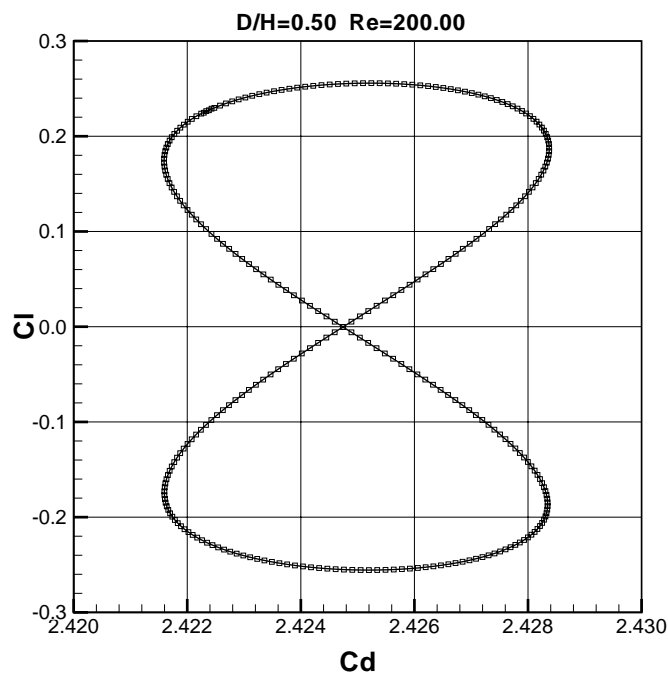


Figure 5.16: Phase-space plots of lift and drag coefficients parametrized with non-dimensional time (tU_{max}/D), computed on M2 at $Re = 200.00$ and $\Lambda = 0.5$ (point 1 in Fig. 5.13).

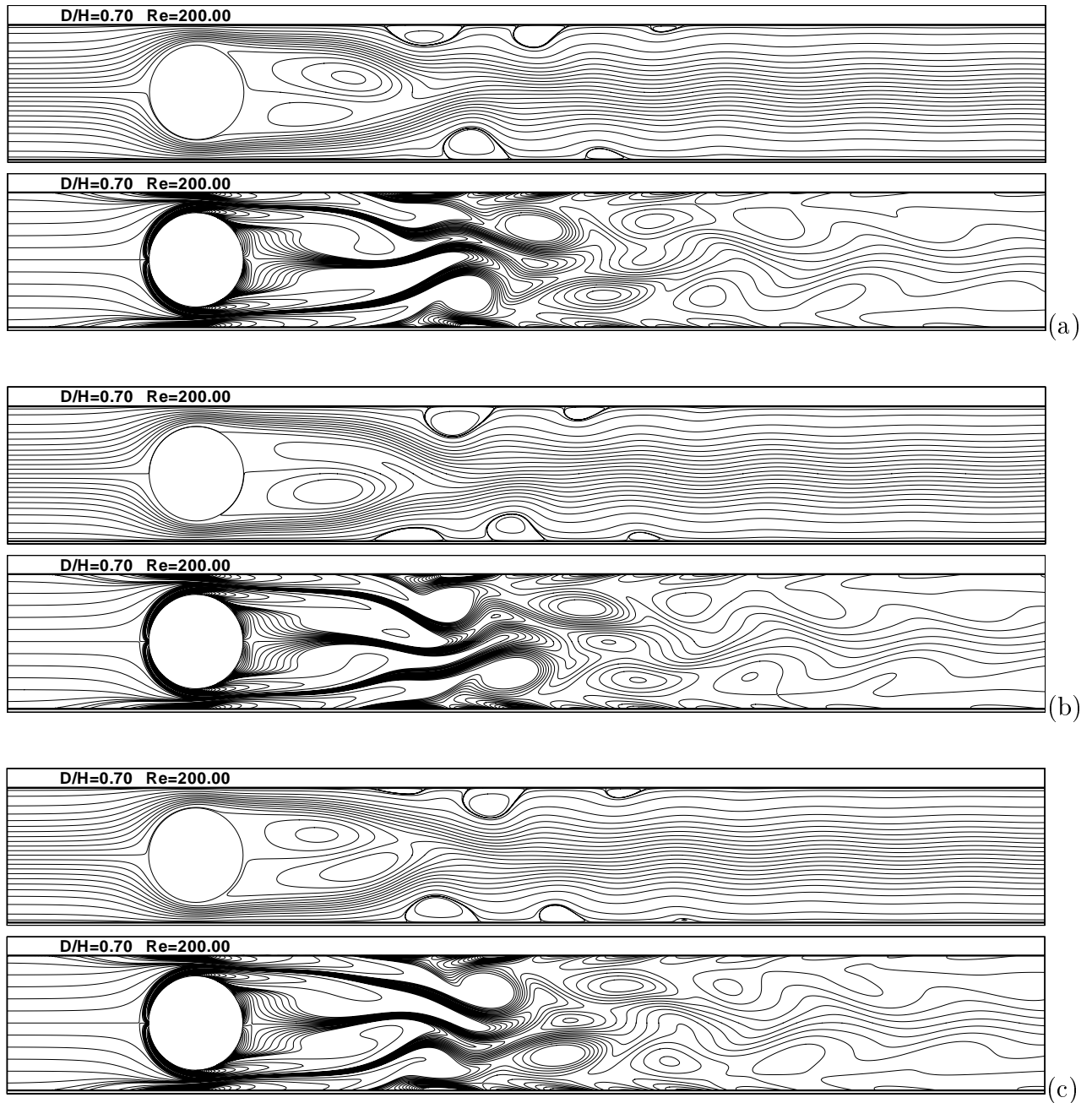


Figure 5.17: Streamlines (upper plots) and vorticity contours (lower plots) of the periodic flow at (a) $t = 0$, (b) $T/3$ and (c) $2T/3$ for $Re=200.00$ and $\Lambda = 0.7$ (point 2 in Fig. 5.13) computed on M2. $t = 0$ corresponds to the solution having minimum lift coefficient and the period $T \approx 2.05$.

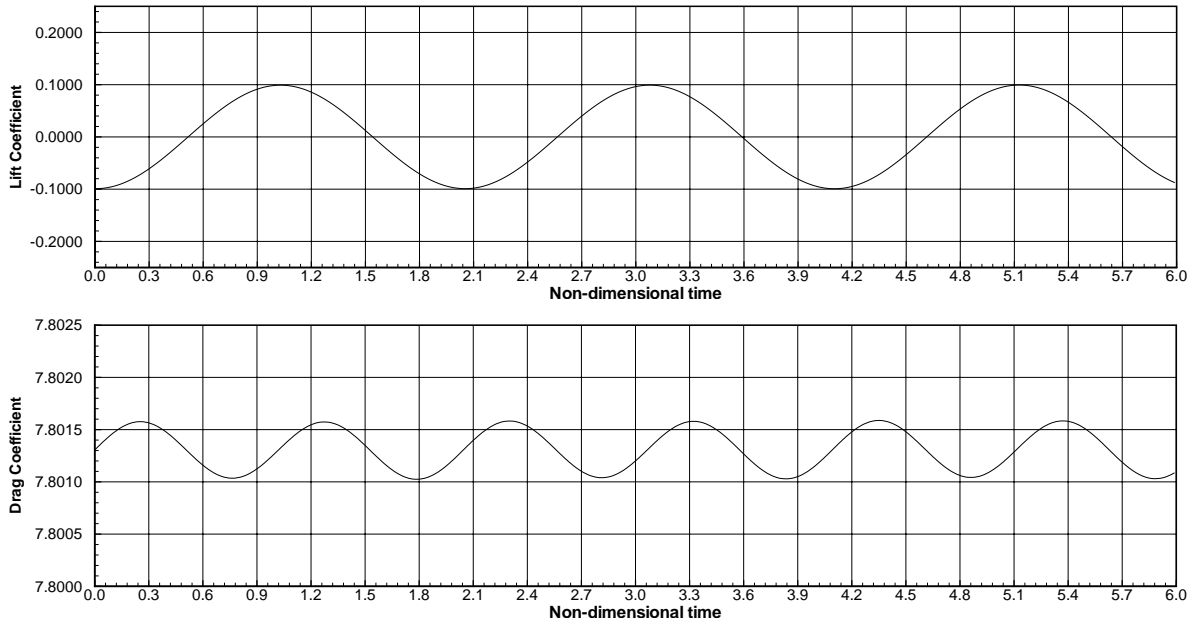


Figure 5.18: Time variation of lift and drag coefficients with non-dimensional time (tU_{max}/D) at $Re=200.00$ for $\Lambda = 0.7$ (point 2 in Fig. 5.13) computed on M2.

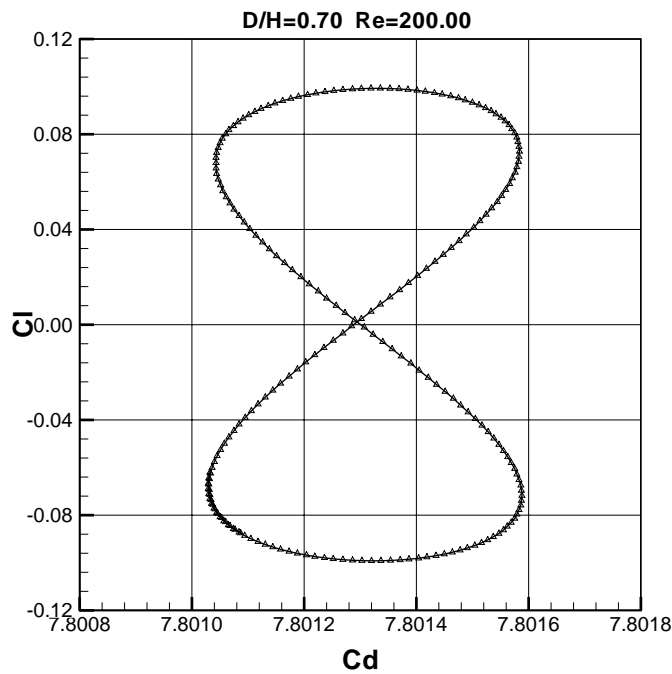


Figure 5.19: Phase-space plots of lift and drag coefficients parametrized with non-dimensional time (tU_{max}/D), computed on M2 at $Re = 200.00$ and $\Lambda = 0.7$ (point 2 in Fig. 5.13).

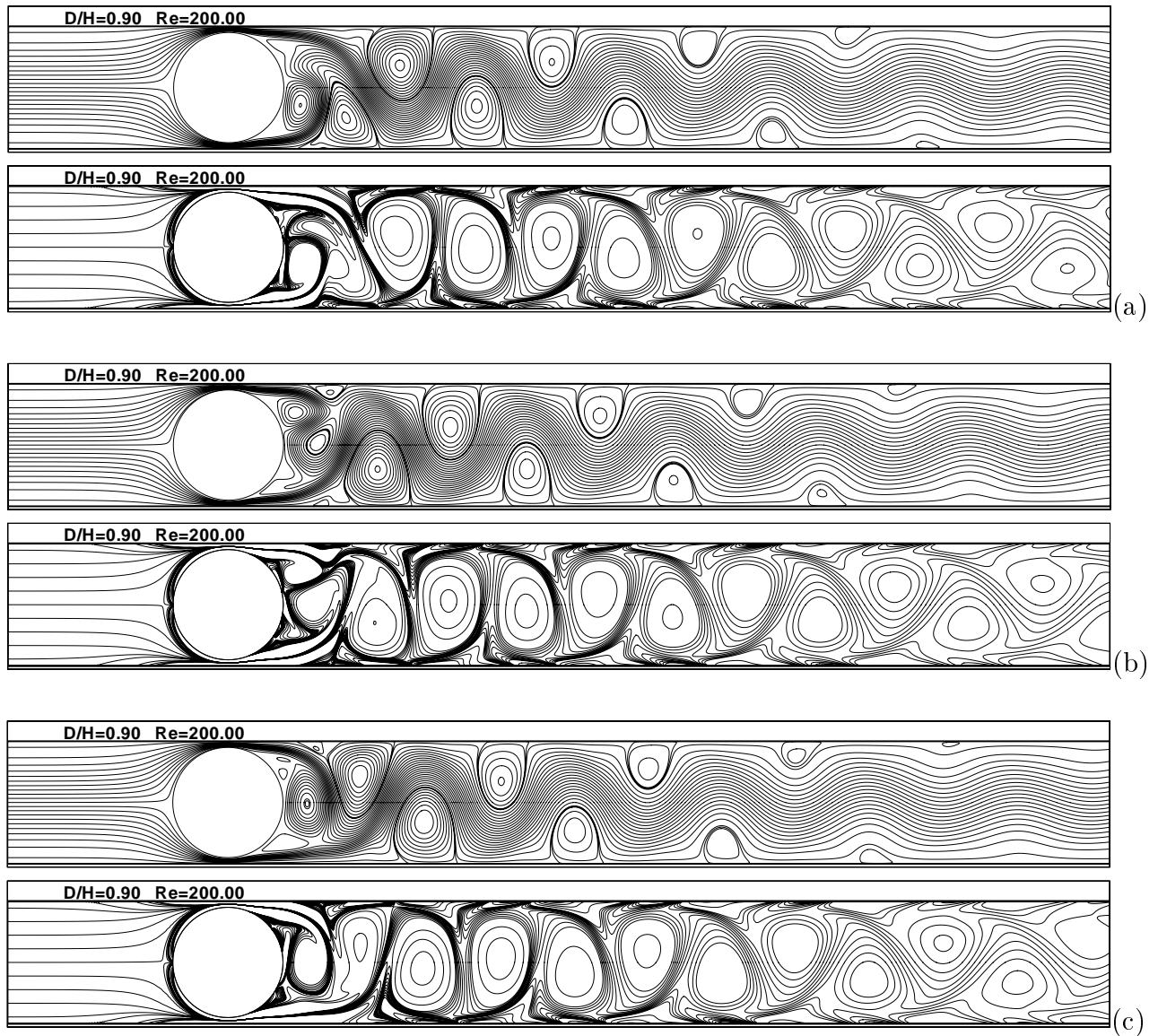


Figure 5.20: Streamlines (upper plots) and vorticity contours (lower plots) of the periodic solution at (a) $t = 0$, (b) $T/3$ and (c) $2T/3$ for $Re=200.00$ and $\Lambda = 0.9$ (point 3 in Fig. 5.13) computed on M2. $t = 0$ corresponds to the solution having minimum lift coefficient and the period $T \approx 1.88$.

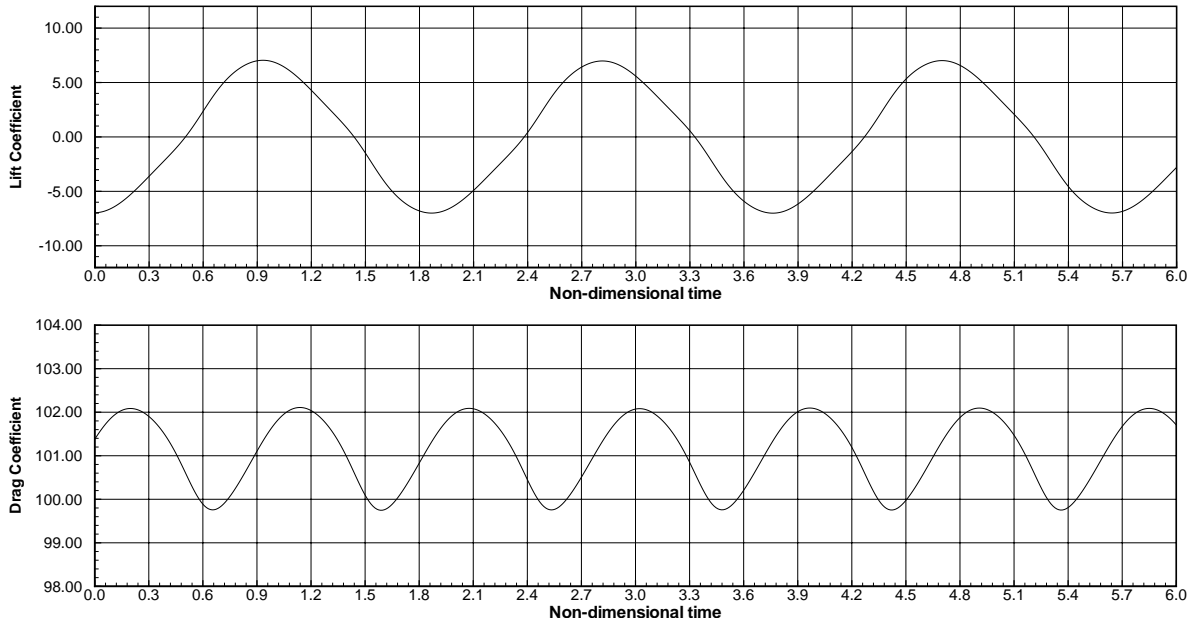


Figure 5.21: Time variation of lift and drag coefficients with non-dimensional time (tU_{max}/D) at $Re=200.00$ for $\Lambda = 0.9$ (point 3 in Fig. 5.13) computed on M2.

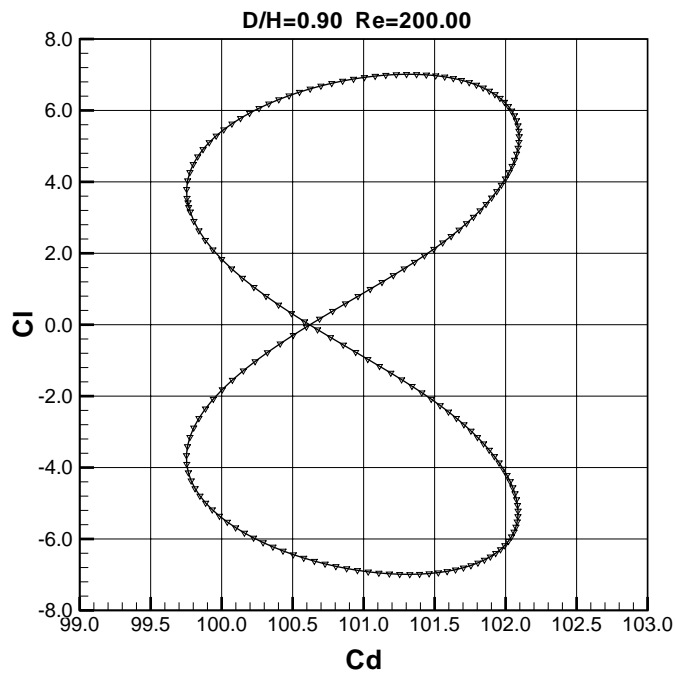


Figure 5.22: Phase-space plots of lift and drag coefficients parametrized with non-dimensional time (tU_{max}/D), computed on M2 at $Re = 200.00$ and $\Lambda = 0.9$ (point 3 in Fig. 5.13).

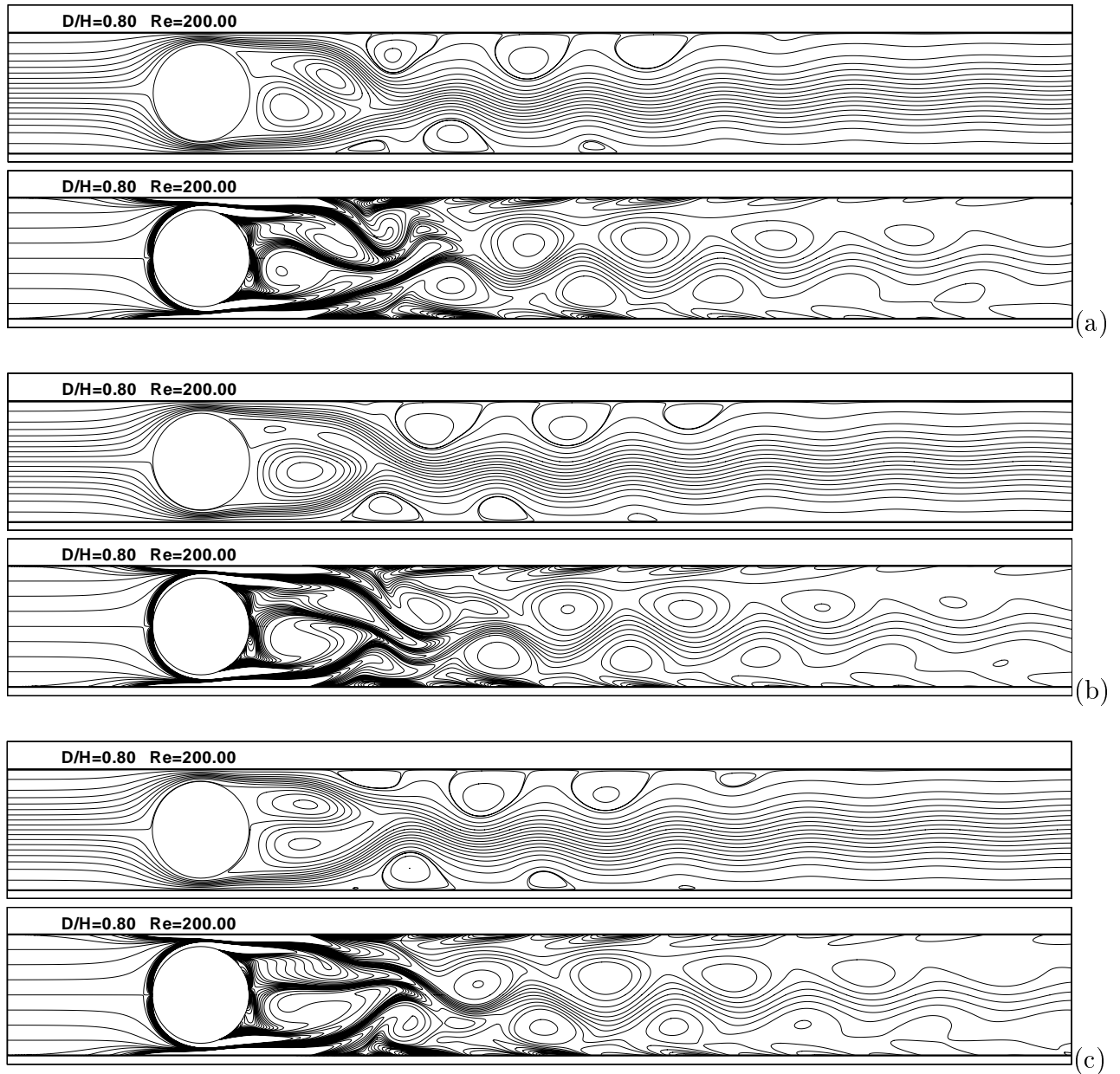


Figure 5.23: Streamlines (upper plots) and vorticity contours (lower plots) of the periodic solution at (a) $t = 0$, (b) $T/3$ and (c) $2T/3$ for $Re=200.00$ and $\Lambda = 0.8$ (point 4 in Fig. 5.13) computed on M2. $t = 0$ corresponds to the solution having minimum lift coefficient and the period $T \approx 1.815$.

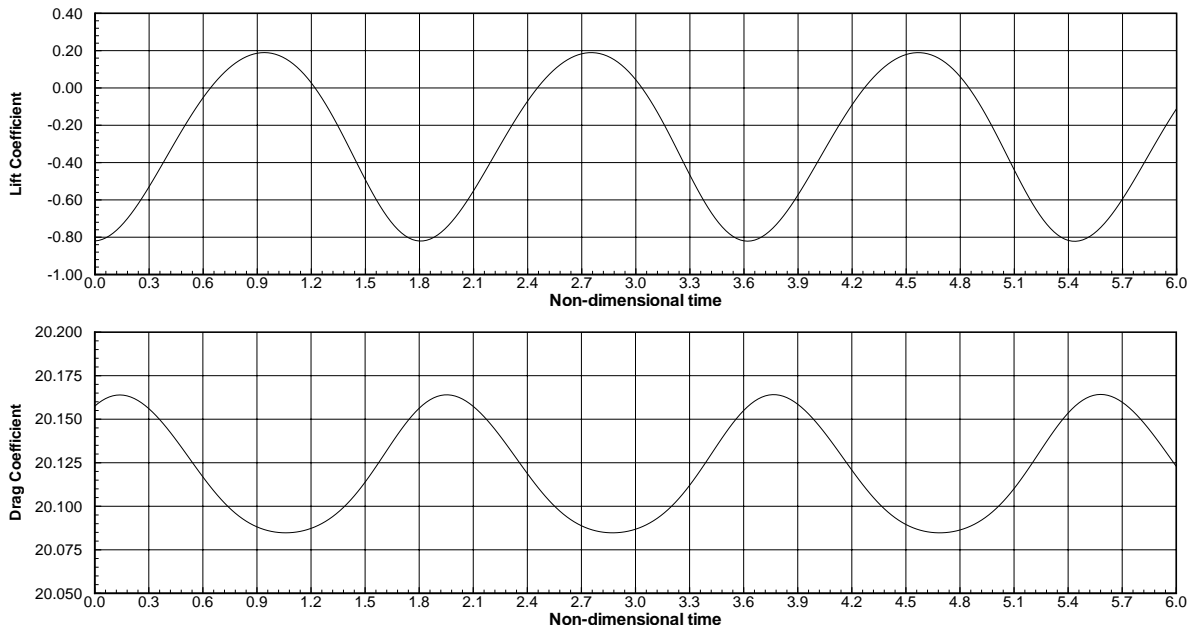


Figure 5.24: Time variation of lift and drag coefficients with non-dimensional time (tU_{max}/D) at $Re=200.00$ for $\Lambda = 0.8$ (point 4 in Fig. 5.13) computed on M2.

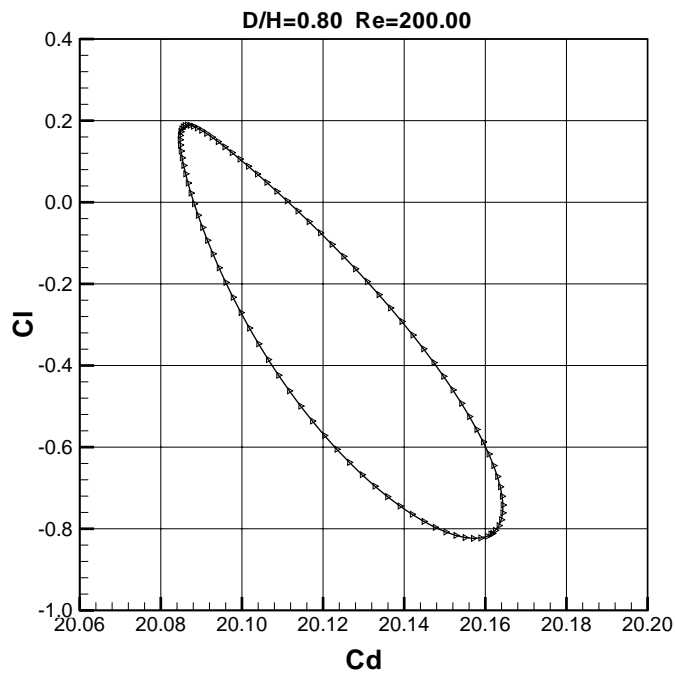


Figure 5.25: Phase-space plots of lift and drag coefficients parametrized with non-dimensional time (tU_{max}/D), computed on M2 at $Re = 200.00$ and $\Lambda = 0.8$ (point 4 in Fig. 5.13).

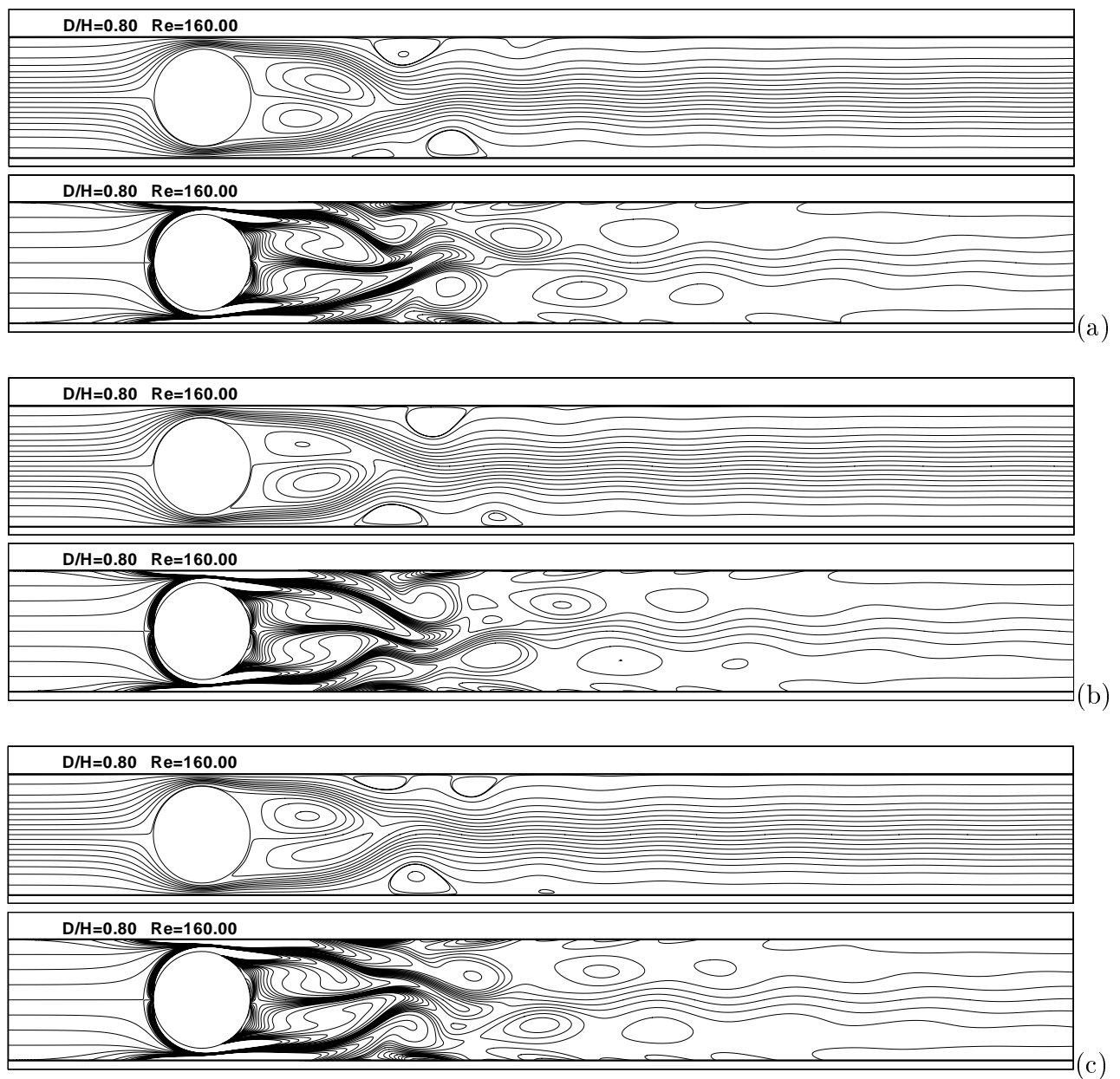


Figure 5.26: Streamlines (upper plots) and vorticity contours (lower plots) of the periodic solution at (a) $t = 0$, (b) $T/3$ and (c) $2T/3$ for $Re = 160.00$ and $\Lambda = 0.8$ (point 5 in Fig. 5.13) computed on M2. $t = 0$ corresponds to the solution having minimum lift coefficient and the period $T \approx 1.806$.

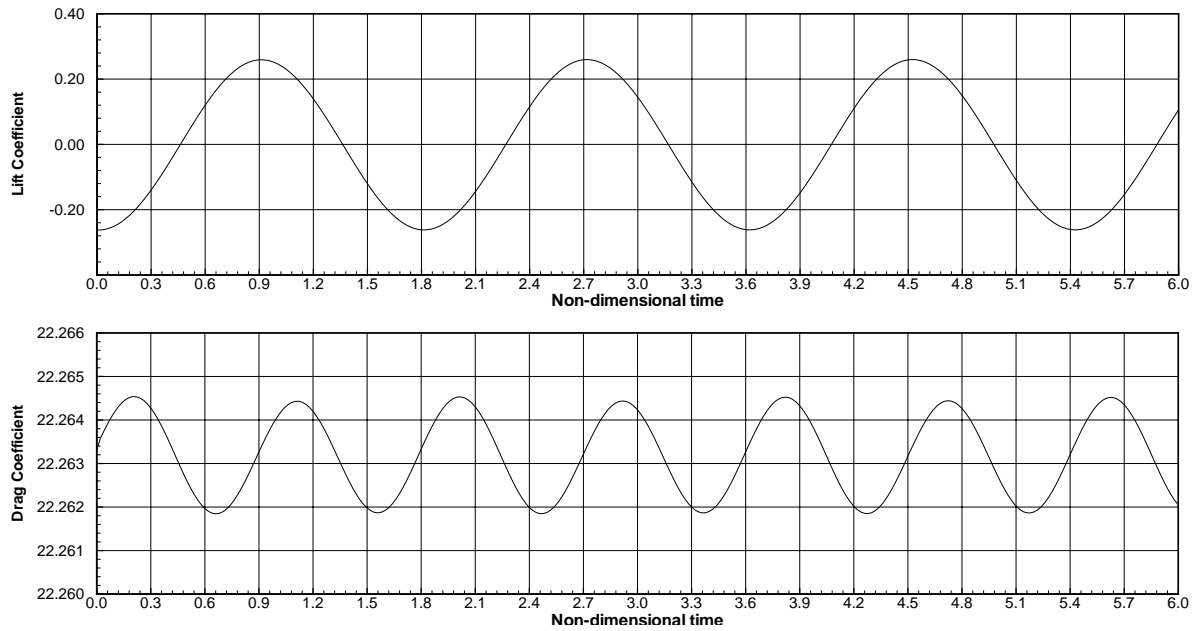


Figure 5.27: Time variation of lift and drag coefficients with non-dimensional time (tU_{max}/D) at $Re=160.00$ for $\Lambda = 0.8$ (point 5 in Fig. 5.13) computed on M2.

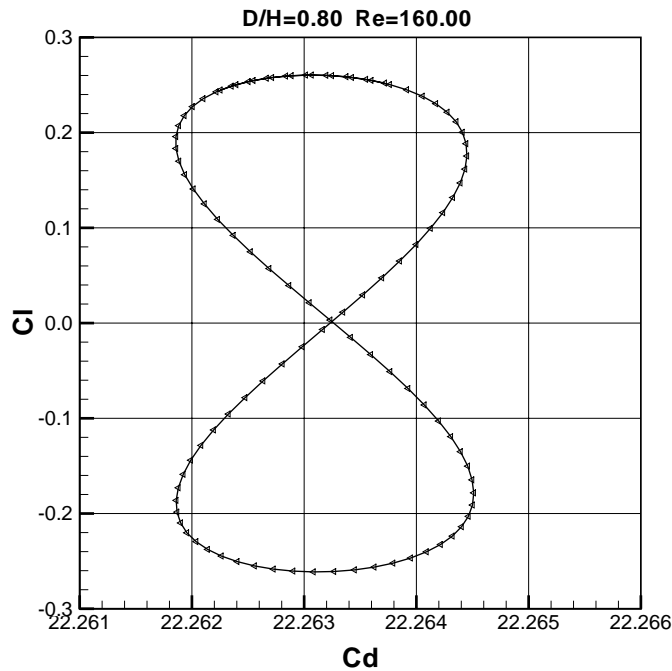


Figure 5.28: Phase-space plots of lift and drag coefficients parametrized with non-dimensional time (tU_{max}/D), computed on M2 at $Re = 160.00$ and $\Lambda = 0.8$ (point 5 in Fig. 5.13).

considered, but the amplitudes of oscillation of both coefficients has dramatically increased after a tendency observed up to $\Lambda \approx 0.75$ of successively diminishing amplitudes. We also note for the first time that the lift coefficient is no longer symmetric in the rising and falling parts of each cycle, due to the fact that the base flow is itself asymmetric.

The flow behavior in the parametric region between curves BD and FG is particularly interesting since although the steady base flow solutions are linearly stable they appear to be finitely unstable. Although our primary concern in this chapter is the study of wall effects on the *linear* stability of flow past a confined cylinder, in Fig. 5.13 we plot the instantaneous streamlines of two pairs of different solutions, both pairs being for a blockage ratio $\Lambda = 0.8$ but corresponding to two different values of Re : at point 4 $Re = 200$ whereas at point 5 $Re = 160$. Shown in the uppermost plots at points 4 and 5 are the steady and linearly stable solutions, but these may be sent into permanently unsteady states by running, for example, the time-dependent code with the geometrically-rescaled steady base flow of point 2 ($\Lambda = 0.7$, $Re = 200$) as the initial “guess”. Snapshots of unsteady flow at times $t = 0$, $T/3$ and $2T/3$ at point 4 are presented in Fig. 5.23(a)-(c), with the period $T \approx 1.815$. Unlike the other unsteady cases considered so far in this chapter, the recirculation regions on the upper wall are much larger than those on the lower wall and they can move far downstream. Additionally, the recirculatory region at the lower part of the cylinder is larger than that at the upper part. This asymmetry may be seen from the lift coefficients in Fig. 5.24 and Fig. 5.25. The time average of the lift coefficient is no longer zero and the lift curve is asymmetric in the rising and falling part of each cycle, similar to that at point 3. However if the Reynolds number is chosen equal to 160 (point 5 in Fig. 5.13) the time average of the flow becomes symmetric since point 5 is below the curve CE . The computed streamlines and vorticity contours are given in Fig. 5.26(a)-(c) with $T \approx 1.806$. At this point the flow structure is quite similar to that of point 2 with vortex shedding from the upper and lower walls. The lift and drag coefficients which are given in Fig. 5.27 and 5.28 are also similar to those of point 2 with zero time average of the lift coefficient.

Numerical experiments at a blockage ratio of 0.9 and a Reynolds number of 500 indicated that the flow had become chaotic. However, it seems unlikely that the flow is still two-dimensional at this Reynolds number and presentation of our results will have to await a fully three-dimensional analysis.

5.5 Conclusions

In this chapter we have computed with greater accuracy and over a larger range of blockage ratios than has proved possible in the past the effects on the drag and linear stability of lateral wall proximity for flow past a cylinder at Reynolds numbers up to 280.

Some of the rich and complex dynamics of the system for sufficiently high Reynolds numbers and blockage ratios have been uncovered and discussed. In particular, we have found that for $Re \leq 280$ and $\Lambda \leq 0.9$ there are (at least) three separate curves of neutral stability: (a) Hopf bifurcation of a symmetric state, (b) pitchfork bifurcation of a symmetric state to one of two asymmetric states, and (c) Hopf bifurcation of an asymmetric state leading to asymmetric oscillations thereafter. In addition, we have drawn attention to a transition region from symmetric vortex shedding to asymmetric vortex shedding with increasing blockage ratio. Further increases in the blockage ratio (crossing CD in Fig. 5.13) leads to restabilization to a steady asymmetric solution.

A co-dimension 2 point where pitchfork and Hopf bifurcations occur simultaneously has been identified and a region in parameter space (either side of the locus of the pitchfork bifurcation) seems to exist where the steady solution is linearly stable but unstable to finite two-dimensional perturbations.

Chapter 6

Viscoelastic Flow Past a Confined Circular Cylinder

6.1 Introduction

Literally hundreds of papers, both experimental and numerical, have appeared in the scientific literature on the subject of bluff body wake instabilities since the pioneering work of von Kármán in 1912 [147]. In his recent review of the literature Williamson [153] includes a recapitulation of the now well-known vortex shedding regimes observed in unbounded flows of Newtonian fluids past a single cylinder. For Reynolds numbers up to about 260 Williamson identified two principal regimes. Firstly, at a Reynolds number greater than approximately 49, transition to two-dimensional laminar vortex shedding is via a supercritical Hopf bifurcation and manifests itself through increases in the amplitude of the maximum wake velocity fluctuations and a decrease in the formation length (distance downstream of the cylinder to the point where the rms velocity fluctuations are a maximum). Second, in the so-called wake-transition regime, three-dimensional vortical instabilities are seen from Reynolds numbers of approximately 190 onwards and this regime is characterized by two distinct discontinuities in the Strouhal number-Reynolds number curve [150]. The first (hysteretic) discontinuity marks the appearance of vortex loops, streamwise vortex pairs being shed at wavelengths of approximately 3-4 cylinder diameters (mode A instability [152]) whilst the second (mode B instability) appears in the Reynolds number range 230 to 250 and is typified by finer-scale streamwise vortices. More details of these vortex shedding regimes may be found in Section 5.4.2.

We divide our review of research results on viscoelastic bluff body wake instabilities into subsections dealing with (a) purely elastic ($Re = 0$) instabilities in the wake of bluff bodies and (b) the influence of polymer additives on shear instabilities in the wake for sufficiently large Reynolds numbers.

6.1.1 Purely elastic instabilities

The first experimental study of elastic instabilities in creeping viscoelastic flow past a confined cylinder was made by McKinley and co-workers [94] in 1993. The authors worked with a Boger-type fluid consisting of a very dilute solution of polyisobutylene (PIB) in a polybutene/tetradecane solvent and the geometry consisted of a cylinder mounted centrally in a rectangular channel with a blockage ratio Λ (equal to the ratio of the cylinder diameter to

the channel height) taken for most of the experiments equal to 0.5. At a shear-rate-dependent Deborah number De of 1.3 and at a Reynolds number not exceeding 0.05 a steady three-dimensional flow instability confined to the narrow region of strongly extensional flow near the rear stagnation point of the cylinder was reported. The instability appeared as a three-dimensional cellular structure that extended along the length of the cylinder with spatially periodic oscillations in the axial velocity field profiles intensifying as the Deborah number was increased from 1.3. The wavelength of these flow perturbations scaled with the cylinder radius. A second flow transition, this time to a time-periodic instability was seen for $De \geq 1.85$, the cellular structure now moving slowly along the length of the cylinder towards the channel walls and time-dependent velocity oscillations being observed in the wake. Since 1993 other notable experimental investigations into purely elastic wake instabilities for flow past single confined cylinders or periodic arrays of cylinders are those of Byars [22], Liu [89] and Arora et al. [7] and more details of these are supplied at various points in the succeeding paragraphs.

Of fundamental importance has been the establishment of criteria for the critical conditions for the onset of the observed elastic instabilities. McKinley et al. [95] and Pakdel and McKinley [113] suggested in 1996 that for shear-dominated flows the destabilizing mechanism was a combination of streamline curvature and elastic normal stresses, giving rise to an extra tension along the streamlines, the onset Deborah number thus scaling with the streamline curvature. The analysis of McKinley et al. [95] seemed to do well in predicting the experimentally-determined critical Deborah numbers of Byars [22] and McKinley et al. [94] and, much more recently, Arora et al. [7] have confirmed that for their experiments with PIB-based Boger fluids in a periodically undulating channel and past a periodic array of closely-spaced cylinders, the onset Weissenberg numbers, when scaled with streamline curvatures for the two periodic flows, were very close to each other within experimental uncertainty. The authors therefore concluded that the observed instabilities arose from the coupling between streamline curvature and elastic normal stresses.

Attempts at numerically determining the linear stability and non-linear dynamics of creeping viscoelastic flow past isolated cylinders have met with only limited success and to date no purely elastic instability has been predicted numerically. In 1999 Sureshkumar et al. [139] investigated the linear stability of flow of an Oldroyd B fluid through a linear periodic array of cylinders and used a finite element DEVSS-G/SUPG/ θ method to solve the linearized transient perturbation equations. Results were presented for two-dimensional perturbations to two-dimensional flow with a blockage ratio Λ equal to 0.5. Denoting a cylinder radius by R , distances between successive cylinders ranged from $2.5R$ (closely spaced) to $30R$ (widely spaced). For Deborah numbers up to 0.71 the flow was predicted to be linearly stable for cylinder separations of $30R$ and $6R$. However, for the most closely spaced cylinders a critical Deborah number of approximately 0.64 was found, associated with a possible Hopf bifurcation from the base flow. No secondary flow was observed near the cylinder surface. Instabilities were also found for separation distances of $3R$ and $3.5R$ and the critical Deborah numbers for the onset of instabilities were shown to scale with the cylinder-to-cylinder separation distance.

A year later the same authors [133] reported that the calculations in [139] were not converged with mesh refinement and that in fact the numerical evidence now led to the conclusion that two-dimensional flow of an Oldroyd B fluid was stable to two-dimensional perturbations, even with a cylinder separation distance of $2.5R$. In [133] Smith et al. used SUPG and DG finite element discretizations and both the θ method and a fourth-order Runge-Kutta method for time integration of the linearized equations corresponding to three-dimensional perturba-

tions of two-dimensional Oldroyd B flow past a single confined cylinder at a blockage ratio of 0.5. Computations were continued up to a Weissenberg number of 0.75 and the flow was computed to be stable over this range, in contradiction with the experimental results of Byars [22], who reported a transition from the two-dimensional base flow to a three-dimensional cellular structure in the wake at a Weissenberg number of 0.5.

In an extension of their earlier paper, Smith et al. [134] used a DEVSS-G/SUPG/ θ method and a Krylov subspace method for computing a subset of the eigenspectrum that results from assuming the long-time response of the perturbations to have the form $\exp(\sigma t)$. Their analyses concerned the linear stability of two-dimensional base flows to three-dimensional perturbations. Although for a cylinder spacing of $2.5R$ there was remarkably good agreement with the critical Weissenberg number predicted by Liu [89] for flow of a PIB Boger fluid, two important discrepancies existed between the simulations and the experiments. Firstly, the transition at $We_{crit} = 1.53$ observed by Liu was to a time-periodic state, whereas at the numerically-determined critical value of Smith et al. ($We_{crit} = 1.55$) the calculated three-dimensional structure was steady. Second, whereas the analysis with the Oldroyd B fluid predicted that We_{crit} increased with cylinder separation, Liu saw exactly the opposite trend.

6.1.2 Modification to the wake by polymer additives

There exist very many experimental studies of viscoelastic flow past a cylinder which present measurements, for example, of the heat transfer characteristics (e.g. [73, 74]), of the changes in the drag (e.g. [19, 51, 73, 74, 98, 128]) and of the shift in the streamlines and velocity profiles (e.g. [82, 93, 144]) brought to bear by viscoelasticity. In this subsection, and with a concern for a focussed presentation, however, we nimbly skip over these papers (as well as numerous similarly-minded numerical studies) and concentrate on the question of how the shear instabilities observed in the wake of Newtonian fluids for sufficiently high Reynolds numbers are modified by the addition of small amounts of polymer.

Gadd [51] in 1966 measured the Strouhal number at a Reynolds number of 240 for jets of various fluids flowing past a wire placed transversely to the axis of the jet. A reduction in the shedding frequency relative to that of water was observed when the jet consisted of solutions of polyethylene oxide (PEO). The author used concentrations varying from 5 to 40 wppm. The Strouhal number was also observed to decrease with increasing concentration. No such changes in the shedding frequency were seen, however, in concentrations of polyacrylamide and guar gum that produced the same order of turbulent drag as the 15 wppm concentration PEO solution.

Working with water and a PEO solution at a concentration of 100 wppm past wires of varying diameters and at Reynolds numbers up to almost 400, Kalashnikov and Kudin [77] demonstrated that the vortex shedding frequency was much lower for the polymer solution than for water. The authors were able to attribute the reduction in shedding frequency for any given wire to viscoelasticity since when the same concentration of an *inelastic* solution of PEO was used in the flow around a wire the frequency of the Kármán vortex street was *higher* than for the Newtonian fluid. The same observation was made for a 500 wppm solution of (inelastic) guar gum. Thus, some of the results of Gadd [51] were extended and made more precise. It is also of interest to note from the paper of Kalashnikov and Kudin [77] that the addition of polymer seemed to destabilize the flow in that the Reynolds number Re_{vs} at which the first vortices appeared were less than for the water for all cylinder diameters, the reduction being

greatest for the wires having the smallest diameter. Here, however, it is not possible to claim viscoelasticity as the sole explanation since the same phenomenon was seen with the solutions of inelastic polymer.

Sarpkaya et al. [128] worked with solutions of the same PEO as Gadd [51] and Kalashnikov and Kudin [77], although at different concentrations. Reynolds numbers for the experiments were selected in the range 5×10^4 to 3×10^5 and the general conclusion was that polymer additives precipitated the occurrence of flow characteristics normally seen at higher Reynolds numbers in a Newtonian fluid.

In the experiments of Usui et al. [145], a striking suppression of vortex formation for flow of solutions of PEO at various concentrations ($c = 100, 200$ and 400 wppm) was observed in the flow regime $Re \leq 300$. Consistent with the findings of Kalashnikov and Kudin [77], Usui et al. [145] demonstrated that an increase of polymer concentration or a decrease of cylinder diameter further reduced the Strouhal number at a given Reynolds number. The authors were able to establish a strong correlation between the Strouhal number and a Weissenber number We and equally with the square root of the reciprocal of the elasticity number $E = Re/We$. Although not stated by the authors explicitly it would seem (see their Fig. 3) that Re_{vs} became smaller with increasing concentration and/or decreasing cylinder diameter than the Re_{vs} for a Newtonian flow.

In an experimental investigation of the effect of polymer additives on laminar separation in flow past a cylinder, Kim and Telionis [79] performed experiments at Reynolds numbers of the order of 10^4 with solutions of polyacrylamide and PEO. The results presented for the polyacrylamide solution showed that for the lowest Reynolds numbers ($\approx 10^4$) the Strouhal numbers were slightly lower than for water, in qualitative agreement with Usui et al. [145] (who nevertheless operated at much lower Reynolds numbers). Overall, however, the authors concluded that polymer additives had no effect on the frequency of vortex shedding.

Thus far in our review the polymer solutions used in the experiments have been homogeneous. In two papers [23, 24] dating from 1999 and 2000, however, the authors chose to inject solutions of PEO through holes pierced on the upstream side of the cylinder into the mainstream flow of water. In [23] Cadot and Lebey performed experiments of two-dimensional flow past a cylinder at a Reynolds number of 185 with injection of solutions of polymers having two different molecular weights and at varying flow rates. As the injection rate of the polymer having the greater molecular weight increased the wavelength of the Kármán street also increased and the thickness of the wake decreased. No significant effects were observed by injecting the lower molecular weight polymer, even at the highest injection rate. Thus, although there was a significant difference in the viscosities of the two PEO solutions compared to the water, viscosity gradients alone could not be responsible for the observed effects in the case of the polymer having the greater molecular weight. The authors proposed that the greater elasticity of this latter solution was therefore the main cause of the inhibition effect, in agreement with the linear stability analysis of Azaiez and Homsy [9] who showed using an Oldroyd B model that elasticity tends to stabilize the shear instability in free shear flows. In the later paper, Reynolds numbers up to 300 were realized. Cadot and Kumar [24] confirmed the effect of viscoelasticity in delaying the development of the two-dimensional instability in the sense of shifting it to longer wavelengths. A study of the effect of polymer injection on the three-dimensional instability leading to the A mode showed that in general the A mode was damped and was correlated with changes in the aspect ratio (thickness of the wake divided by wavelength of the Kármán street) of the two-dimensional base flow.

Experiments performed by Cressman et al. [35] with two-dimensional flow of a soap film around a rod at Reynolds numbers of about 400 revealed that whereas a polymer additive of high molecular weight strongly altered vortex shedding, one of lower molecular weight (but higher concentration) had no observable effect. Since the extensional viscosity depends strongly on the molecular weight of a polymer the origin of the dramatic increase in the formation length, reduction in peak shedding frequency and strong suppression of the rms velocity fluctuations observed behind the rod with the addition of the polymer of higher molecular weight was suggested as being due to the elastic extensional properties of the polymer additive.

Very recently, Coelho and Pinho [32, 33] have presented and discussed results of measurements of vortex shedding in the wake of cylinders immersed in aqueous solutions of (weakly elastic) methyl hydroxyethyl cellulose and (more elastic) carboxymethyl cellulose (CMC). The Reynolds numbers selected covered the laminar vortex shedding regime, the transition regime and the shear-layer transition regime. Fluid elasticity was found to reduce a number of critical Reynolds numbers marking the onset or the end of flow regimes. In particular, the critical Reynolds number Re_{vs} for the onset of laminar vortex shedding was found to be lower than for a Newtonian fluid when the CMC solutions were used. The end of the transition regime was seen to be particularly strongly influenced by viscoelasticity. Shear-thinning was found to increase the Strouhal number in the laminar vortex shedding regime, so that non-Newtonian effects on shedding frequency were different from those observed, for example, by Gadd [51] who worked with constant viscosity Boger-type fluids. Pseudoplasticity was thus held partially responsible for the advancement of the onset of the transition regime.

The only recent numerical study known to us of vortex shedding in the wake of a cylinder in a viscoelastic fluid is that of Oliveira [109] who used a constant viscosity modified FENE Chilcott-Rallison (MCR) model to investigate the influence of elasticity, Reynolds number and dumbbell maximum extensibility on the drag, lift and Strouhal number in the two-dimensional laminar vortex shedding regime. Increasing elasticity was found to attenuate the shedding frequency, the rate of decrease of the Strouhal number closely matching that of Usui et al. [145]. The reduction in the time-averaged rms value of the lateral velocity component observed by Cressman et al. [35] were corroborated by Oliveira. The author also found that the formation length increased with Deborah number or polymer extensibility, similar to observations made by Cadot and Lebey [23] and Cadot and Kumar [24]. What seemed rather different from any experimental observations, however, was the prediction (see his Fig. 9a) of a stabilization effect of elasticity on the vortex shedding, Re_{vs} being slightly larger than that for a Newtonian fluid.

The present thesis represents, as far as we are aware, the first linear stability analysis for *inertial* flows of a viscoelastic fluid around a bluff body. Our particular interest is the effect of polymer additives on the linear stability of two-dimensional viscous flow past a confined cylinder and our investigation involves both direct numerical simulation (DNS) and the solution of a generalized eigenvalue problem arising from the linearized perturbation equations. The MCR model is used. We are motivated by two observations:

1. As evidenced earlier in the Introduction, attempts at numerically determining the linear stability and non-linear dynamics of creeping ($Re = 0$) flow past a cylinder have met with only limited success. To date no purely elastic instability ($2D$ or $3D$) in flow past a single confined cylinder has been predicted numerically and agreement with experimentally observed stability thresholds for linear periodic arrays of cylinders has been qualitative at best. A study of the modification to inertial instabilities in dilute polymer solutions

does not suffer from the same handicap of needing to chase what are possibly unachievable Weissenberg number regimes for the single cylinder. Moreover, crude dumbbell models of the FENE-type have already been shown [109] to capture much of the essential physics of the viscoelastic wake dynamics for inertial flows.

2. Despite the encouraging agreement in the laminar vortex shedding regime between numerical and experimental results with the MCR model and solutions of PEO, respectively, for quantities such as shedding frequency, rms lateral velocity magnitude and formation length [24, 23, 35, 109, 145], the numerical prediction (see Fig.9a of [109]) of an increase in Re_{vs} with viscoelasticity is at variance with the experimental evidence, even for constant viscosity fluids. However, the observation was made via direct numerical simulations for only one value of the Deborah number ($De = 80$) and polymer extensibility. A detailed study, involving a linear stability analysis over a range of Deborah numbers and polymer extensibilities, has not yet been done.

The outline of the present chapter is as follows: In Section 6.2 we validate our MCR DNS code by computing a dimensionless drag on a confined cylinder (blockage ratio $\Lambda = 0.5$) as well as the axial elastic normal stress profile on the cylinder surface and in its wake. Results are compared with those of Oliveira [110] in the finitely extensible case and with those of Alves et al. [2] and Fan et al. [43] in the limit of infinitely extensible dumbbells (Oldroyd B fluid). In Sections 6.3 and 6.4 we investigate, via a linear stability analysis and DNS, the effect of Reynolds number, Deborah number and polymer extensibility on the cylinder wake dynamics. Finally, we draw some conclusions.

6.2 Validation and Comparison with Other Results in the Literature

In the present chapter for viscoelastic flow past a confined cylinder the Reynolds number is defined as $Re = \langle u \rangle R / \nu$ where ν is the total kinematic viscosity, $\langle u \rangle$ is the average inlet fluid speed and R is the cylinder radius. Thus our Reynolds number in this chapter should be multiplied by 3 to make them equivalent to those of Willimson [153]. The Weissenberg number We is defined to be equal to $\lambda \langle u \rangle / R$. In the presentation of results in Section 6.4 for laminar vortex shedding, a Strouhal number St is defined by $St = R / (T \langle u \rangle)$, where T is the period of vortex shedding. The solvent to total viscosity ratio β is chosen equal to 0.59 throughout Sections 6.2 to 6.4. We denote by $(\mathbf{x}, t) = ((x_1, x_2), t)$ a dimensionless generic point in space and time.

The velocity-stress formulation described in Section 1.2 is used for the solution of the viscoelastic flow field. The continuity equation (1.30) and the vorticity transport equation (1.31) are applied as in Chapter 5 with the same boundary conditions. In addition, the viscoelastic constitutive equation (1.32) is satisfied within each finite volume in a manner similar to the continuity equation (1.30). To avoid multi-valuedness of the pressure field, and following similar reasoning to that given in Section 5.2, we impose the following equation

$$\oint_{\Gamma} \mathbf{n} \times \left[\frac{\partial \mathbf{u}}{\partial t} + (\nabla \times \mathbf{u}) \times \mathbf{u} + \frac{\beta}{Re} \nabla \times (\nabla \times \mathbf{u}) - \frac{1}{Re} \nabla \cdot \boldsymbol{\tau}' \right] ds = \mathbf{0}, \quad (6.1)$$

M1				M2				M3			
i_{max}	k_{max}	k_{wall}	N	i_{max}	k_{max}	k_{wall}	N	i_{max}	k_{max}	k_{wall}	N
134	271	25	134,830	200	401	37	295,440	266	541	49	527,650

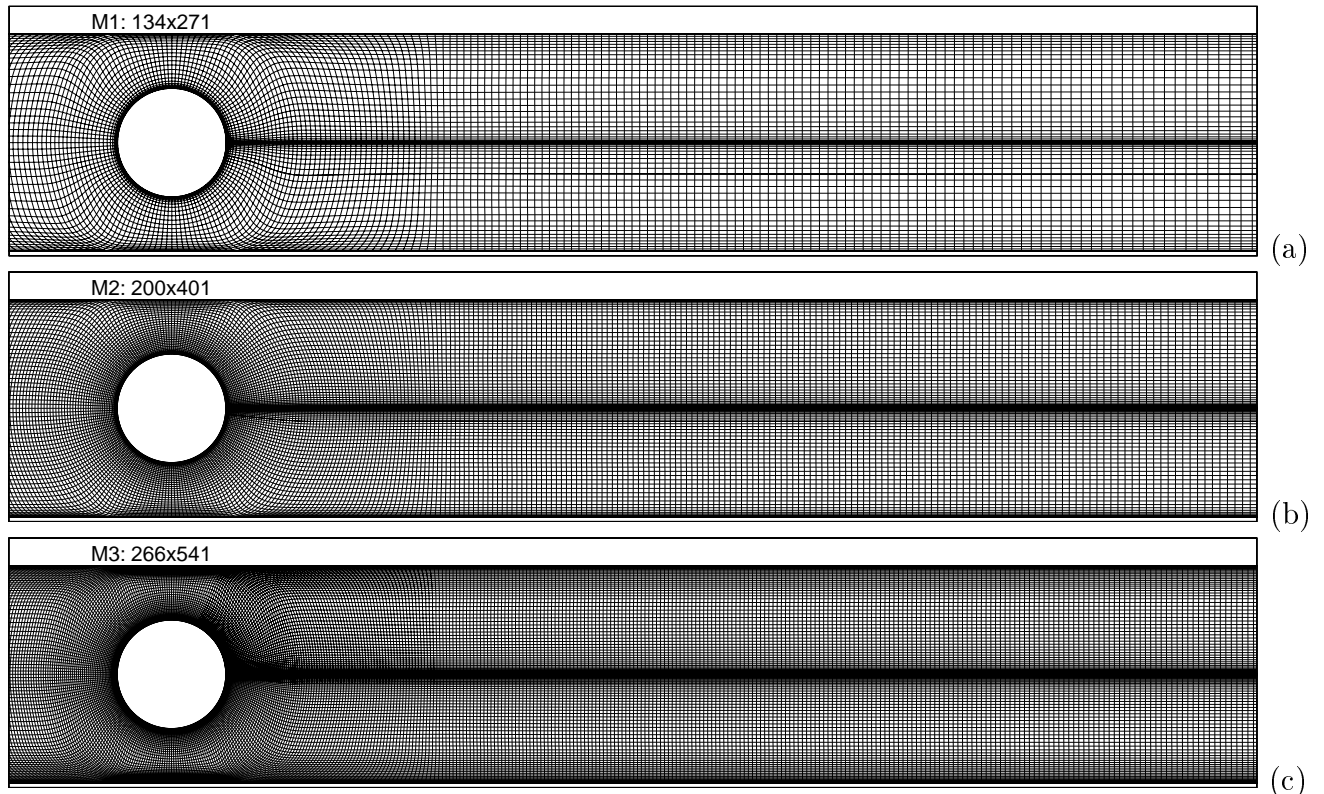
Table 6.1: Values of grid parameters i_{max} , k_{max} , k_{wall} and N .

Figure 6.1: Computational meshes used for blockage ratio $\Lambda = 0.5$. (a) Mesh M1: Number of degrees of freedom = 134,830. (b) Mesh M2: Number of degrees of freedom = 295,440. (c) Mesh M3: Number of degrees of freedom = 527,650.

where, as before, Γ is formed from the union of the outer edges of the finite volumes on the cylinder surface.

Three different finite volume grids (M1-M3) have been used in this chapter. In Fig. 6.1(a)-(c) we show parts of M1 to M3 for blockage ratio $\Lambda = 0.5$. As it may be seen the grid points are highly clustered near the solid wall and in the wake cut in order to solve very strong stress gradients. The inlet and outlet of the channel are set to a distance $80R$ from the cylinder centre. Each of the meshes has been generated algebraically and then smoothed by solving elliptic partial differential equations for the spatial variables x_1 and x_2 where derivatives are with respect to mapped variables in a space in which the mesh appears rectangular [138]. For the present problem the physical grid “cut” is moved away from the line $x_2 = 0$ in order to avoid high stress gradients along this cut. The method of Steger and Sorenson [138] described in Section 5.2 allows both grid cell sizes and grid cell skewness to be controlled at the inner and outer boundaries. Meshes M1 to M3 in Fig. 6.1(a)-(c) are characterized by i_{max} : the number of nodes on the surface of the cylinder, k_{max} : the number of nodes along the line $x_2 = 0$ from the

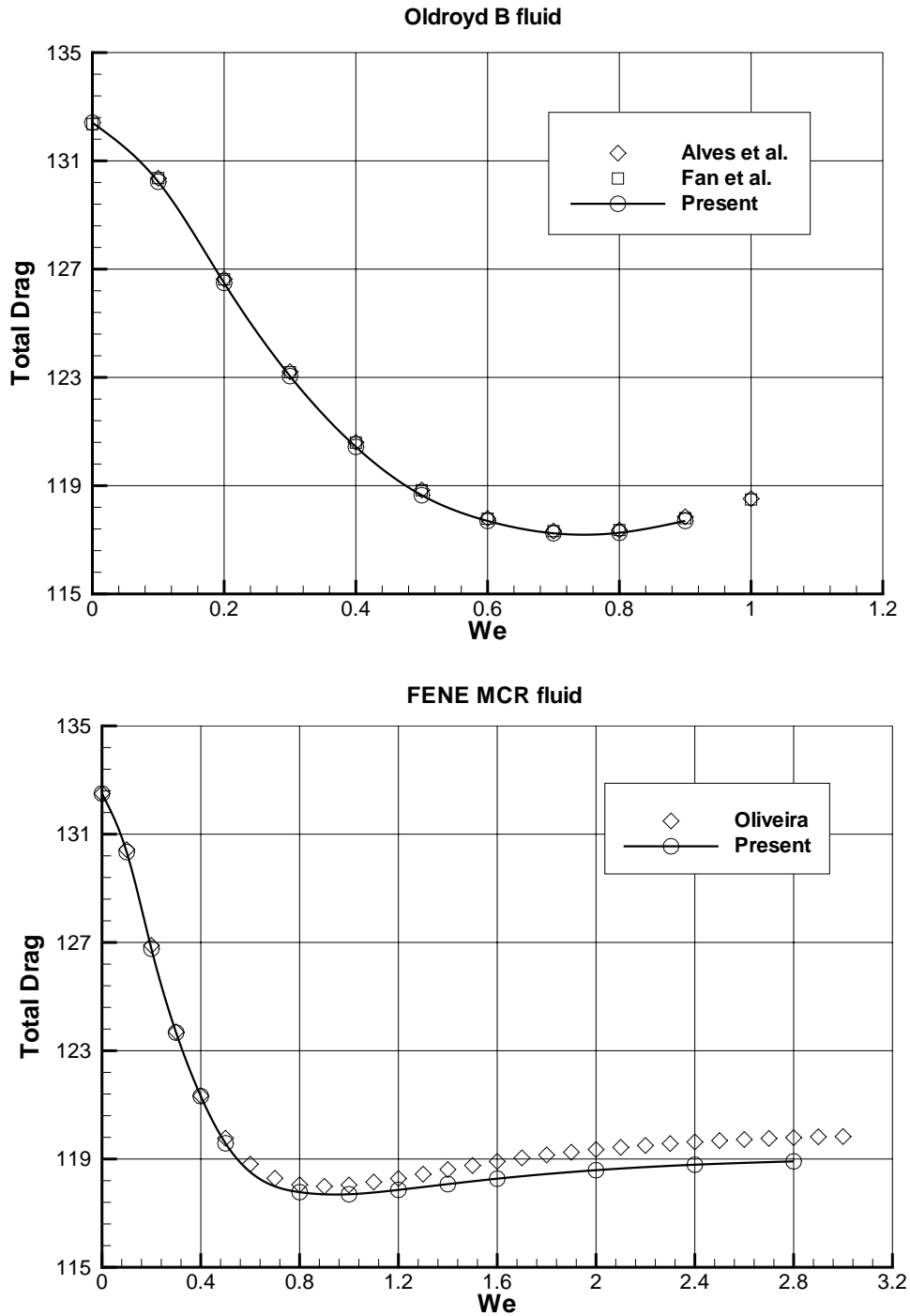


Figure 6.2: Steady state drag at $Re = 0, \beta = 0.59$ computed on mesh M3 as a function of We for Oldroyd B (upper plot) and MCR (lower plot, $b = 144$) fluids. Comparison is made with the results of Alves et al. [2] and Oliveira [110].

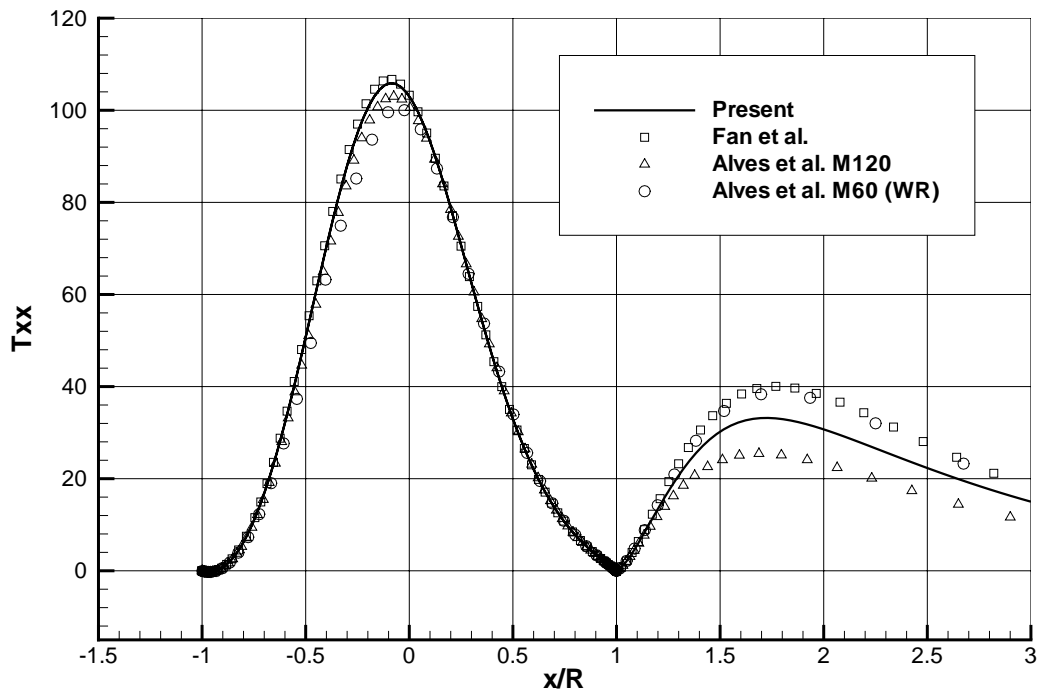


Figure 6.3: Profiles of τ_{xx} on the cylinder surface and in the cylinder wake for an Oldroyd B fluid at $We = 0.7$. Comparison is made with the results of Alves et al. [2] and Fan et al. [43].

rear midpoint on the cylinder to the outflow boundary and k_{wall} : the number of nodes in the gap between the cylinder and a lateral wall. The values of i_{max} , k_{max} and k_{wall} for the three meshes are supplied in Table 6.1 for different blockage ratios. Also shown in Table 6.1 is N , the number of degrees of freedom associated with each mesh.

The computation of the flow of a viscoelastic fluid past a cylinder placed symmetrically between two parallel lateral walls is a popular benchmark problem in the computational rheology community. The flow is a rich mixture of shear and elongational regions and manifests interesting fluid mechanical phenomena in different flow regimes in $We - Re$ space (streamline shifts, drag variations, instabilities etc) some of which will be discussed in Sections 6.3 and 6.4. The necessity of adequately resolving what can be steep elastic stress gradients near solid surfaces and in the cylinder wake results in a potentially challenging problem, all the more so as the Reynolds number and Weissenberg number increase. For a recent review of the numerical literature, the reader is referred to the monograph of Owens and Phillips [112].

Since the majority of numerical results for viscoelastic flow in the cylinder benchmark geometry with $\Lambda = 0.5$ are for steady, inertialess flows, it is natural to validate our basic code in this case. To do so we compare our results against those of Alves et al. [2] and Fan et al. [43, 44] for the Oldroyd B fluid ($b = \infty$) and some newly computed results of Oliveira [110] for the MCR fluid ($b = 144$). Both the results of Alves et al. and Oliveira [110] were obtained using a collocated high-resolution finite volume method and Fan et al. [45, 44] used a Galerkin/least-squares hp finite element method. In Figure 6.2 we show the results of computing the total drag on the cylinder in the two cases of infinite and finite dumbbell extensibility. The results of Alves et al. [2] were obtained using a Richardson extrapolation technique (see Table 3 of [2]) and those of Oliveira using Mesh M45 of [2], the details of which may be found in Table 1

of that paper. Agreement for the Oldroyd B drag results over the whole range of Weissenberg numbers is seen to be very close with our computations. A small discrepancy for $We \gtrsim 0.8$ exists between the MCR drag values computed by Oliveira [110] and us. This is undoubtedly due to the coarse mesh employed by the former. A more discerning measure of the solution accuracy than that supplied by computations of the total drag is consideration of the axial elastic normal stress profile on the cylinder surface and in the cylinder wake. In Figure 6.3 we compare our predictions computed on mesh M3 with those of Alves et al. [2] and Fan et al. [44] for an Oldroyd B fluid at $We = 0.7$. Although the results of Fan et al. [44] were computed using the same SUPG MIX0 formulation as in [45], the authors employed a high-order finite element method featuring uniform interpolation order 10 polynomials in each finite element to represent the velocity and stress fields. The data of Alves et al. represented by triangles in Fig. 6.3 was obtained on their finest mesh M120 (corresponding to 69600 control volumes) and those by diamonds using a special locally wake-refined version of their coarser M60 mesh. Agreement between all results is excellent on the cylinder and in the wake we see that our results lie between those of the fine mesh calculations of Alves et al. and those computed on the highly wake-refined meshes of Fan et al. and Alves et al. Agreement in the wake between our code and what we consider to be the best steady-state codes currently available is therefore quite satisfactory and we could expect even better agreement with further local refinement in the cylinder wake.

6.3 Linear Stability Analysis

6.3.1 Numerical considerations

A representative result of using the Arnoldi method to obtain an approximate eigenvalue set solving the GEVP (2.14) is shown in Fig. 6.4 for the Oldroyd B fluid at the critical Reynolds number ($Re = Re_{vs} = 60$) corresponding to a Weissenberg number of 0.6. The figure shows the result of using the three meshes M1-M3 to compute the steady symmetric base flow (\mathbf{U}, \mathbf{T}). The same Krylov space dimension $m = 150$ was used for these computations. As expected in the case of a zero shift λ the best resolution of the spectrum appears nearest the origin and, in particular, excellent convergence of the leading complex conjugate eigenpair (indicating transition to an unsteady state via a Hopf bifurcation) is apparent. It is clear, however, from Fig. 6.4 that for the computation of the steady base flow using the finest mesh M3, eigenvalues appear in the positive real part of the complex plane. There is no convergence with mesh refinement for these eigenvalues, however, and they are consequently rejected as spurious.

In Table 6.2 we supply the values of the critical Reynolds numbers computed for the Oldroyd B fluid on meshes M1 to M3 with Krylov space dimension $m = 150$. Good convergence of both critical values is to be seen and in fact St_{vs} does not vary between the M2 and M3 results.

6.3.2 Effect on linear stability of polymer additives

The curves of neutral stability for the MCR fluid shown in Fig. 6.5 and the results displayed in Tables 6.2 and 6.3 establish convincingly the case that for this constant viscosity model, polymer additive has a stabilizing effect upon two-dimensional flow past a confined cylinder. This statement is consistent with the observation of Oliveira [109] that in numerical simulations

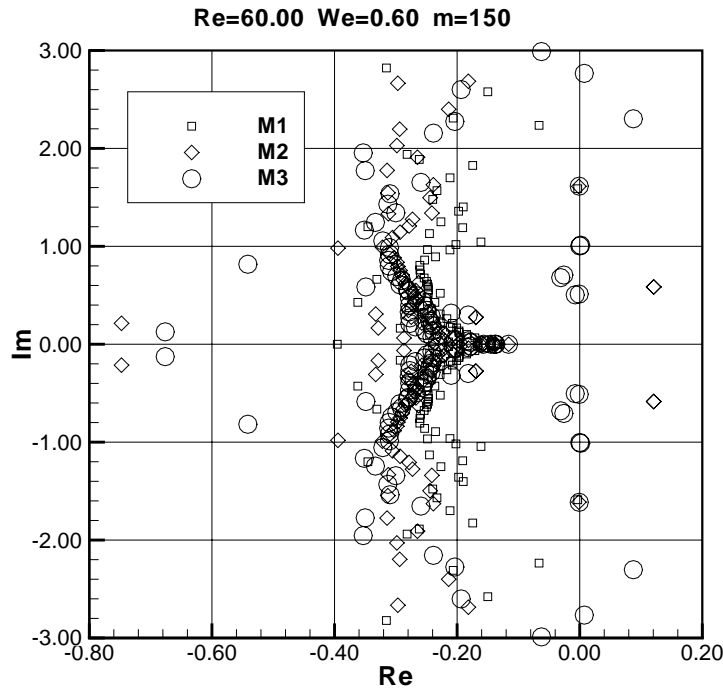


Figure 6.4: Comparison of reciprocal Ritz values computed on meshes M1-M3 with Krylov space dimension $m = 150$ and shift parameter $\lambda = 0.5$. Oldroyd B fluid. $We = 0.6$, $Re = Re_{vs} = 60$. Note the good convergence of the leading physical complex eigenpair on the imaginary axis. Spurious eigenvalues in the positive real part of the complex plane are also in evidence (see commentary in Section 6.3.1).

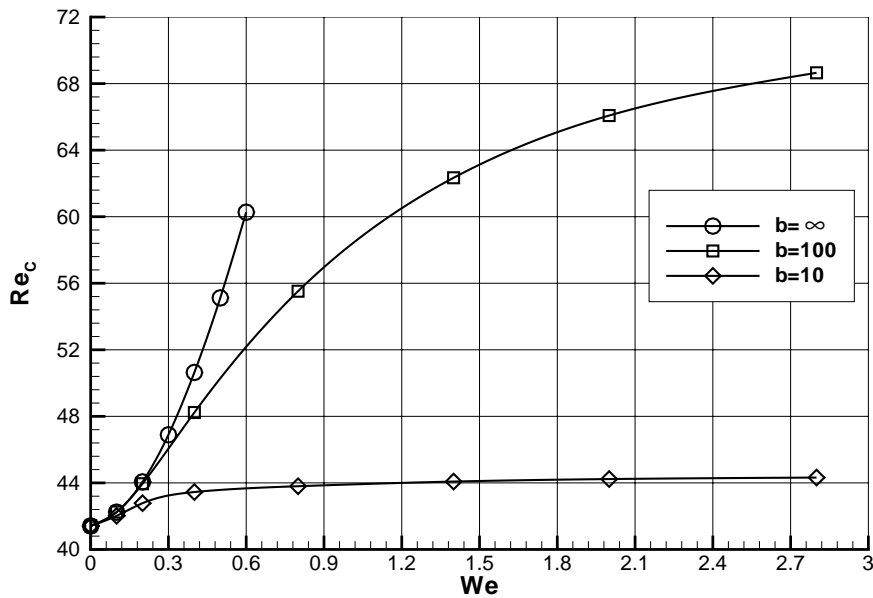


Figure 6.5: Curves of neutral stability for a Hopf bifurcation from the steady two-dimensional symmetric solution for the MCR fluid computed on M2 for $b = 10$, $b = 100$ and $b = \infty$ (Oldroyd B fluid). No increase in the critical Reynolds number from the Newtonian value (41.46) is seen with $b = d = 3$.

	M1		M2		M3	
We	Re_{vs}	St_{vs}	Re_{vs}	St_{vs}	Re_{vs}	St_{vs}
0.0	42.29	0.248	41.41	0.253	41.46	0.253
0.1	43.11	0.247	42.24	0.252	42.37	0.252
0.2	45.01	0.247	44.06	0.252	44.22	0.252
0.3	48.00	0.248	46.89	0.252	47.15	0.252
0.4	51.79	0.249	50.64	0.253	50.83	0.253
0.5	56.05	0.251	55.12	0.255	55.23	0.255
0.6	60.70	0.253	60.27	0.257	60.15	0.257

Table 6.2: Change of critical Reynolds number and Strouhal number with We number. Oldroyd-B fluid

	$b = 100$		$b = 10$	
We	Re_{vs}	St_{vs}	Re_{vs}	St_{vs}
0.0	41.41	0.253	41.41	0.253
0.1	42.25	0.252	42.02	0.252
0.2	43.95	0.252	42.78	0.252
0.4	48.23	0.251	43.43	0.250
0.8	55.52	0.252	43.80	0.248
1.4	62.34	0.252	44.08	0.246
2.0	66.08	0.251	44.23	0.245
2.8	68.65	0.250	44.32	0.243

Table 6.3: Change of critical Reynolds number and Strouhal number with We number. MCR fluid. Mesh M2.

of the unbounded flow of an MCR fluid ($b = 100, De = 80$) around an isolated cylinder, vortex shedding was completely suppressed at $Re = 50$, placing the critical value Re_{vs} for the viscoelastic fluid above that of a Newtonian fluid. Fig. 6.5 reveals that the greater the maximum extensibility of the FENE dumbbells, the larger the value of Re_{vs} for any given value of We . Thus the stabilization brought to bear by the presence of the FENE MCR dumbbells would appear to depend strongly upon the extensional properties of the polymer solution. The recent experimental paper of Cressman et al. [35] confirms the importance of the extensional properties of high molecular weight polymers (even at low concentrations) in reducing the kinetic energy contained in the velocity fluctuations behind a cylinder. In the present case, for which further evidence is presented in Section 6.4, high Trouton ratios lead to strong stabilization of the wake flow relative to the Newtonian case, possibly following the same mechanism as that described by Cressman et al. [35]. For all finite extensibilities b a plateau is reached in the $Re_{vs} - We$ curve, the first critical Reynolds number converging from below with Weissenberg number to some finite limit. Simultaneously, the maximum extensional stress τ_{xx} computed in the flow field converges to a limiting value. As an example, on the last three data points in Fig. 6.5 of the $Re_{vs} - We$ curve corresponding to $b = 10$, τ_{xx} changes from approximately 27.46 at $We = 0.8$ to 28.45 at $We = 1.4$ but only increases up to 28.86 at $We = 2.0$, thus adding weight to our conjecture that it is the extensional properties of the fluid that are the dominant effect in a constant viscosity fluid in the stabilization of the wake flow. From Tables 6.2 and 6.3 no obvious trend is noticeable in the Strouhal number computed along the $Re_{vs} - We$ curves for $b = 10, 100$ or ∞ .

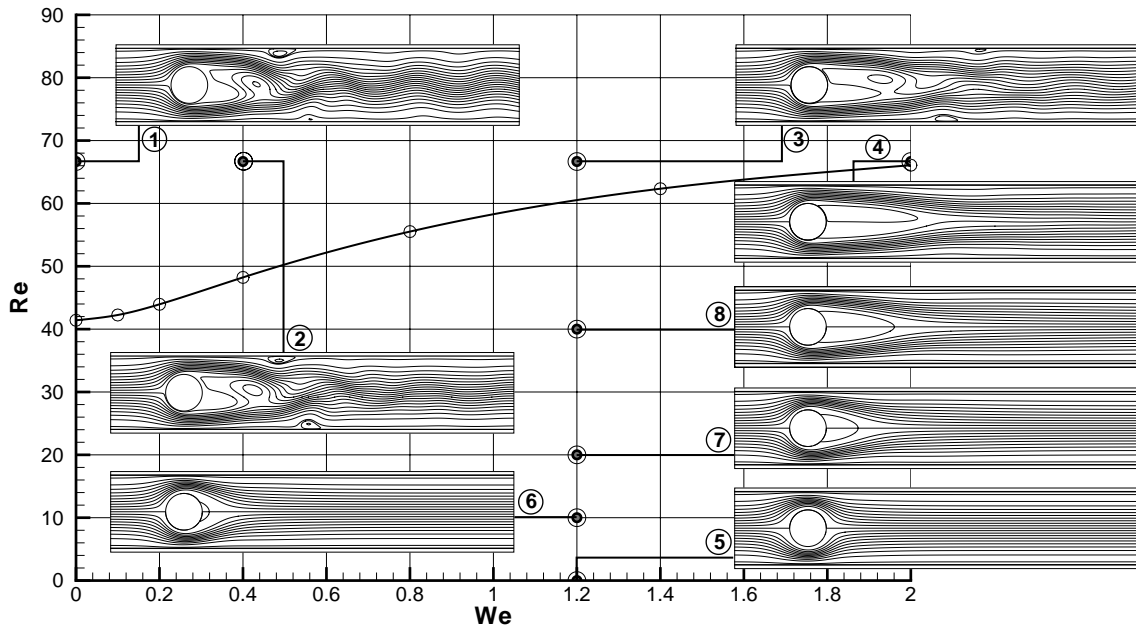


Figure 6.6: Instantaneous streamlines contour plot at eight different points for MCR fluid with $b = 100$.

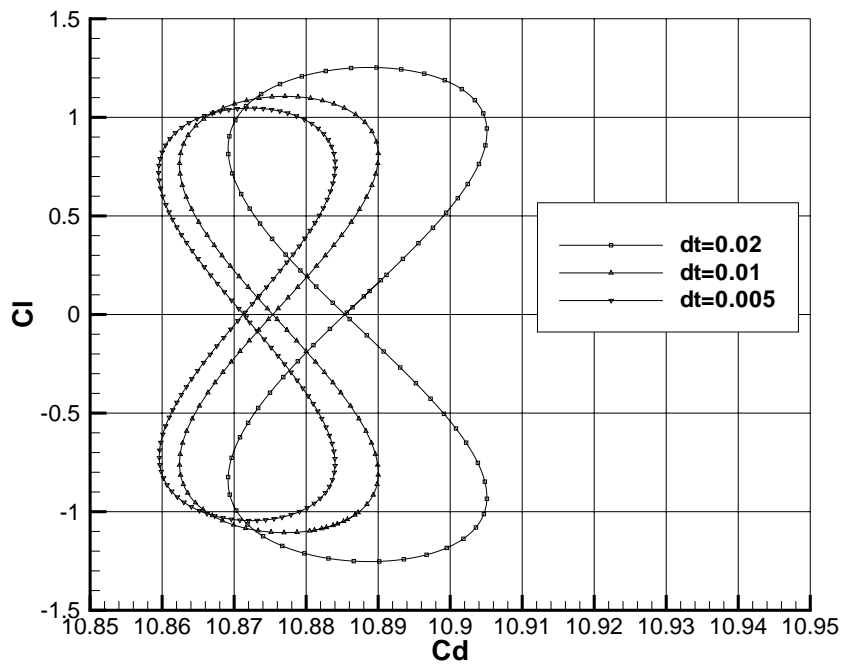


Figure 6.7: Phase-space plot of C_l against C_d at point 1 of Fig. 6.6 using scheme (1.33) and time steps $\Delta t = 0.005, 0.01$ and 0.02 .

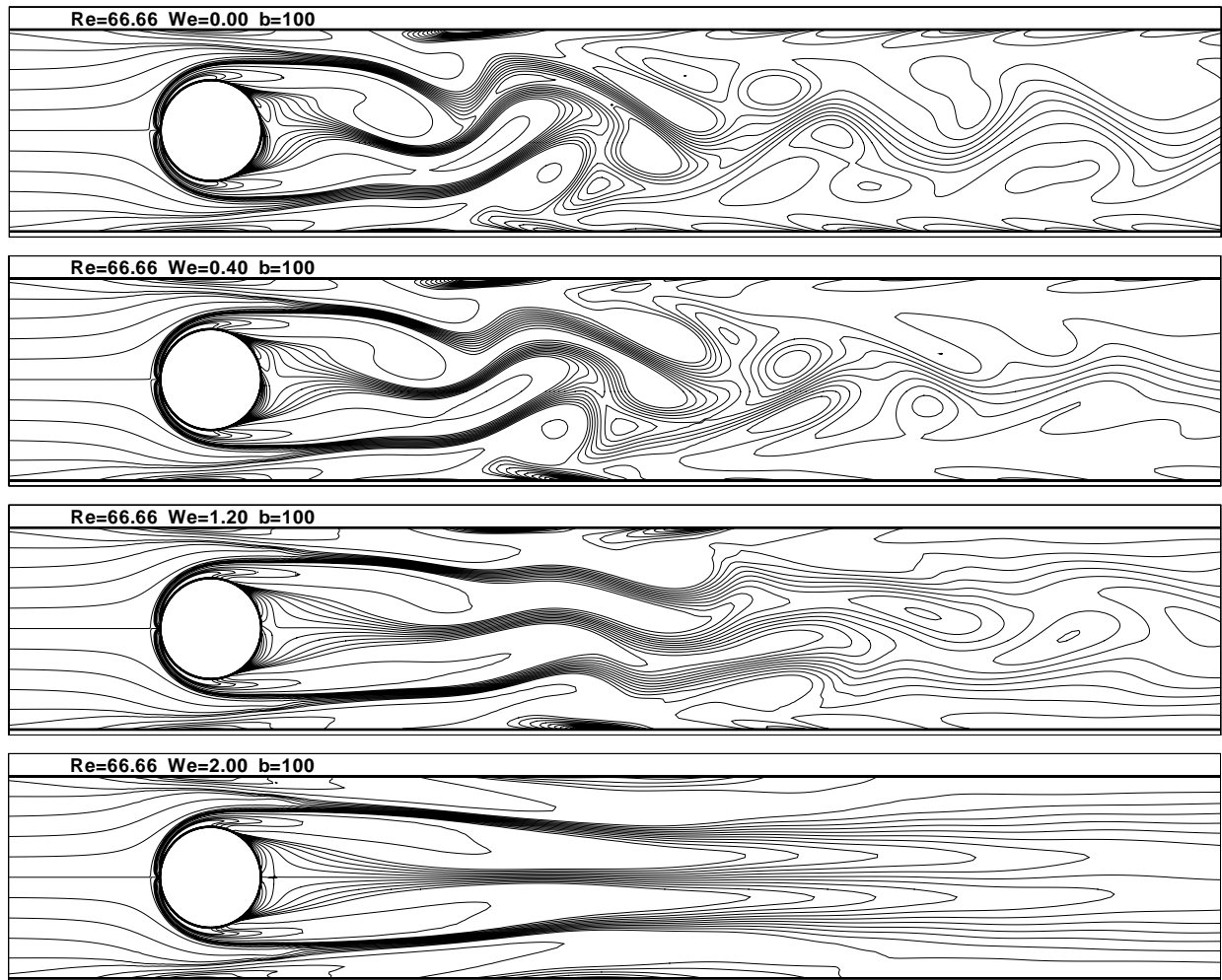


Figure 6.8: Instantaneous vorticity contour plots for MCR fluid at points 1 to 4 in Fig. 6.6. $We = 0.0, 0.4, 1.2$ and 2.0 , $Re = 66.66$, $b = 100$. The plots shown correspond to the minimum lift coefficient.

Two limiting cases of the value of b deserve mention. In the case $b = d = 3$ Eqns. (1.25) and (1.27)-(1.29) make it clear that the fluid is now purely Newtonian with a non-dimensional viscosity equal to unity. This is because (see Eqn. (1.26)) for $b = d$ the maximum extensibility $\langle Q_{max}^2 \rangle^{1/2}$ of a dumbbell equals its equilibrium length $\sqrt{d}l_0$. Thus no stabilization is to be seen. In the case of an Oldroyd B fluid ($b = \infty$) the increasing gradient of the neutral stability curve as a function of We would seem to indicate the existence of a limiting Weissenberg number, at least for two-dimensional flows. The existence of such a limiting Weissenberg number for inertialess flow of an Oldroyd B fluid around confined cylinders and spheres has been conjectured elsewhere [46].

6.4 Direct Numerical Simulations

To gain further insight into the stabilization mechanism of viscoelasticity in a constant viscosity fluid several calculations have been performed for an MCR fluid with $b = 100$. The points in

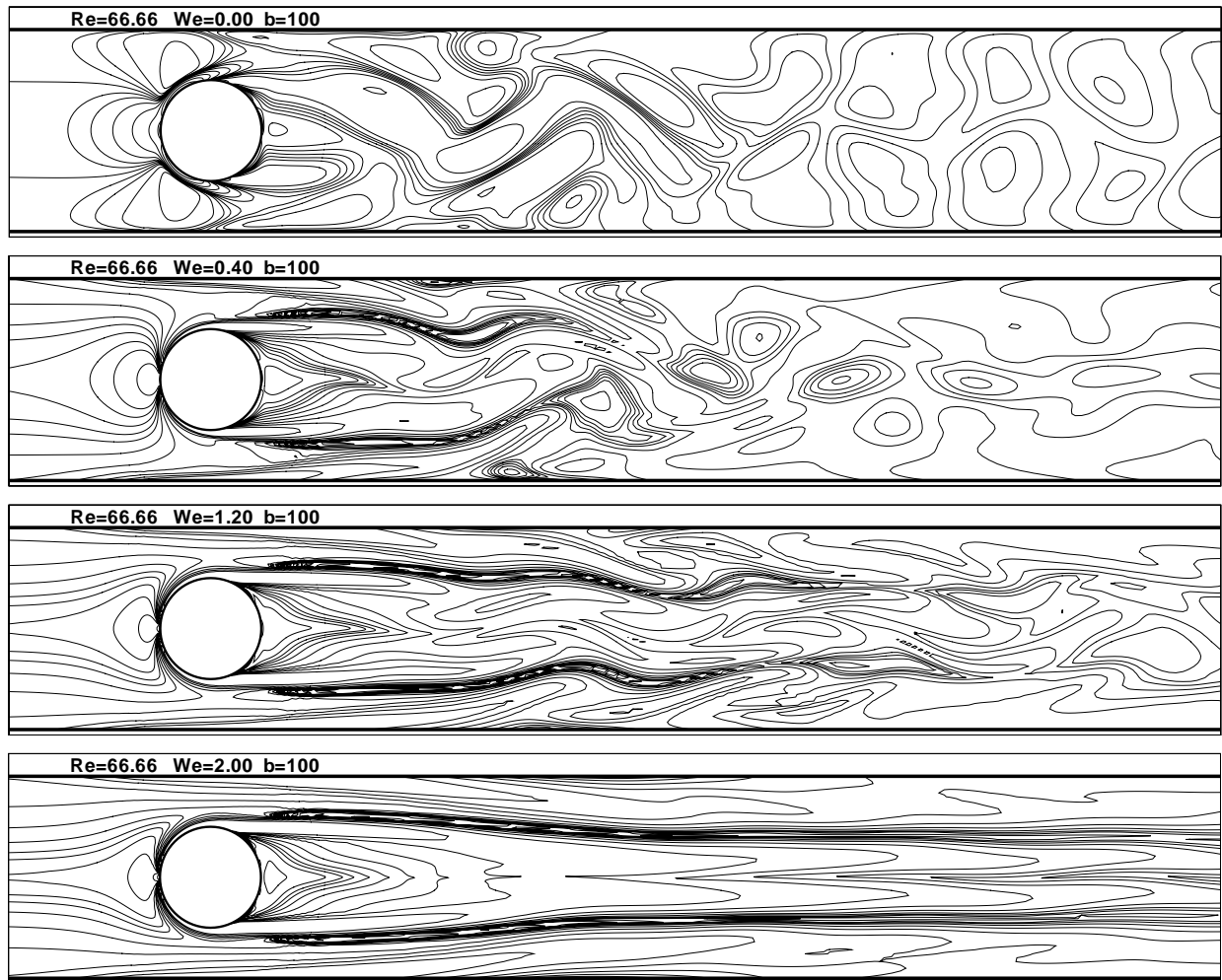


Figure 6.9: Instantaneous τ_{xx} contour plots for MCR fluid at points 1 to 4 in Fig. 6.6. $We = 0.0, 0.4, 1.2$ and 2.0 , $Re = 66.66$, $b = 100$. The plots shown correspond to the minimum lift coefficient.

$We - Re$ parameter space where the computations are performed are labelled 1-8 in Fig. 6.6 and correspond to both steady and unsteady regions in $We - Re$ space. Two numerical tests were performed to give some confidence about the reliability of our unsteady numerical code. These checks were performed at $Re = 66.66$ and $We = 0$ (point 1 of Fig. 6.6). First, in Fig. 6.7 we show the results in a $C_d - C_l$ phase-space plot of varying the dimensionless time step Δt in our Euler implicit scheme (1.33) from 0.02 to 0.005. Good convergence is seen. Computations with $\Delta t = 0.01$ and 0.005 using a Crank-Nicolson scheme could not be distinguished with the naked eye from the corresponding plots in Fig. 6.7. As a compromise between accuracy and cost, $\Delta t = 0.01$ has been used for all results presented in this Section. Secondly, the Strouhal number prediction from the eigenvalue computations of Section 6.3 was compared with that computed from the C_l data of the unsteady code at point 4 in Fig 6.6. The Strouhal number computed from the GEVP ($St = 0.251$) compares very well with the Strouhal number computed from the C_l data at point 4 in Fig 6.6 ($St = 0.252$) even though they are computed at two slightly different Reynolds numbers.

In Figs. 6.8 and 6.9 we show the instantaneous contours (corresponding to the minimum

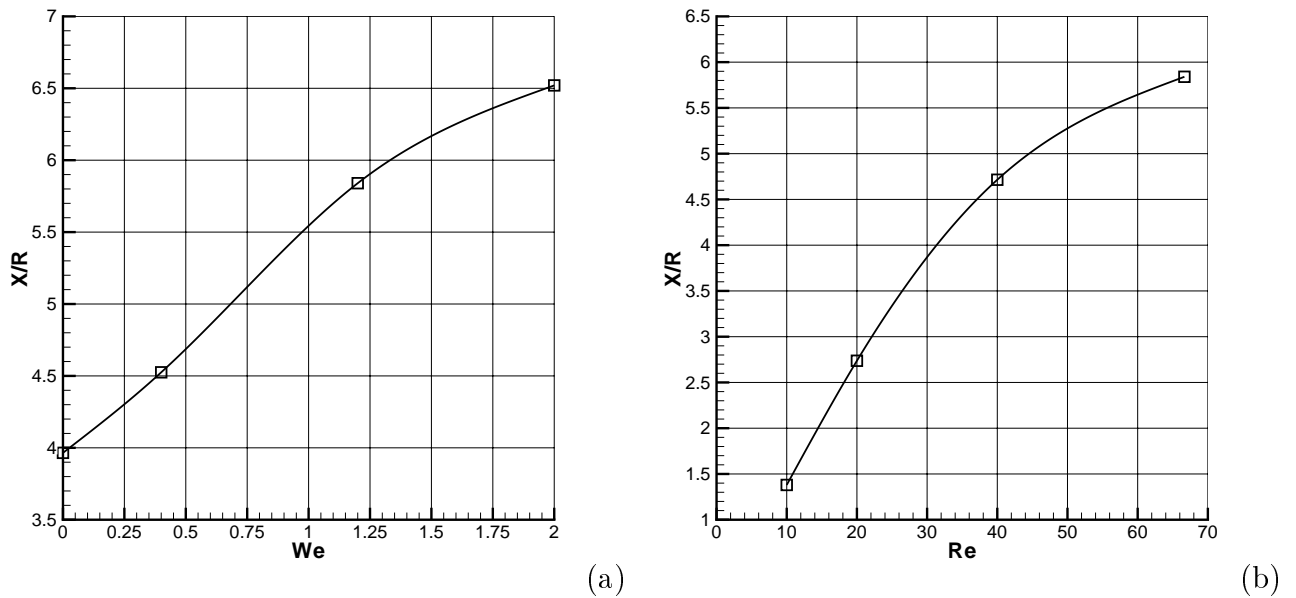
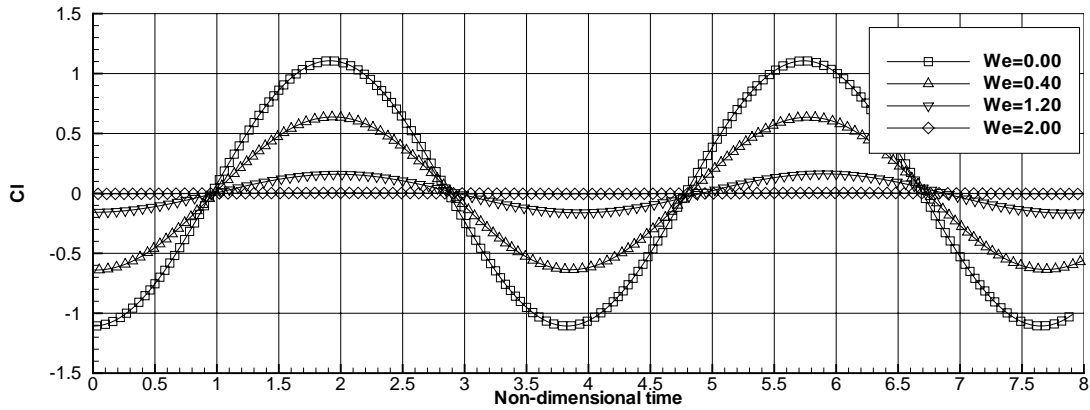


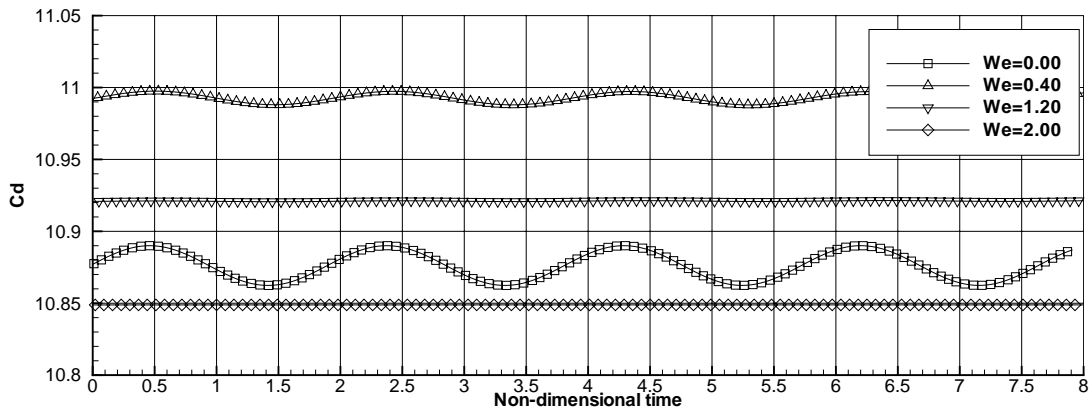
Figure 6.10: Time-averaged length of recirculation region (scaled with cylinder radius) (a) as a function of Weissenberg number $Re = 66.66$, (b) as a function of Reynolds number $We = 1.2$, $b = 100$.

lift coefficient) of the vorticity and axial normal stress τ_{xx} at points 1-4 of Fig. 6.6. At a Weissenberg number of 0.0 and a Reynolds number of 66.66 (point 1 of Fig. 6.6) the flow is unstable to infinitesimal disturbances and becomes time periodic with $St=0.261$. As may be seen from Fig. 6.8 a pair of vortices is shed from the upper and lower gaps between the cylinder and the walls. As these vortices move downstream the vortices having the same sign merge with each other and form a reverse Kármán street. As the Weissenberg number increases the strength of the shed vortices is highly reduced and at a Weissenberg number of 2.0 (point 4 of Fig. 6.6) vortex shedding is almost suppressed. In fact, this is in agreement with our linear stability analysis since point 4 is just above the neutral stability curve.

As elastic effects grow in importance it may be seen in Fig. 6.9 that two parallel strands of highly extended polymer develop, these strands eventually extending from the upstream side of the cylinder and being swept in a tangential direction downstream from its upper and lower surfaces. The peak τ_{xx} value in the two strands progressively increases with increasing Weissenberg number but, as mentioned in the previous Section, increasing the Weissenberg number beyond some critical (b -dependent) value on a curve $Re = Re_{vs}$ does not change the peak τ_{xx} value noticeably since the polymers are now fully extended. For $Re > Re_{vs}$ the two strands of highly extended polymer contain between them a region of slowly moving fluid: the velocity rms values u' and v' along the axis of symmetry in the cylinder wake being lower than in the Newtonian case at the same Reynolds numbers. In Fig. 6.10 (a) we show how the average recirculation length X behind the cylinder at a Reynolds number of 66.66 varies as a function of the Weissenberg number. We note that the recirculatory region increases in length continuously with We . In addition, the strength of the wake vortices has been observed to decrease with increasing elasticity. The instantaneous streamlines shown in Fig. 6.6 show that separation bubbles form on the downstream walls, although their strength is reduced as



(a)



(b)

Figure 6.11: Time variation of (a) lift and (b) drag coefficients. MCR fluid. $We = 0.0, 0.4, 1.2$ and 2.0 , $Re = 66.66$, $b = 100$.

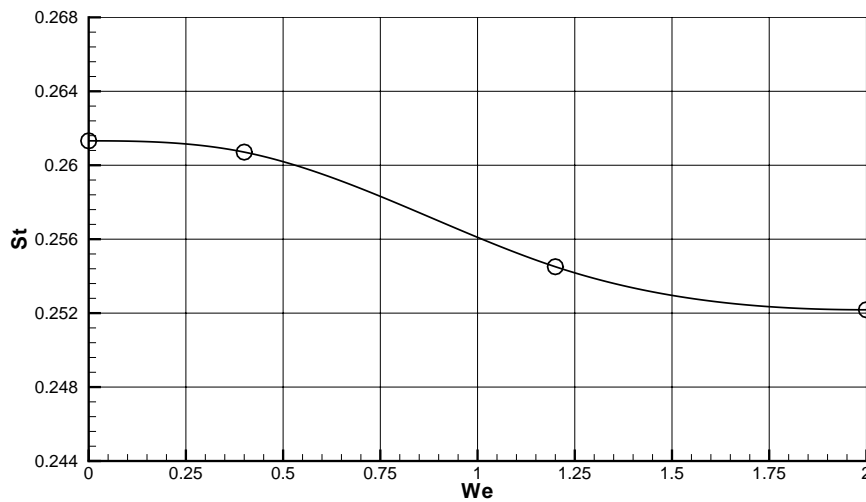


Figure 6.12: Change of Strouhal number with Weissenberg number. MCR fluid. $We = 0.0, 0.4, 1.2$ and 2.0 , $Re = 66.66$, $b = 100$.

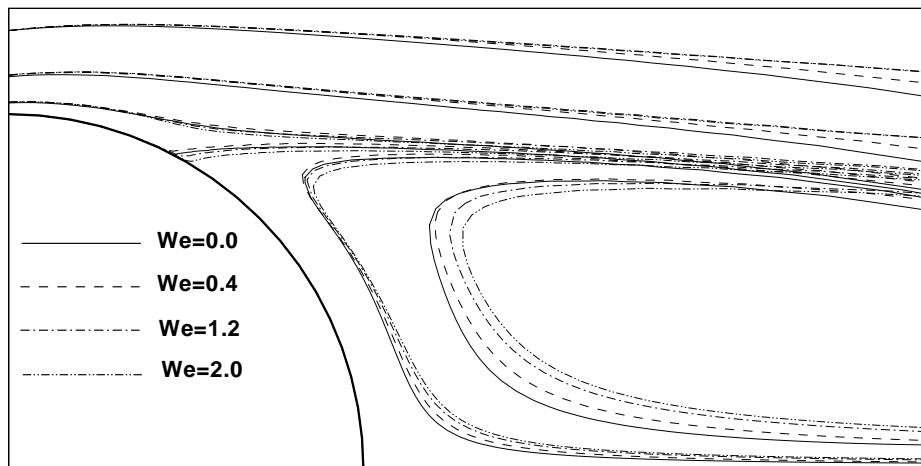


Figure 6.13: Zoom of the time-averaged streamlines at points 1 to 4 of Fig. 6.6 near the downstream side of the cylinder. Note the upstream shift in the streamline at the separation point at $We = 0.4$.

the Weissenberg number increases. When the oscillations are suppressed (just beyond point 4) these separation bubbles completely disappear.

From Figs. 6.11(a) and (b) it may be seen that in moving from points 1 to 4 in Fig. 6.6 the amplitudes of the periodic lift and drag coefficients decrease and the period of the vortex shedding increases as the Weissenberg number increases. The phenomena are indicative of the increasing stabilization of the flow due to viscoelasticity and are manifestations of the fact that as the Weissenberg number increases there develops a long region of slowly moving fluid in the wake of the cylinder entrapped by upper and lower strands of increasingly highly stretched polymer (see the sequences of plots in Figs. 6.8 and 6.9). In Fig. 6.12 we plot the variation of the Strouhal number as a function of Weissenberg number, and this provides a clearer picture than that visible in Fig. 6.11 of how the vortex shedding frequency decreases as the flow restabilizes.

An important point of interest that may be drawn from Fig. 6.11(b) is that there is a slight *increase* in the average drag on the cylinder at small values of We ($\ll 1$) before the time-averaged values begin to decrease again. The steady-state drag was also observed to increase for sufficiently small Weissenberg numbers at $Re = 40$. The same increase for low De , followed by a decrease for larger De was documented by Oliveira [109] for unbounded flow past a single cylinder at $Re = 100$ (see column 4 of his Table 4) but not commented upon. In their study of wall effects on the flow of viscoelastic fluids around a circular cylinder Huang and Feng [71] concluded, however, that there was no increase in drag with elasticity for inertial flow ($0.1 \leq Re \leq 10$) past a confined cylinder at a blockage ratio greater than 0.1 when the Oldroyd B model was used. In our own simulations, no drag increase has been seen for $Re \leq 10$ and the evidence of a monotonic drag decrease in the inertialess case is presented in Fig. 6.2. It would seem, therefore, that for Re sufficiently large an immediate distortion is imparted to the stress field around the cylinder by the polymer that is sufficient to cause an initial drag increase with We . Indeed, we have observed that for very small Weissenberg numbers and sufficiently large Reynolds numbers there is an initial widening of the time-averaged recirculation zone

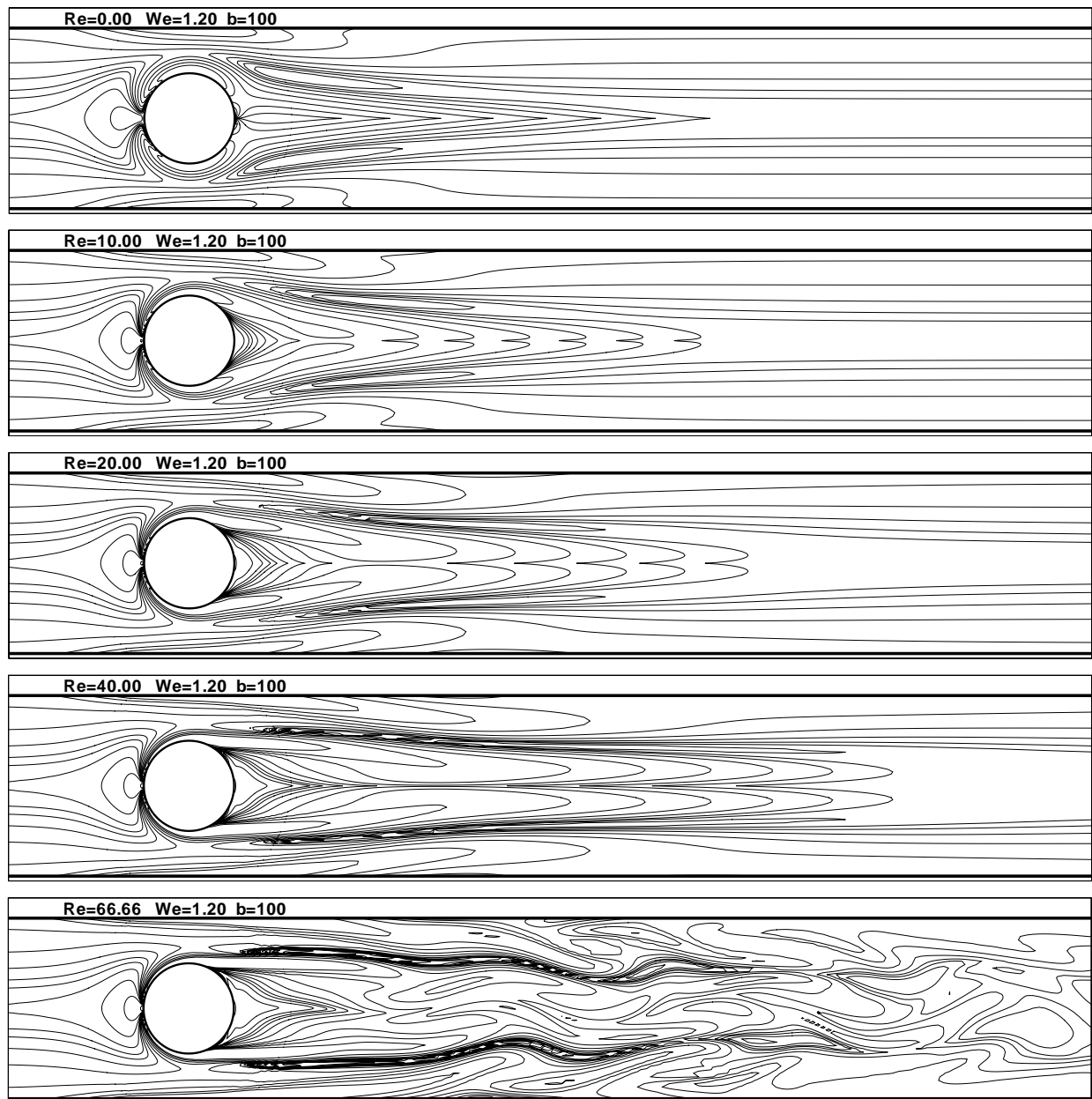


Figure 6.14: τ_{xx} contour plots for MCR fluid at points 5 to 8 and 3 of Fig. 6.6. $Re = 0, 10, 20, 40, 66.66$, $We = 1.2$, $b = 100$. The last contour plot (point 3 of Fig. 6.6) corresponds to the minimum lift coefficient.

compared to the Newtonian case, this being particularly obvious in the movement upstream of the reattachment points on the cylinder: see Fig. 6.13 for an example at $Re = 66.66$. At larger Weissenberg numbers the recirculation zone becomes more slender. For all Weissenberg numbers Fig. 6.13 provides evidence of the continuous *downstream* shift in those streamlines situated sufficiently far from the cylinder.

Finally, although not of immediate relevance to the linear stability results of Section 6.3, it is nevertheless of interest to consider the flow dynamics as the Reynolds number increases at a fixed value of We . In Fig. 6.14 we present changes in τ_{xx} at a Weissenberg number of 1.2 at Reynolds numbers between 0 and 66.66 (see points 3 and 5 to 8 in Fig. 6.6). At $Re = 0$ there is a well-known stress wake behind the cylinder with a very strong stress gradient in the transverse direction. However, as the Reynolds number increases a separation bubble starts to appear just behind the cylinder (see Fig. 6.6) and τ_{xx} becomes almost zero along the axis of symmetry in the cylinder wake. Very high stress strands form from the upper and lower part of the cylinder, as seen in Fig. 6.14. The magnitude of the elastic stresses on the cylinder becomes even higher as the Reynolds number increases further. With increasing Reynolds number the length X of the recirculation zone also increases. This increase is obvious from the streamline plots at points 5 to 8 of Fig. 6.6 and we plot X against Re in Fig. 6.10 (b). As the recirculation length increases the total drag decreases steadily from 117.9 at $Re = 0$ to 14.2 at $Re = 10$, 9.2 at $Re = 20$ and 6.6 at $Re = 40$.

6.5 Conclusions

A linear stability analysis has been performed in order to investigate the effect of elastic forces on the inertial stability of flow of an MCR fluid around a confined circular cylinder. Both direct numerical simulations and linear stability analysis indicate stabilization of the flow by the polymer additives in the sense that the critical Reynolds number for the onset of vortex shedding in the viscoelastic fluid is higher than in the Newtonian case. The stabilization brought to bear by the presence of the MCR dumbbells depends strongly upon the extensional properties of the polymer solution. Direct numerical simulations reveal that in the vortex-shedding regime two strands of highly extended polymer contain between them a region of slowly moving fluid, the amplitude and frequency of vortex shedding in the wake being lower for the viscoelastic fluid than for a Newtonian fluid at the same Reynolds number.

Chapter 7

Conclusions and Future Perspectives

A novel finite volume method based on velocity-only and velocity-stress formulations has been successfully applied to several flow problems. The accuracy of the proposed method has been verified and our results have been compared with the many others available in the literature. The main advantage of the present method lies in the elimination of the pressure term from the governing equations. Therefore any difficulty associated with the pressure term is avoided in a similar manner to that achieved by the velocity-vorticity formulation. However, unlike the velocity-vorticity formulation, our method possesses two significant advantages. First, unlike most velocity-vorticity formulations, no vorticity boundary conditions are required on the wall, since the resulting equations are expressed solely in terms of the velocity components. Only no-slip velocity boundary conditions are required. Secondly, the number of primary variables that need to be determined equals the number of space dimensions.

In addition to our numerical scheme, we have unearthed some interesting fluid physics from our observations which involve both direct numerical simulation (DNS) and the solution of a generalized eigenvalue problem arising from the linearized perturbation equations:

- For purely Newtonian flow past a confined circular cylinder in a channel, four distinct regions in the parameter space have been identified, each corresponding to a different class of flow: (i) steady symmetric flow, (ii) symmetric vortex shedding, (iii) steady asymmetric flow and (iv) asymmetric vortex shedding.
- For viscoelastic flow past a confined circular cylinder, a constant viscosity FENE-type model polymer additive is shown to have a stabilizing effect. In particular, our results reveal that the greater the maximum extensibility of the FENE dumbbells, the larger the value of the critical Reynolds number marking the onset of vortex shedding. The stabilization brought to bear by the dumbbells has been linked to the extensional properties of the FENE fluid.

Although in our current work we investigate two-dimensional temporal and spatial instabilities, one should also verify whether under these flow conditions the base flow is truly two-dimensional (particularly at high blockage ratios). Therefore, three-dimensional linear stability analysis is highly desirable even though it is computationally very expensive. In the case of

purely viscoelastic instabilities, the computation of three-dimensional instabilities to a three-dimensional base flow is an urgent need since the earlier experimental work done by McKinley and co-workers [94] has shown that these instabilities manifest themselves first as a three-dimensional spatial instability followed by a temporal instability.

One of the main problem for three-dimensional numerical simulations is the required computer time for the solution of the resulting algebraic system of equations. Even a frontal direct solver such as the *MUMPS* library is not enough in term of required computer memory to handle three-dimensional problems due to their large size. As an example, a linear system with 2,000,000 equations is solvable on *Eridan* (SGI Origin 3800 parallel machine with 124 processors) for a two-dimensional problem while for a three-dimensional problem we can not afford a linear system larger than 200,000. This particularly due to the increase in the bandwidth of the system which significantly increases the required computer memory. A sample solution of three-dimensional Newtonian flow based on the semi-staggered velocity-pressure formulation of Wright and Smith [135, 154] is presented in Figs. 7.1 and 7.2 at a Reynolds number of 100 ($Re = U_{max}D/\nu$). The solution is obtained by using the *MUMPS* library on a rather coarse grid (with 185,382 degree of freedom). One way to overcome this problem is to use multigrid methods directly [102, 148, 155] or to use one multigrid cycle as a preconditioner for Krylov subspace methods such as GMRES [122], BiCGStab [146], etc. The main advantages of multigrid methods or multigrid preconditioned Krylov subspace methods is that the convergence rate is independent of the grid space and therefore they are scalable on parallel machines. Therefore, we are currently trying to implement these options in a parallel environment.

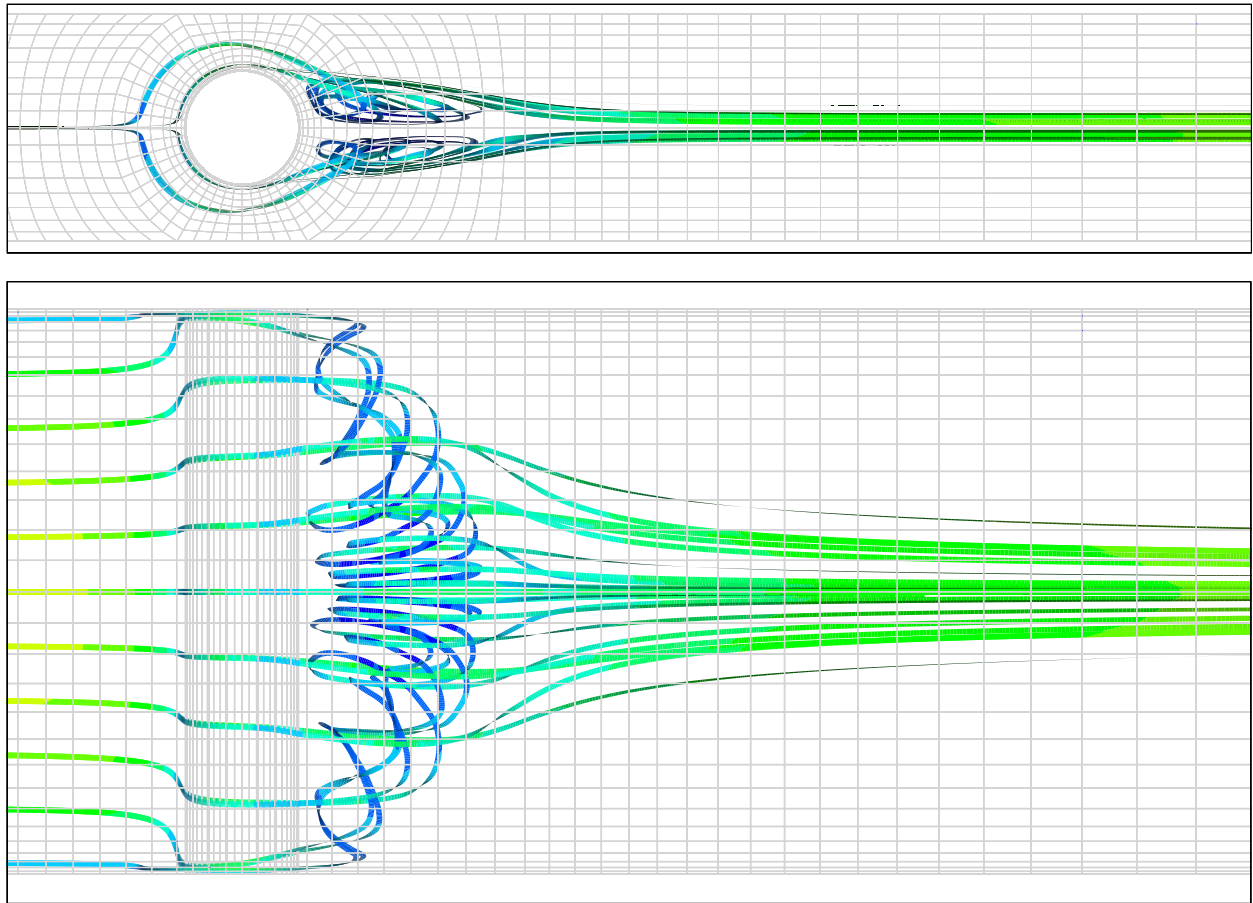


Figure 7.1: Streamtraces for flow past a confined circular cylinder with blockage ratio $D/H=0.50$, aspect ratio $W/H=2.50$ and $Re = 100$.

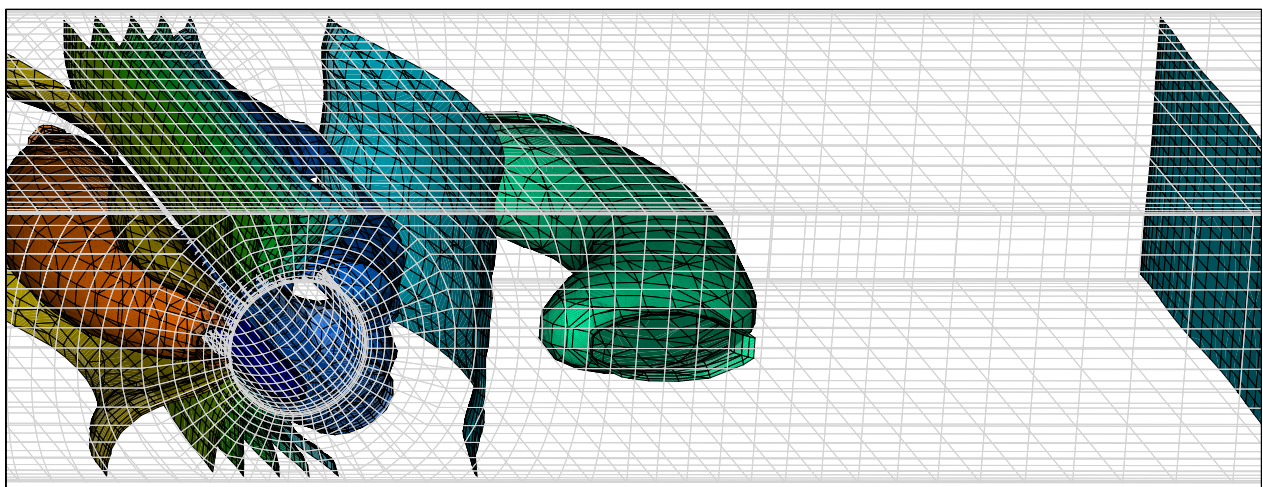


Figure 7.2: Pressure contours for flow past a confined circular cylinder with blockage ratio $D/H=0.50$, aspect ratio $W/H=2.50$ and $Re = 100$.

Bibliography

- [1] A. Allievi and R. Bermejo, Finite element modified method of characteristics for the Navier-Stokes equations, *Int. J. Numer. Meth. Fluids* **32** (2000) 439–464.
- [2] M. A. Alves, F. T. Pinho and P. J. Oliveira, The flow of viscoelastic fluids past a cylinder: finite-volume high-resolution methods, *J. Non-Newtonian Fluid Mech.* **97** (2001) 207–232.
- [3] P. R. Amestoy, I. S. Duff and J. -Y. L'Excellent, Multifrontal parallel distributed symmetric and unsymmetric solvers, *Comput. Methods Appl. Mech. Engrg.* **184** (2000) 501–520.
- [4] P. R. Amestoy, I. S. Duff, J. Koster and J. -Y. L'Excellent, A fully asynchronous multifrontal solver using distributed dynamic scheduling, *SIAM J. Matrix Anal. Appl.* **23** (2001) 15–41.
- [5] P. Anagnostopoulos, G. Iliadis and S. Richardson, Numerical study of the blockage effect on viscous flow past a circular cylinder, *Int. J. Numer. Meth. Fluids* **22** (1996) 1061–1074.
- [6] W. E. Arnoldi, The principle of minimized iterations in the solution of the matrix eigenvalue problem, *Quart. Appl. Math.* **9** (1951) 17–29.
- [7] K. Arora, R. Sureshkumar and B. Khomami, Experimental investigation of purely elastic instabilities in periodic flows, *J. Non-Newtonian Fluid Mech.* **108** (2002) 209–226.
- [8] M. Aydin and R. T. Fenner, Boundary element analysis of driven cavity flow for low and moderate Reynolds numbers, *Int. J. Numer. Meth. Fluids* **37** (2001) 45–64.
- [9] J. Azaiez and G. M. Homsy, Linear stability of free shear-flow of viscoelastic liquids, *J. Fluid Mech.* **268** (1994) 37–69.
- [10] D. Barkley and R. D. Henderson, Three-dimensional Floquet stability analysis of the wake of a circular cylinder, *J. Fluid Mech.* **322** (1996) 215–241.
- [11] E. Barragy and G. F. Carey, Stream function-vorticity driven cavity solution using p finite elements, *Computers & Fluids*, **26** (1997) 453–468.
- [12] A. Batoul, H. Khallouf and G. Labrosse, Une méthode de résolution directe (pseudo-spectrale) du problème de Stokes 2D/3D instationnaire. Application à la cavité entraînée carrée, *C. R. Acad. Sci. Paris* **319** (1994) 1455–1461.
- [13] F. Battaglia, S. J. Taverner, A. K. Kulkarni and C. L. Merkle, Bifurcation of low Reynolds number flows in symmetric channels, *AIAA J.* **35** (1997) 99–105.

- [14] P. W. Bearman and M. M. Zdravkovich, Flow around a circular cylinder near a plane boundary, *J. Fluid Mech.* **89** (1978) 33–47.
- [15] M. Behr, S. Hastreiter, S. Mittal and T. E. Tezduyar, Incompressible flow past a circular cylinder: dependence of the computed flow field on the location of the lateral boundaries, *Comput. Methods Appl. Mech. Engrg.* **123** (1995) 309–316.
- [16] O. Botella, On the solution of the Navier-Stokes equations using Chebyshev projection schemes with third-order accuracy in time, *Computers & Fluids* **26** (1997) 107–116.
- [17] O. Botella and R. Peyret, Benchmark spectral results on the lid-driven cavity flow, *Computers & Fluids* **27** (1998) 421–433.
- [18] O. Botella and R. Peyret, Computing singular solutions of the Navier-Stokes equations with the Chebyshev-collocation method, *Int. J. Numer. Meth. Fluids* **36** (2001) 125–163.
- [19] J. M. Broadbent and B. Mena, Slow flow of an elastico-viscous fluid past cylinders and spheres, *Chem. Eng. J.* **8** (1974) 11–19.
- [20] C-H. Bruneau and C. Jouron, An efficient scheme for solving steady incompressible Navier-Stokes equations, *J. Comput. Phys.* **89** (1990) 389–413.
- [21] O. R. Burggraf, Analytical and numerical studies of the structure of steady separated flows, *J. Fluid Mech.* **24** (1966) 113–151.
- [22] J. A. Byars, Experimental characterization of viscoelastic flow instabilities, *PhD dissertation*, Massachusetts Institute of Technology, Cambridge, MA, USA, (1996).
- [23] O. Cadot and M. Lebey, Shear instability inhibition in a cylinder wake by local injection of a viscoelastic fluid, *Phys. Fluids* **11** (1999) 494–496.
- [24] O. Cadot and S. Kumar, Experimental characterization of viscoelastic effects on two- and three-dimensional shear instabilities, *J. Fluid Mech.* **416** (2000) 151–172.
- [25] W. H. Calhoun and R. L. Roach, A naturally upwinded conservative procedure for the incompressible Navier-Stokes equations on non-staggered grids, *Computers & Fluids* **26** (1997) 525–545.
- [26] W. Cazemier, R. W. C. P. Verstappen and A. E. P. Veldman, Proper orthogonal decomposition and low-dimensional models for driven cavity flows, *Phys. Fluids* **10** (1998) 1685–1699.
- [27] S. Chang and D. C. Haworth, Adaptive grid refinement using cell-level and global imbalances, *Int. J. Numer. Meth. Fluids* **24** (1997) 375–392.
- [28] R. Y. Chang and W. H. Yang, Numerical simulation of mold filling in injection molding using a three-dimensional finite volume approach, *Int. J. Numer. Meth. Fluids* **37** (2001) 125–148.
- [29] J. -H. Chen, W. G. Pritchard and S. J. Tavener, Bifurcation for flow past a cylinder between parallel planes, *J. Fluid Mech.* **284** (1995) 23–41.

-
- [30] M. D. Chilcott and J. M. Rallison, Creeping flow of dilute polymer solutions past cylinders and spheres, *J. Non-Newtonian Fluid Mech.* **29** (1988) 381–432.
- [31] P. J. Coates, R. C. Armstrong and R. A. Brown, Calculation of steady-state viscoelastic flow through axisymmetric contractions with the EEME formulation, *J. Non-Newtonian Fluid Mech.* **42** (1992) 141–188.
- [32] P. M. Coelho and F. T. Pinho, Vortex shedding in cylinder flow of shear-thinning fluids I. Identification and demarcation of flow regimes, *J. Non-Newtonian Fluid Mech.* **110** (2003) 143–176.
- [33] P. M. Coelho and F. T. Pinho, Vortex shedding in cylinder flow of shear-thinning fluids II. Flow characteristics, *J. Non-Newtonian Fluid Mech.* **110** (2003) 177–193.
- [34] M. Coutanceau and R. Bouard, Experimental determination of the main features of the viscous flow in the wake of a circular cylinder in uniform translation. Part 1. Steady flow, *J. Fluid Mech.* **79** (1977) 231–256.
- [35] J. R. Cressman, Q. Bailey and W. I. Goldberg, Modification of a vortex street by a polymer additive, *Phys. Fluids* **13** (2001) 867–871.
- [36] C. Davies and P. W. Carpenter, A novel velocity-vorticity formulation of the Navier-Stokes equations with applications to boundary layer disturbance evolution, *J. Comput. Phys.* **172** (2001) 119–165.
- [37] G. B. Deng, J. Piquet, P. Queutey and M. Visonneau, Incompressible-flow calculations with a consistent physical interpolation finite-volume approach, *Computers & Fluids* **23** (1994) 1029–1047.
- [38] S. C. R. Dennis and G. Z. Chang, Numerical solutions for steady flow past a circular cylinder at Reynolds numbers up to 100, *J. Fluid Mech.* **42** (1970) 471–489.
- [39] Y. Ding and M. Kawahara, Three-dimensional linear stability analysis of incompressible viscous flows using the finite element method, *Int. J. Numer. Meth. Fluids* **31** (1999) 451–479.
- [40] Y. Ding and M. Kawahara, Secondary instabilities of wakes of a circular cylinder using a finite element method, *Int. J. Comp. Fluid Dynamics* **13** (2000) 279–301.
- [41] D. Drikakis, Bifurcation phenomena in incompressible sudden expansion flows, *Phys. Fluids* **9** (1997) 76–86.
- [42] J. Dušek, P. Le Gal and P. Fraunié, A numerical and theoretical study of the first Hopf bifurcation in a cylinder wake, *J. Fluid Mech.* **264** (1994) 59–80.
- [43] Y. R. Fan, R. I. Tanner and N. Phan-Thien, Galerkin/least-square finite element methods for steady viscoelastic flows, *J. Non-Newtonian Fluid Mech.* **84** (1999) 233–256.
- [44] Y. R. Fan, Private communication, (2004).

-
- [45] Y. R. Fan, R. I. Tanner and N. Phan-Thien, Galerkin/least-square finite element methods for steady viscoelastic flows, *J. Non-Newtonian Fluid Mech.* **84** (1999) 233–256.
- [46] Y. R. Fan, Limiting behavior of the solutions of a falling sphere in a tube filled with viscoelastic fluids, *J. Non-Newtonian Fluid Mech.* **110** (2003) 77–102.
- [47] O. H. Faxén, Forces exerted on a rigid cylinder in a viscous fluid between two parallel fixed planes, *Proc. R. Swed. Acad. Eng. Sci.* **187** (1946) 1–13.
- [48] R. M. Fearn, T. Mullin and K. A. Cliffe, Nonlinear flow phenomena in a symmetric sudden expansion, *J. Fluid Mech.* **211** (1990) 595–608.
- [49] B. Fornberg, A numerical study of steady viscous flow past a circular cylinder, *J. Fluid Mech.* **98** (1980) 819–855.
- [50] A. Fortin, M. Jardak, J. J. Gervais and R. Pierre, Localization of Hopf bifurcations in fluid flow problems, *Int. J. Numer. Meth. Fluids* **24** (1997) 1185–1210.
- [51] G. E. Gadd, Effects of long-chain molecule additives in water on vortex streets, *Nature* **211** (1966) 169–170.
- [52] T. B. Gatski, Review of incompressible fluid flow computations using the vorticity-velocity formulation, *Appl. Numer. Math.* **7** (1991) 227–239.
- [53] T. B. Gatski and C. E. Grosch, In 9th Conference on Numerical Methods in Fluid Dynamics, Edited by S. J. P. Boujot, *Lecture Notes in Physics*, **218**, (1984) 235–239.
- [54] T. B. Gatski, C. E. Grosch and M. E. Rose, A numerical study of the two-dimensional Navier-Stokes equations in vorticity-velocity variables, *J. Comput. Phys.* **48** (1982) 1–22.
- [55] J. H. Gerrard, The wakes of cylindrical bluff bodies at low Reynolds numbers, *Philos. Trans. R. Soc. London Ser. A* **288** (1978) 351–382.
- [56] J. J. Gervais, D. Lemelin and R. Pierre, Some experiments with stability analysis of discrete incompressible flows in the lid-driven cavity, *Int. J. Numer. Meth. Fluids* **24** (1997) 477–492.
- [57] U. Ghia, K. N. Ghia and C. T. Shin, High-Re solutions for incompressible flow using the Navier-Stokes equations and a multigrid method, *J. Comput. Phys.* **48** (1982) 387–411.
- [58] J. W. Goodrich, K. Gustafson and K. Halasi, Hopf bifurcation in the driven cavity, *J. Comput. Phys.* **90** (1990) 219–261.
- [59] P. M. Gresho, Incompressible fluid dynamics: Some fundamental formulation issues, *Annu. Rev. Fluid Mech.* **23** (1991) 413–453.
- [60] M. M. Grigoriev and G. F. Dargush, A poly-region boundary element method for incompressible viscous fluid flows, *Int. J. Numer. Meth. Engrg.* **46** (1999) 1127–1158.
- [61] M. M. Grigoriev and A. V. Fafurin, A boundary element method for steady viscous fluid flow using penalty function formulation, *Int. J. Numer. Meth. Fluids* **25** (1997) 907–929.

- [62] D. X. Guo, A second order scheme for the Navier-Stokes equations: Application to the driven-cavity problem, *Appl. Numer. Math.* **35** (2000) 307–322.
- [63] K. Gustafson and K. Halasi, Vortex dynamics of cavity flows, *J. Comput. Phys.* **64** (1986) 279–319.
- [64] K. Gustafson and K. Halasi, Cavity flow dynamics at higher Reynolds number and higher aspect ratio, *J. Comput. Phys.* **70** (1987) 271–283.
- [65] M. Hafez and M. Soliman, Numerical solution of the incompressible Navier-Stokes equations in primitive variables on unstaggered grids, *Incompressible Computational Fluid Dynamics*, M. D. Gunzberger and R. A. Nicolaides (eds), Cambridge University Press, (1993) 183–201.
- [66] E. B. Hansen and M. A. Kelmanson, An integral equation justification of the boundary conditions of the driven cavity problem, *Computers & Fluids* **23** (1994) 225–240.
- [67] T. Hawa and Z. Rusak, The dynamics of a laminar flow in a symmetric channel with a sudden expansion, *J. Fluid Mech.* **436** (2001) 283–320.
- [68] R. D. Henderson, Detail of the drag curve near the onset of vortex shedding, *Phys. Fluids* **7** (1995) 2102–2104.
- [69] R. D. Henderson, Dynamic refinement algorithms for spectral element methods, *Comput. Methods Appl. Mech. Engrg.* **175** (1999) 395–411.
- [70] S. Hou, Q. Zou, S. Chen, G. Doolen and A. C. Cogley, Simulation of cavity flow by the lattice Boltzmann method, *J. Comput. Phys.* **118** (1995) 329–347.
- [71] P. Y. Huang and J. Feng, Wall effects on the flow of viscoelastic fluids around a circular cylinder, *J. Non-Newtonian Fluid Mech.* **60** (1995) 179–198.
- [72] C. P. Jackson, A finite-element study of the onset of vortex shedding in flow past variously shaped bodies, *J. Fluid Mech.* **182** (1987) 23–45.
- [73] D. F. James and A. J. Acosta, The laminar flow of dilute polymer solutions around circular cylinders, *J. Fluid Mech.* **42** (1970) 269–288.
- [74] D. F. James and O. P. Gupta, Drag on circular cylinders in dilute polymer solutions, *Chem. Eng. Prog. Symp. Ser.* **67** (1971) 62–73.
- [75] A. Jennings, *Matrix Computation for Engineers and Scientists*, Wiley, London (1977).
- [76] G. Jin and M. Braza, A nonreflecting outlet boundary condition for incompressible unsteady Navier-Stokes calculations, *J. Comput. Phys.* **107** (1993) 239–253.
- [77] V. N. Kalashnikov and A. M. Kudin, Karman vortices in the flow of drag-reducing polymer solutions, *Nature* **225** (1970) 445–446.
- [78] G. E. Karniadakis and G. S. Triantafyllou, Three-dimensional dynamics and transition to turbulence in the wake of bluff objects, *J. Fluid Mech.* **238** (1992) 1–30.

- [79] B. K. Kim and D. P. Telionis, The effect of polymer additives on laminar separation, *Phys. Fluids A* **1** (1989) 267–273.
- [80] P. Kjellgren, A semi-implicit fractional step finite element method for viscous incompressible flows, *Comput. Mech.* **20** (1997) 541–550.
- [81] D. A. Knoll and P. R. McHugh, Enhanced nonlinear iterative techniques applied to a nonequilibrium plasma flow, *SIAM J. Sci. Comput.* **19** (1998) 291–301.
- [82] A. Koniuta, P. M. Adler and J.-M. Piau, Flow of dilute polymer solutions around circular cylinders, *J. Non-Newtonian Fluid Mech.* **7** (1980) 101–106.
- [83] A. Kourta, M. Braza, P. Chassaing and H. Haminh, Numerical analysis of a natural and excited two-dimensional mixing layer, *AIAA J.* **25** (1987) 279–286.
- [84] R. Kupferman, A central-difference scheme for a pure stream function formulation of incompressible viscous flow, *SIAM J. Sci. Comput.* **23** (2001) 1–18.
- [85] C. Lei, L. Cheng and K. Kavanagh, Re-examination of the effect of a plane boundary on force and vortex shedding of a circular cylinder, *J. Wind. Eng. Ind. Aerodyn.* **80** (1999) 263–286.
- [86] C. Lei, L. Cheng and K. Kavanagh, Spanwise length effects on three-dimensional modelling of flow over a circular cylinder, *Comput. Methods Appl. Mech. Engrg.* **190** (2001) 2909–2923.
- [87] B. P. Leonard, Stable and accurate convective modeling procedure based on quadratic upstream interpolation, *Comp. Meth. Appl. Mech. Engrg.* **19** (1979) 59–98.
- [88] E. Leriche and M. O. Deville, A Uzawa-type pressure solver for the Lanczos- τ -Chebyshev spectral method, *Computers & Fluids* (2001) submitted.
- [89] A. W. Liu, Viscoelastic flow of polymer solutions around arrays of cylinders: comparison of experiment and theory, *PhD dissertation*, Massachusetts Institute of Technology, Cambridge, MA, USA, (1997).
- [90] A. W. Liu, D. E. Bornside, R. C. Armstrong and R. A. Brown, Viscoelastic flow of polymer solutions around a periodic, linear array of cylinders: comparisons of predictions for microstructure and flow fields, *J. Non-Newtonian Fluid Mech.* **77** (1998) 153–190.
- [91] C. H. Liu and D. Y. C. Leung, Development of a finite element solution for the unsteady Navier-Stokes equations using projection method and fractional- θ -scheme, *Comput. Meth. Appl. Mech. Engrg.* **190** (2001) 4301–4317.
- [92] N. Mai-Duy and T. Tran-Cong, Numerical solution of Navier-Stokes equations using multiquadric radial basis function networks, *Int. J. Numer. Meth. Fluids* **37** (2001) 65–86.
- [93] O. Manero and B. Mena, On the flow of viscoelastic liquids past a circular cylinder, *J. Non-Newtonian Fluid Mech.* **9** (1981) 379–387.

- [94] G. McKinley, R. C. Armstrong and R. C. Brown, The wake instability in viscoelastic flow past confined circular cylinders, *Phil. Trans. R. Soc. Lond. A* **344** (1993) 265–304.
- [95] G. H. McKinley, P. Pakdel and A. Öztekin, Rheological and geometric scaling of purely elastic flow instabilities, *J. Non-Newtonian Fluid Mech.* **67** (1996) 19–47.
- [96] A. Meister, Comparison of different Krylov subspace methods embedded in an implicit finite volume scheme for the computation of viscous and inviscid flow fields on unstructured grids, *J. Comp. Phys.* **140** (1998) 311–345.
- [97] A. Meister and M. Oevermann, An implicit finite volume approach of the k - ε turbulence model on unstructured grids, *ZAMM* **78** (1998) 743–757.
- [98] B. Mena and B. Caswell, Slow flow of an elastic-viscous fluid past an immersed body, *Chem. Eng. J.* **8** (1974) 125–134.
- [99] C. Migeon, A. Texier, and G. Pineau, Effects of lid-driven cavity shape on the flow establishment phase, *J. Fluids & Structures*, **14** (2000) 469–488.
- [100] S. Mishra and K. Jayaraman, Asymmetric flows in planar symmetric channels with large expansion ratio, *Int. J. Numer. Meth. Fluids* **38** (2002) 945–962.
- [101] H. K. Moffatt, Viscous and resistive eddies near a sharp corner, *J. Fluid Mech.* **18** (1964) 1–18.
- [102] R. S. Montero, I. M. Llorente and M. D. Salas, Robust multigrid algorithms for the Navier-Stokes equations, *J. Comp. Phys.* **173** (2001) 412–432.
- [103] K. W. Morton and M. Stynes, An analysis of the cell vertex method, *RAIRO - Modél. Math. Anal. Numér.* **28** (1994) 699–724.
- [104] K. W. Morton, M. Stynes and E. Suli, Analysis of a cell-vertex finite volume method for convection-diffusion problems, *Math. Comp.* **66** (1997) 1389–1406.
- [105] R. Natarajan, An Arnoldi-based iterative scheme for nonsymmetric matrix pencils arising in finite element stability problems, *J. Comput. Phys.* **100** (1992) 128–142.
- [106] M. Nishioka and H. Sato, Measurements of velocity distributions in the wake of a circular cylinder at low Reynolds numbers, *J. Fluid Mech.* **65** (1974) 97–112.
- [107] M. Nishioka and H. Sato, Mechanism of determination of shedding frequency of vortices behind a cylinder at low Reynolds numbers, *J. Fluid Mech.* **89** (1978) 49–60.
- [108] B. R. Noack and H. Eckelmann, A global stability analysis of the steady and periodic cylinder wake, *J. Fluid Mech.* **1994** (1994) 297–330.
- [109] P. J. Oliveira, Method for time-dependent simulations of viscoelastic flows: vortex shedding behind cylinder, *J. Non-Newtonian Fluid Mech.* **101** (2001) 113–137.
- [110] P. J. Oliveira, Asymmetric flows of viscoelastic fluids in symmetric planar expansion geometries. *J. Non-Newtonian Fluid Mech.* **114** (2003) 33–63.

-
- [111] P. J. Oliveira, Private communication, (2003).
- [112] R. G. Owens and T. N. Phillips, *Computational Rheology*, Imperial College Press/World Scientific, London, (2002).
- [113] P. Pakdel and G. H. McKinley, Elastic instability and curved streamlines, *Phys. Rev. Lett.* **77** (1996) 2459–2462.
- [114] T. W. Pan and R. Glowinski, A projection/wave-like equation method for the numerical simulation of incompressible viscous fluid flow modeled by the Navier-Stokes equations, *Comput. Fluid Dyn. J.* **9** (2000) 28–42.
- [115] M. Poliashenko and C. K. Aidun, A direct method for computation of simple bifurcations, *J. Comput. Phys.* **121** (1995) 246–260.
- [116] O. Posdziech and R. Grundmann, Numerical simulation of the flow around an infinitely long circular cylinder in the transition regime, *Theoret. Comput. Fluid Dynamics* **15** (2001) 121–141.
- [117] C. Pozrikidis, Numerical studies of cusp formation at fluid interfaces in Stokes flow, *J. Fluid Mech.* **357** (1998) 29–57.
- [118] C. Pozrikidis, Numerical investigation of the effect of surfactants on the stability and rheology of emulsions and foam, *J. Engrg. Math.* **41** (2001) 237–258.
- [119] M. Provansal, C. Mathis and L. Boyer, Bénard-von Kármán instability: transient and forced regimes, *J. Fluid Mech.* **182** (1987) 1–22.
- [120] A. Roshko, On the development of turbulent wakes from vortex streets, *NACA Report* 1191 (1954).
- [121] Y. Saad, Variations on Arnoldi’s method for computing eigenelements of large unsymmetric matrices, *Linear Algebra Appl.* **34** (1980) 269–295.
- [122] Y. Saad and M. H. Schultz, GMRES: a generalized minimal residual algorithm for solving nonsymmetric linear systems, *SIAM J. Sci. Statist. Comput.* **7** (1986) 856–869.
- [123] M. Sahin, Solution of the incompressible unsteady Navier-Stokes equations only in terms of the velocity components, *Int. J. Comp. Fluid Dynamics* **17** (2003) 199–203.
- [124] M. Sahin and R. G. Owens, A novel fully-implicit finite volume method applied to the lid-driven cavity problem. Part I. High Reynolds number flow calculations, *Int. J. Numer. Meth. Fluids* **42** (2003) 57–77.
- [125] M. Sahin and R. G. Owens, A novel fully-implicit finite volume method applied to the lid-driven cavity problem. Part II. Linear stability analysis, *Int. J. Numer. Meth. Fluids* **42** (2003) 79–88.
- [126] M. Sahin and R. G. Owens, A numerical investigation of wall effects up to high blockage ratios on two-dimensional flow past a confined circular cylinder, *Phys. Fluids* (Accepted).

- [127] M. Sahin and R. G. Owens, On the effects of viscoelasticity on two-dimensional vortex dynamics in the cylinder wake, *J. Non-Newtonian Fluid Mech.* (Submitted).
- [128] T. Sarpkaya, P. G. Rainey and R. E. Kell, Flow of dilute polymer solutions about circular cylinders, *J. Fluid Mech.* **57** (1973) 177–208.
- [129] E. Schreck and M. Schäfer, Numerical study of bifurcation in three-dimensional sudden channel expansions, *Computers & Fluids* **29** (2000) 583–593.
- [130] A. Sedaghat, J. A. D. Ackroyd and N. J. Wood, Turbulence modelling for supercritical flows including examples with passive shock control, *Aero. J.* **103** (1999) 113–125.
- [131] P. N. Shankar and M. D. Deshpande, Fluid mechanics in the driven cavity, *Annu. Rev. Fluid Mech.* **32** (2000) 93–136.
- [132] J. Shen, Hopf bifurcation of the unsteady regularized driven cavity flow, *J. Comput. Phys.* **95** (1991) 228–245.
- [133] M. D. Smith, R. C. Armstrong, R. A. Brown and R. Sureshkumar, Finite element analysis of stability of two-dimensional viscoelastic flows to three-dimensional perturbations, *J. Non-Newtonian Fluid Mech.* **93** (2000) 203–244.
- [134] M. D. Smith, Y. L. Joo, R. C. Armstrong and R. A. Brown, Linear stability analysis of flow of an Oldroyd-B fluid through a linear array of cylinders, *J. Non-Newtonian Fluid Mech.* **109** (2002) 13–50.
- [135] R. W. Smith and J. A. Wright, An implicit edge-based ALE method for the incompressible Navier-Stokes equations, *Int. J. Numer. Meth. Fluids* **43** (2003) 253–279.
- [136] W. Y. Soh and J. W. Goodrich, Unsteady solution of incompressible Navier-Stokes equations, *J. Comput. Phys.* **79** (1988) 113–134.
- [137] P. K. Stansby and A. Slaouti, Simulation of vortex shedding including blockage by the random-vortex and other methods, *Int. J. Numer. Meth. Fluids* **17** (1993) 1003–1013.
- [138] J. L. Steger and R. L. Sorenson, Automatic mesh-point clustering near a boundary in grid generation with elliptic partial differential equations, *J. Comput. Phys.* **33** (1979) 405–410.
- [139] R. Sureshkumar, M. D. Smith, R. C. Armstrong and R. A. Brown, Linear stability and dynamics of viscoelastic flows using time-dependent numerical simulations, *J. Non-Newtonian Fluid Mech.* **82** (1999) 57–104.
- [140] S. Taneda, Experimental investigation of the wakes behind cylinders and plates at low Reynolds numbers, *J. Phys. Soc. Japan* **11** (1956) 302–307.
- [141] G. I. Taylor, On scraping viscous fluid from a plane surface, *Miszellaneen der Angewandten Mechanik (Festschrift Walter Tollmein)*, M. Schäfer (ed), Akademie-Verlag, Berlin, (1962) 313–315.

- [142] M. Thompson, K. Hourigan and J. Sheridan, Three-dimensional instabilities in the wake of a circular cylinder, *Experimental Thermal and Fluid Science* **12** (1996) 190–196.
- [143] D. J. Tritton, Experiments on the flow past a circular cylinder at low Reynolds numbers, *J. Fluid Mech.* **6** (1959) 547–567.
- [144] J. S. Ultman and M. M. Denn, Slow viscoelastic flow past submerged objects, *Chem. Eng. J.* **2** (1971) 81–89.
- [145] H. Usui, T. Shibata and Y. Sano, Kármán vortex behind a circular cylinder in dilute polymer solutions, *J. Chem. Engrg. Japan* **13** (1980) 77–79.
- [146] H. A. Van der Vorst, BI-CGSTAB: a fast and smoothly converging variant of BI-CG for the solution of nonsymmetric linear systems, *SIAM J. Sci. Statist. Comput.* **10** (1992) 631–644.
- [147] T. von Kármán and H. Rubach, Über die Mechanismen des Flüssigkeits und Luftwiderstandes, *Phys. Z.* **42** (1912) 173.
- [148] P. Wesseling, *An Introduction to Multigrid Methods*, John Wiley & Sons, New York (1992).
- [149] D. A. White, Drag coefficients for spheres in high Reynolds number flow of dilute solutions of high polymers, *Nature* **212** (1966) 277–278.
- [150] C. H. K. Williamson, The existence of two stages in the transition to three-dimensionality of a cylinder wake, *Phys. Fluids* **31** (1988) 3165–3168.
- [151] C. H. K. Williamson, Oblique and parallel modes of vortex shedding in the wake of a circular cylinder at low Reynolds numbers, *J. Fluid Mech.* **206** (1989) 579–627.
- [152] C. H. K. Williamson, "Mode A" secondary instability in wake transition, *Phys. Fluids* **8** (1996) 1680–1682.
- [153] C. H. K. Williamson, Vortex dynamics in the cylinder wake, *Annu. Rev. Fluid Mech.* **28** (1996) 477–539.
- [154] J. A. Wright and R. W. Smith, An edge-based method for the incompressible Navier-Stokes equations on polygonal meshes, *J. Comput. Phys.* **169** (2001) 24–43.
- [155] N. G. Wright and P. H. Gaskell, An efficient multigrid approach to solving highly recirculating flows, *Computers & Fluids* **24** (1995) 63–79.
- [156] S. C. Xue, N. Phan-Thien and R. I. Tanner, Fully three-dimensional, time-dependent numerical simulations of Newtonian and viscoelastic flows in a confined cylinder - Part I. Method and steady flows, *J. Non-Newtonian Fluid Mech.* **87** (1999) 337–367.
- [157] S. C. Xue, R. I. Tanner and N. Phan-Thien, Three-dimensional numerical simulations of viscoelastic flows - predictability and accuracy, *Comp. Meth. Appl. Mech. Engrg.* **180** (1999) 305–331.

-
- [158] H.-Q. Zhang, U. Fey, B. R. Noack, M. König and H. Eckelmann, On the transition of the cylinder wake, *Phys. Fluids* **7** (1995) 779–794.
- [159] Th. Zisis and E. Mitsoulis, Viscoplastic flow around a cylinder kept between parallel plates, *J. Non-Newtonian Fluid Mech.* **105** (2002) 1–20.
- [160] L. Zovatto and G. Pedrizzetti, Flow around a circular cylinder between parallel walls, *J. Fluid Mech.* **440** (2001) 1–25.

Curriculum Vitae

Mehmet SAHIN

Born on 15 July 1973 in Kayseri, TURKEY

- April 2001-March 2004 Ph.D. Mechanical Engineering
Swiss Federal Institute of Technology, Lausanne, SWITZERLAND
Fluid Mechanics Laboratory
Advisor Prof. Robert G. OWENS
Thesis title: "A Numerical Investigation using a Novel
Finite Volume Method of some Flow Instabilities".
- Jan 1999-July 2000 M.Sc. School of Aerospace Engineering
Georgia Institute of Technology, Atlanta, USA
Computational Aerodynamics Laboratory
Advisor Prof. Lakshimi N. SANKAR
Thesis title: "Dynamic Stall Alleviation using a Deformable
Leading Edge Concept - A Numerical Study".
- April 1996-March 1998 M.Sc. Mechanical Engineering
Yokohama National University, Yokohama, JAPAN
Advisor Prof. Kyoji KAMEMOTO
Thesis title: "A Fast Higher-Order Integral Equation Method
for Solution of the Full Potential Equation around Airfoils".
- Sept 1991-July 1995 B.Sc. Aeronautical Engineering
Istanbul Technical University, Istanbul, TURKEY
- Sept 1993-July 1995 B.Sc. Physics Engineering
Istanbul Technical University, Istanbul, TURKEY
(Double Majored)